Efficient Motion Planning and Control for Underwater Gliders

Nina Mahmoudian

Dissertation submitted to the Faculty of the
Virginia Polytechnic Institute and State University
in partial fulfillment of the requirements for the degree of

Doctor of Philosophy
in
Aerospace Engineering

Craig A. Woolsey, Chair
Christopher D. Hall
Wayne Neu
Daniel J. Stilwell

September 8, 2009
Blacksburg, Virginia

Keywords: Motion Control, Path Planning, Underwater Gliders
Copyright 2009, Nina Mahmoudian

Efficient Motion Planning and Control for Underwater Gliders

Nina Mahmoudian

(ABSTRACT)

Underwater gliders are highly efficient, winged autonomous underwater vehicles that propel themselves by modifying their buoyancy and their center of mass. The center of mass is controlled by a set of servo-actuators which move one or more internal masses relative to the vehicle's frame. Underwater gliders are so efficient because they spend most of their time in stable, steady motion, expending control energy only when changing their equilibrium state. Motion control thus reduces to varying the parameters (buoyancy and center of mass) that affect the state of steady motion. These parameters are conventionally controlled through feedback, in response to measured errors in the state of motion, but one may also incorporate a feedforward component to speed convergence and improve performance.

In this dissertation, first an approximate analytical expression for steady turning motion is derived by applying regular perturbation theory to a realistic vehicle model to develop a better understanding of underwater glider maneuverability, particularly with regard to turning motions. The analytical result, though approximate, is quite valuable because it gives better insight into the effect of parameters on vehicle motion and stability.

Using these steady turn solutions, including the special case of wings level glides, one may construct feasible paths for the gliders to follow. Because the turning motion results are only approximate, however, and to compensate for model and environmental uncertainty, one must incorporate feedback to ensure convergent path following. This dissertation describes the development and numerical implementation of a feedforward/feedback motion control system intended to enhance locomotive efficiency by reducing the energy expended for guidance and control. It also presents analysis of the designed control system using slowly varying systems theory. The results provide (conservative) bounds on the rate at which the reference command (the desired state of motion) may be varied while still guaranteeing stability of the closed-loop system. Since the motion control system more effectively achieves and maintains steady motions, it is intrinsically efficient.

The proposed control system enables speed, flight path angle, and turn rate, providing a mechanism for path following. The next step is to implement a guidance strategy, together with a path planning strategy, and one which continues to exploit the natural efficiency of this class of vehicle. The structure of the approximate solution for steady turning motion is such that, to first order in the turn rate, the glider's horizontal component of motion matches that of "Dubins' car," a kinematic car with bounded turn rates. Dubins' car is a classic example in the study of time-optimal control for mobile robots. For an underwater glider, one can relate time optimality to energy optimality. Specifically, for an underwater glider travelling at a constant speed and maximum flight efficiency (i.e., maximum lift-to-drag ratio), minimum time paths are minimum energy paths. Hence, energy-efficient paths can be obtained by generating sequences of steady wings-level and turning motions. These efficient paths can, in turn, be followed using the motion control system developed in this work.

That this work received support from the Office of Naval Research under grant number N00014-08-1-0012.

Acknowledgments

I am deeply indebted to my advisor, Craig Woolsey, for the incomparable opportunity that he provided me. I am grateful for his encouraging guidance, his close attention to my research, his mentorship, and his extraordinary kindness. I aspire to achieve his level of academic scholarship and leadership.

I sincerely thank Dr. Mehdi Ahmadian for his enlightening comments and vision. Because of his encouragement and advice, I applied to Virginia Tech and started working with Dr. Craig Woolsey at the Department of Aerospace and Ocean Engineering, which had always been my prime interest. I deeply appreciate his influence on the change of direction in the path of my life.

I would like to thank the members of my committee, Christopher Hall, Daniel Stilwell, and Wayne Neu, for reviewing my dissertation and providing me with their comments, which greatly helped me to improve the quality of this dissertation.

My department is a happy home that I will truly miss. For their contributions to my professional preparation, I thank faculty members Dr. Leigh McCue and Dr. Christopher Hall. I also thank the administrative staff, Wanda Foushee, Janet Murphy, and Rachel Hall Smith, for their organizational prowess and friendship. A special thanks goes to Steve Edwards for all his help and support whenever I needed it.

Membership in the Nonlinear Systems Lab provided me with collaborators, colleagues, and friends for life. I thank Laszlo Techy, Bob Kraus, and Chris Cotting. I also thank past lab members for their contributions and camaraderie, including Konda Reddy, Amanda Young, and Enric Xagary.

Studying with my wonderful husband Mohammad made my journey at Virginia Tech an exceptionally unique experience. Taking classes together, discussing our research, preparing for presentations, and planning for the future have never been more pleasant. His devotion and dedication will continue to take us to the higher heights.

I want to thank my family for their continuous support and encouragement. My brothers Mani and Rasa's affection have always been a great comfort. I also thank my parents, Nazi and Taher; their love and caring go beyond what I have ever seen. I now fully appreciate the emphasis my father has always put on ethics and values and feel overwhelmed when I remember how my mother taught me to live, learn, and love. Who I have become, what I believe in, and my ability to look towards a wonderful future are all because of her, and I wish to dedicate this dissertation to her.

Contents

List of Figures

List of Tables

Chapter 1

Introduction

The ocean covers approximately 71 percent of the surface of Earth. Ocean water has a great impact on the climate of Earth; however, many global oceanographic phenomena are not yet well understood [5]. Research efforts are focused on developing models and tools to better understand the coupled physical and biological dynamics of the oceans and their impact on the environment, from marine ecosystems to the global climate [6].

The main challenge is collecting data "in a vast, inhospitable, and unforgiving" ocean environment [7]. Different sensing methods are being used to measure pressure, temperature, salinity, sound speed, density, and velocity in the ocean [7]. Surface drifters and deep ocean floats are examples of traditional measurement systems [7]. The use of remote sensing techniques (acoustic and electromagnetic) from satellites in recent years helped a lot of the ocean surface studies [7], but limited measurements under ocean surface can be made with traditional methods. In recent years, marine scientists have used autonomous underwater vehicles (AUVs) as an important tool in gathering oceanographic data, replacing the traditional process of using expendable sensors, moored profilers, and floats in deep ocean. AUVs are able to operate at a fraction of overall costs and to gather orders of magnitude more data than traditional approaches [5]. However, the propulsion systems and power storage limitations of conventional AUVs do not allow for long-term deployments, at least not with-

out a significant investment in undersea infrastructure to enable recharging. Conventional, battery-powered, propeller-driven AUVs can only operate on the order of a few hours before their power is depleted. Buoyancy-driven underwater gliders, on the other hand, have proven to be quite effective for long-range, long-term oceanographic sampling. Gliders are winged autonomous mobile platforms that use changes in buoyancy as their source of propulsion.

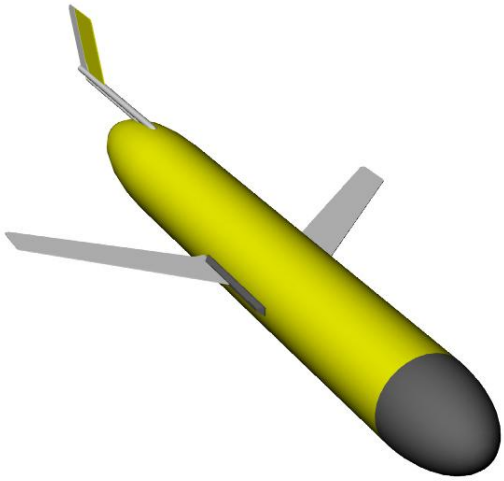

Figure 1.1 The underwater glider *Slocum* solid model [1].

The idea of underwater gliders, formally proposed in [8], was developed by oceanographer Henry Stommel and his colleague and protégé Doug Webb, an innovative developer of oceanographic instrumentation [9]. The original prototype was named *Slocum* in keeping with the vision of an autonomous vehicle that might someday circumnavigate the globe [10]. (Joshua Slocum was the first human sailor to circumnavigate the globe solo in his small boat, *Spray* [9].) The concept of gliding to conserve energy while diving in the ocean is also used by marine mammals such as seals, dolphins, and whales. The bodies and lungs of these animals compress enough to make them heavy at depth, enabling them to glide for longer and deeper dives [9].

Underwater gliders modulate their buoyancy to rise or sink. The typical configurations use an electric or hydraulic pump to force oil from an internal bladder to an external one, causing the vehicle to gain bouyancy and rise to the surface. To sink, water pressure forces

the oil to return to the internal bladder when a valve is open and the bladders are separated. Gliders locomote by repeatedly descending and ascending in a sawtooth pattern, communicating with a mission-control center via satellite at surface points. To steer, they use servo-actuators, protected within the hull of the vehicle, to shift the center of mass relative to the center of buoyancy and to control pitch and roll attitude. By appropriately cycling these actuators, underwater gliders can control their directional motion and propel themselves with great efficiency. These gliders can reach up to 1500 meters' depth. They carry sensors such as conductivity-temperature-depth (CTD) sensors, fluorometers, dissolved oxygen sensors, photosynthetically active radiation (PAR) sensors, and biological and other sensors [5]. The collected sensor data is stored on board, and a subset of the data can be communicated back to a mission center when the vehicle surfaces, allowing scientists to monitor the progress of the glider mission and change mission parameters, if necessary. At the end of the mission, possibly after months of deployment and thousands of kilometers' travel, the gliders are retrieved.

The first generation of underwater gliders includes *Slocum* [10], manufactured by the Webb Research Corporation (recently acquired by Teledyne) (Figure 1.1); *Seaglider* [11], manufactured originally by the University of Washington Applied Physics Laboratory; and *Spray* [12], manufactured by the Scripps Institution of Oceanography. These "legacy gliders" were designed with similar functional objectives [13, 14] so they are similar in weight, size, and configuration (see Table 1.1 for detailed information).

The *Slocum* electric glider is manufactured in "coastal configuration" for shallow water operation (30 m, 100 m, and 200 m) and "1 km configuration" for deep water. Both configurations use battery power to alter buoyancy, hence their length of time of operation is limited by battery life. To date, over 165 systems are operating worldwide in 14 countries and being used by 45 different groups for observing the oceans [15]. For example, Rutgers University Coastal Ocean Observation Lab (RU-COOL) have flown battery-powered *Slocum* gliders over 62000 km in partnership with Teledyne Webb Research in different endurance

flights, including a New Jersey to Halifax, Novia Scotia, run and a New Jersey to the Azores mission [15]. Presently, RU27, the "Scarlet Knight", is over halfway across the Atlantic [15] to finish the unfinished voyage of RU17, which set a record-breaking distance of 5700 km during a five-month flight [16].

A University of Washington *Seaglider* holds the world record for the longest-duration mission of six months; it has made round-trips hundreds of miles in length under the Arctic ice [17]. The iRobot corporation has manufactured and delivered more than 80 *Seaglider* systems worldwide [18].

Table 1.1 Specifications of "Legacy gliders" [4].

Platform	***Slocum* Electric** Coastal & 1 km	***Seaglider*** Original & iRobot	***Spray***
Body Type	cylindrical + wings	Teardrop	cylindrical + wings
Overall Size (m) $(L \times W \times H)$	$1.79 \times 1.01 \times 0.49$	$2.8 \times 1 \times 0.4$	$1.8 \times 1.01 \times 0.3$
Fuselage Size (m) $(L \times D)$	1.5×0.21	1.8×0.3	1.8×0.3
Hull Material	Aluminium	Fiberglass	Aluminium
Weight (kg)	52	52	52
Max. Depth (m)	1000	1000	1500
Endurance (hours)	3800	5333.3	6666.7
Nominal Speed (m/s)	0.4	0.25	0.25

These legacy gliders have proven their worth as quiet, reliable, effective, and low-cost ocean-sampling platforms. They are suitable for long-range travel and endurance, if low to moderate speed is acceptable. Their sawtooth profile is well-suited for both vertical and horizontal observations in the water column. They are unobtrusive, with low noise radiation and small surface expression. They can be deployed by one to two people. And they

are comparatively low cost: each glider costs between $150-200K, depending on the sensor configuration [5].

The ALBAC glider, available since 1992, is a shuttle-type glider developed at the University of Tokyo, Institute of Industrial Science. The ALBAC design uses a drop weight to drive the glider in a single dive cycle between deployment and recovery from ship [19]. It has a cylindrical body (1.4 m $\times$ 0.24 m) with wings (1.2 m wing span) and can reach to maximum depth of 300 m. The development of mini underwater glider (MUG) for educational purposes is another example of University of Tokyo activities in this area [20]. MUG is a light-weight (1.92 kg), low-cost ($35 dollars) small-winged underwater glider (0.1 m wing span) with a cylindrical body (0.36 m $\times$ 0.1 m) [20].

Princeton University's ROGUE vehicle is another example of a laboratory-scale underwater glider. ROGUE has an elliptical body ($0.45 \times 0.3 \times 0.15$ m) with a wingspan of 0.7 m and weighs around 11 kg [9, 21]. It is designed for experiments in glider dynamics and control [9].

The STERNE glider is a hybrid design with both ballast control and a thruster by ENSIETA, which is administered under the French Ministry for Defense [9]. A shape-optimized underwater glider has been developed by Shenyang Institute of Automation, Chinese Academy of Sciences [20].

The application of underwater gliders is going beyond long-term, basin-scale oceanographic sampling for environmental monitoring to littoral surveillance and military applications. Unmanned underwater surveillance vehicles have been proposed to detect, classify, and locate hostile submarines to protect U.S. Navy personnel and vessels [22]. The Navy plans to buy many underwater gliders (up to 150 gliders by 2014 [23]), in addition to powered unmanned underwater vehicles, to boost its oceanographic research efforts and to help improve the positioning of fleets during naval maneuvers [16, 23]. The Navy's Space and Naval Warfare Systems Command has awarded a contract to design a "littoral battle space sensing-glider" (LBS-G) by July 2010 [23].

Table 1.2 Specifications of other underwater gliders [4].

Platform	***Slocum* Thermal**	***Liberdade*/XRay**	**Bionik Manta**
Body Type	cylindrical + wings	Blended Wing Body	Biomimetic
Overall Size (m) $(L \times W \times H)$	$1.79 \times 1.01 \times 0.49$	$1.68 \times 6.1 \times 0.69$	$1.5 \times 3.5 \times 0.5$
Fuselage Size (m) $(L \times W \times H)$	1.5×0.21	-	-
Weight (kg)	56	850	10
Max. Depth (m)	1200	365	100
Endurance (hours)	43800	(nominal load) 200 (hotel load) 4382	24
Nominal Speed (m/s)	0.4	1.8	1.39

The developers make continual improvements and demonstrate new capabilities that increase value of underwater gliders for military and research communities [16]. Bionik Manta, a product of EvoLogics, a Germany-based high-tech enterprise, is the result of efforts to develop smaller and smarter platforms. Bionik Manta propels itself with a natural movement of "fins" and uses active life-like wing propulsion and level gliding, semi-passive buoyancy-driven gliding, and hydro-jet propulsion as three propulsion modes [24]; see Table 1.2 for more information. Studies of the form and structure of fins of fishes show the biomechanical effect of the spine or ray of the fish fin patented as the "fin ray effect" [24]. The implementations of these constructions led to shape-adaptive wing profiles and flow control devices [24].

Very recent efforts have focused on improving the propulsive efficiency of the legacy gliders even further. One way to increase propulsive efficiency is to harvest the energy needed for buoyancy change from the thermocline of the ocean. The *Slocum* thermal glider is developed based on this idea [15]. The substantial energy savings can result in greater endurance, up to 5 years. (See Table 1.2 for detailed information.) Currently the recent version of this

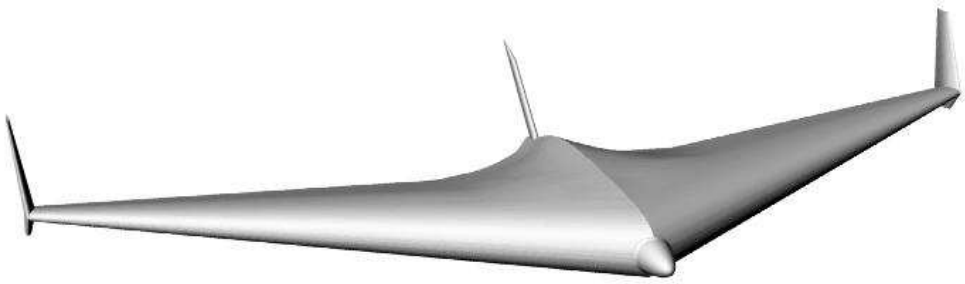

Figure 1.2 The blended wing-body underwater glider *Liberdade/XRay* solid model [1].

glider called Drake is traveling from St. Thomas to Cape Verde [15].

Another way of improving the propulsive efficiency of the legacy gliders is through design optimization, resulting in a newer type of "blended wing-body" glider shown in Figure 1.2 and described in [14]. A prototype of the blended wing-body glider proposed in [14] has been developed jointly by the Scripps Institute of Oceanography's Marine Physical Laboratory and the University of Washington's Applied Physics Laboratory. This vehicle is being developed as a part of the Navy's Persistent Littoral Undersea Surveillance Network (PLUSNet) system of semi-autonomous controlled mobile assets. PLUSNet envisions a network of autonomous underwater vehicles (AUVs) to monitor shallow-water environments from fixed positions on the ocean floor, or by moving through the water to scan large areas for extended periods of time. The first major PLUSNet field experiment for the *Liberdade/XRay* was on August 2006 in Monterey Bay, California [25]. Researchers use the collected data to understand how ocean layers and currents affect the transmission of sounds and electrical and magnetic signals generated by ships (as well as by marine mammals and submarines).

The most recent *Liberdade/XRay* configuration is the world's largest underwater glider. (See Table 1.2 for detail information.) Size is an advantage in terms of hydrodynamic efficiency and space for energy storage and payload. The glider is designed to track quiet diesel-electric submarines operating in shallow-water environments. Like other gliders, it can be deployed quickly and covertly, then stay in operation for a matter of months. It can be programmed to monitor large areas of the ocean (maximum ranges exceeding 1000 km with

on-board energy supplies). The glider is very quiet, making it hard to detect using passive acoustic sensing. The *Liberdade/XRay* is equipped for autonomous operation. Its payload includes acoustics and electric field sensors, along with acoustic and satellite communications capabilities. It was designed for low-cost acquisition, deployment, and retrieval, as well as greater payload carrying capability, cross-country speed, and horizontal point-to-point transport efficiency than existing gliders.

Underwater gliders have proved their efficiency in long-term, basin-scale oceanographic sampling, as well as surveillance and tactical oceanography in shallow water. The interest in using a fleet of these vehicles as a "cost-effective and efficient means" for collecting data is increasing [16].

The objective of this study is to develop implementable, energy-efficient motion control strategies that further improve the inherent efficiency of underwater gliders. Outcomes will include more intelligent behaviors for existing vehicles and improved design guidelines for future underwater gliders.

This work builds on the preliminary work in [9] and [26] to provide a better understanding of glider maneuverability, particularly with regard to turning motions. Nonlinear dynamic models presented in [9, 26, 27] provided the basis for investigations of longitudinal gliding flight. Although the emphasis was on wings level flight, turning motions were also discussed in [9] and [26] and examples were shown for the given vehicle models with chosen parameter values. Bhatta [26] also presented the results of a numerical parametric analysis. No analytical expressions were provided, however, so it is difficult to make general conclusions about the relationship between parameter values and turning motion characteristics. To address this problem, we present a method to find an analytical solution for steady turning flight in Chapter 3.

Early efforts in control of buoyancy-driven vehicles focused on designing efficient, stable, steady motions and controlling the vehicles near these nominal motions [28]. More recent efforts have focused on improving hydrodynamic design [14]. Classical proportional-integral-

derivative (PID) controllers are commonly used for attitude control. These controllers are tuned based on experience and field-tests by glider designers and operators. (See [29], [26], and [14], for example.) A systematic approach to design an underwater glider control system using standard linear optimal control methods was presented in [9] and [27]. Leonard and Graver [9, 27] mentioned the potential value of "complementing the feedback law with a feedforward term which drives the movable mass and the variable mass in a predetermined way from initial to final condition" in control of underwater gliders. Based on this idea, Chapter 4 presents an efficient motion control system, which exploits the properties of the steady wings-level and turning motions.

Dissertation Overview

In Chapter 2, the complete multi-body dynamic model that incorporates buoyancy and moving mass actuator dynamics is developed. The vehicle dynamic model is presented for two cases of actuator dynamics: First, a vehicle, such as *Slocum*, with rectilinear moving mass actuation is considered in Section 2.1. Second, a vehicle with cylindrical moving actuator motion, such as *Seaglider*, is considered in Section 2.2.

Chapter 3 presents an analytical approach to find (approximate) solutions for steady-state flight in terms of the model parameters. The analytical result for wings level gliding flight presented in [21] is reviewed in Section 3.1 and existence and stability of steady turning motions for general parameter values is studied in Section 3.2.2. In Section 3.3, a numerical case study is presented.

In Chapter 4, a feedforward/feedback structure for a glider motion control system is described. Given some desired steady flight condition, the feedforward term drives the moving mass and buoyancy bladder servo-actuators to predetermined equilibrium positions obtained from an (approximate) analytical solution for steady straight and turning motions presented in Chapter 3. The feedback term compensates for the errors due to the approximation, environmental uncertainty, etc. Using this control system, steady motions may be concatenated

to achieve compatible guidance objectives, such as waypoint following. In Section 4.4, the stability of the closed-loop system is analyzed using slowly varying systems theory. Simulation results for the *Slocum* model given in [26] are presented in Section 4.5.

Chapter 5 shows the process of developing and analyzing stability of a feedforward/feedback controller for a simple dynamical system that exhibits a saddle-node bifurcation. In analogy with the underwater glider problem, the stable manifold of the dynamical system is approximated in the neighborhood of a particular equilibrium using regular perturbation theory, a feedforward/feedback controller is designed, and stability of the closed-loop system is examined.

Chapter 6 introduces the problem of optimal motion planning for underwater gliders. In Section 6.1, it is recognized that, by exploiting the special structure of the approximate solution given in Section 3.2.2, one may apply existing optimal path planning results obtained for planar mobile robots. Section 6.2 presents examples of guidance strategies which use the previously developed motion control system to make underwater gliders fly in a desired pattern.

Conclusions and a description of ongoing research are provided in Chapter 7.

Contributions:

- An approximate analytical expression for steady turning motion is derived by applying regular perturbation theory to a realistic underwater glider model.
- A feedforward/feedback motion control system structure is developed to enhance locomotive efficiency by reducing the energy expended by underwater glider guidance and control.
- It is recognized that for underwater gliders energy-efficient paths can be obtained by generating sequences of steady wings-level and turning motions.

Chapter 2

Modeling

The complete multi-body dynamic model that incorporates buoyancy and moving mass actuator dynamics is developed in this chapter. Nonlinear dynamic models presented in [9, 26, 27] and the process presented in [30] provided the basis for the model developed here and presented in [31–33].

2.1 Vehicle Dynamic Model with Rectilinear Actuator Dynamics

The glider is modeled as a rigid body (mass m_{rb}) with two moving mass actuators ($m_{\mathrm{p_x}}$ and $m_{\mathrm{p_y}}$) and a variable ballast actuator (m_{b}). The total vehicle mass is

$$m_{\mathrm{v}} = m_{\mathrm{rb}} + m_{\mathrm{p_x}} + m_{\mathrm{p_y}} + m_{\mathrm{b}},$$

where m_{b} can be modulated by control.

The vehicle displaces a volume of fluid of mass m. If $\tilde{m} = m_{\mathrm{v}} - m$ is greater than zero, the vehicle is heavy in water and tends to sink, while if $\tilde{m}$ is negative, the vehicle is buoyant in water and tends to rise. Figure 2.1 shows the simplified model for the underwater glider actuation system. The variable mass is represented by a mass particle m_{b} located at the origin of a body-fixed reference frame.

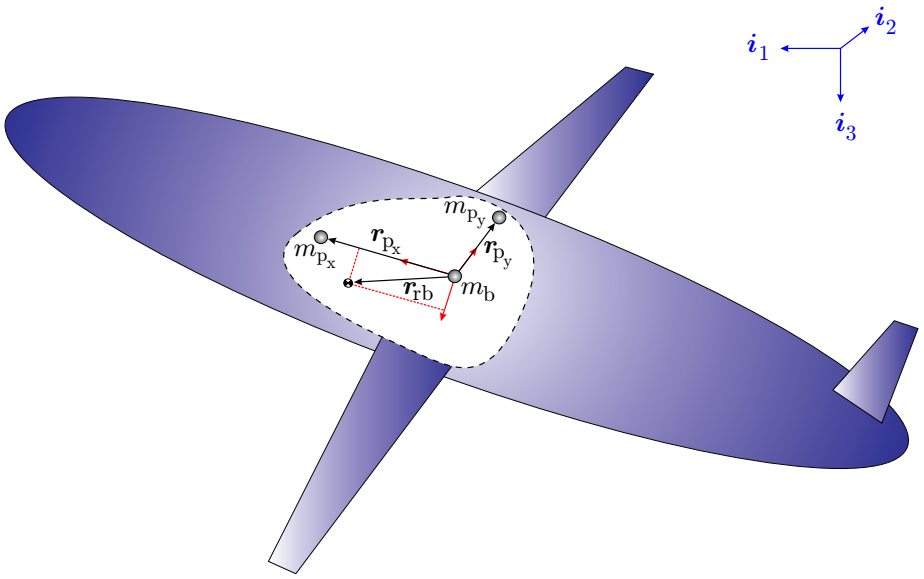

Figure 2.1 Illustration of point mass actuators.

The vehicle's attitude is given by a proper rotation matrix $\boldsymbol{\mathcal{R}}_{\mathrm{IB}}$ which maps free vectors from the body-fixed reference frame to a reference frame fixed in inertial space. The body frame is defined by an orthonormal triad $\{\boldsymbol{b}_1, \boldsymbol{b}_2, \boldsymbol{b}_3\}$, where $\boldsymbol{b}_1$ is aligned with the body's longitudinal axis. The inertial frame is represented by an orthonormal triad $\{\boldsymbol{i}_1, \boldsymbol{i}_2, \boldsymbol{i}_3\}$, where $\boldsymbol{i}_3$ is aligned with the local direction of gravity. To define the rotation matrix explicitly, let

$$\boldsymbol{e}_1 = \begin{pmatrix} 1 \\ 0 \\ 0 \end{pmatrix}, \quad \boldsymbol{e}_2 = \begin{pmatrix} 0 \\ 1 \\ 0 \end{pmatrix}, \quad \text{and} \quad \boldsymbol{e}_3 = \begin{pmatrix} 0 \\ 0 \\ 1 \end{pmatrix}$$

represent the standard basis for $\mathbb{R}^3$. Also, let the character $\hat{\cdot}$ denote the 3×3 skew-symmetric matrix satisfying $\hat{\boldsymbol{a}}\boldsymbol{b} = \boldsymbol{a} \times \boldsymbol{b}$ for 3-vectors $\boldsymbol{a}$ and $\boldsymbol{b}$.

The rotation matrix $\boldsymbol{\mathcal{R}}_{\mathrm{IB}}$ is typically parameterized using the roll angle ϕ, pitch angle θ, and yaw angle ψ:

$$\boldsymbol{\mathcal{R}}_{\mathrm{IB}}(\phi, \theta, \psi) = e^{\widehat{\boldsymbol{e}_3}\psi} e^{\widehat{\boldsymbol{e}_2}\theta} e^{\widehat{\boldsymbol{e}_1}\phi} \qquad \text{where} \qquad e^{\boldsymbol{Q}} = \sum_{n=0}^{\infty} \frac{1}{n!} \boldsymbol{Q}^n \quad \text{for} \quad \boldsymbol{Q} \in \mathbb{R}^{n \times n}.$$

More explicitly,

$$\boldsymbol{\mathcal{R}}_{\mathrm{IB}}(\phi,\theta,\psi) = \begin{pmatrix} \cos\theta\cos\psi & \sin\phi\sin\theta\cos\psi - \cos\phi\sin\psi & \cos\phi\sin\theta\cos\psi + \sin\phi\sin\psi \\ \cos\theta\sin\psi & \cos\phi\cos\psi + \sin\phi\sin\theta\sin\psi & -\sin\phi\cos\psi + \cos\phi\sin\theta\sin\psi \\ -\sin\theta & \sin\phi\cos\theta & \cos\phi\cos\theta \end{pmatrix}.$$

Let $\boldsymbol{v} = [u,\ v,\ w]^T$ represent the translational velocity and let $\boldsymbol{\omega} = [p,\ q,\ r]^T$ represent the rotational velocity of the underwater glider with respect to inertial space, where $\boldsymbol{v}$ and $\boldsymbol{\omega}$ are both expressed in the body frame. If $\boldsymbol{y}$ represents the position of the body frame origin with respect to the inertial frame, the vehicle kinematic equations are

$$\dot{\boldsymbol{y}} = \boldsymbol{\mathcal{R}}_{\mathrm{IB}}\boldsymbol{v} \tag{2.1}$$

$$\dot{\boldsymbol{\mathcal{R}}}_{\mathrm{IB}} = \boldsymbol{\mathcal{R}}_{\mathrm{IB}}\hat{\boldsymbol{\omega}}. \tag{2.2}$$

In terms of these Euler angles, the kinematic equations (2.1) and (2.2) become, respectively,

$$\begin{pmatrix} \dot{x} \\ \dot{y} \\ \dot{z} \end{pmatrix} = \begin{pmatrix} \cos\theta\cos\psi & \sin\phi\sin\theta\cos\psi - \cos\phi\sin\psi & \cos\phi\sin\theta\cos\psi + \sin\phi\sin\psi \\ \cos\theta\sin\psi & \cos\phi\cos\psi + \sin\phi\sin\theta\sin\psi & -\sin\phi\cos\psi + \cos\phi\sin\theta\sin\psi \\ -\sin\theta & \sin\phi\cos\theta & \cos\phi\cos\theta \end{pmatrix} \begin{pmatrix} u \\ v \\ w \end{pmatrix}$$

$$\begin{pmatrix} \dot{\phi} \\ \dot{\theta} \\ \dot{\psi} \end{pmatrix} = \begin{pmatrix} 1 & \sin\phi\tan\theta & \cos\phi\tan\theta \\ 0 & \cos\phi & -\sin\phi \\ 0 & \sin\phi\sec\theta & \cos\phi\sec\theta \end{pmatrix} \begin{pmatrix} p \\ q \\ r \end{pmatrix}.$$

The dynamic equations relate external forces and moments to rates of change of velocity. Accordingly, following [30], define the mass, inertia, and inertial coupling matrices for the combined rigid body/moving mass/variable ballast system as

$$\begin{aligned} \boldsymbol{I}_{\mathrm{rb/p/b}} &= \boldsymbol{I}_{\mathrm{rb}} - m_{\mathrm{p_x}}\hat{\boldsymbol{r}}_{\mathrm{p_x}}\hat{\boldsymbol{r}}_{\mathrm{p_x}} - m_{\mathrm{p_y}}\hat{\boldsymbol{r}}_{\mathrm{p_y}}\hat{\boldsymbol{r}}_{\mathrm{p_y}} \\ \boldsymbol{M}_{\mathrm{rb/p/b}} &= m_{\mathrm{v}}\mathbb{1} \\ \boldsymbol{C}_{\mathrm{rb/p/b}} &= m_{\mathrm{rb}}\hat{\boldsymbol{r}}_{\mathrm{rb}} + m_{\mathrm{p_x}}\hat{\boldsymbol{r}}_{\mathrm{p_x}} + m_{\mathrm{p_y}}\hat{\boldsymbol{r}}_{\mathrm{p_y}} \end{aligned}$$

where $\mathbb{1}$ represents the 3×3 identity matrix. As indicated in Figure 2.1, the mass particle $m_{\mathrm{p_x}}$ is constrained to move along the longitudinal axis while the mass particle $m_{\mathrm{p_y}}$ is constrained to move along the lateral axis:

$$\boldsymbol{r}_{\mathrm{p_x}} = r_{\mathrm{p_x}}\boldsymbol{e}_1 \quad \text{and} \quad \boldsymbol{r}_{\mathrm{p_y}} = r_{\mathrm{p_y}}\boldsymbol{e}_2.$$

The rigid body inertia matrix $\boldsymbol{I}_{\mathrm{rb}}$ represents the distribution of mass m_{rb} and is assumed to take the form

$$\boldsymbol{I}_{\mathrm{rb}} = \begin{pmatrix} I_{xx} & 0 & -I_{xz} \\ 0 & I_{yy} & 0 \\ -I_{xz} & 0 & I_{zz} \end{pmatrix}$$

where the off-diagonal terms in $\boldsymbol{I}_{\mathrm{rb}}$ arise, for example, from an offset center of mass $\boldsymbol{r}_{\mathrm{rb}}$.

Generalized Vehicle Inertia $\mathbb{M}_{\mathrm{rb/p/b}}$

$$\begin{pmatrix} \boldsymbol{I}_{\mathrm{rb/p/b}} & \boldsymbol{C}_{\mathrm{rb/p/b}} & m_{\mathrm{p_x}}\hat{\boldsymbol{r}}_{\mathrm{p_x}}\boldsymbol{e}_1 & m_{\mathrm{p_y}}\hat{\boldsymbol{r}}_{\mathrm{p_y}}\boldsymbol{e}_2 \\ \boldsymbol{C}^T_{\mathrm{rb/p/b}} & \boldsymbol{M}_{\mathrm{rb/p/b}} & m_{\mathrm{p_x}}\boldsymbol{e}_1 & m_{\mathrm{p_y}}\boldsymbol{e}_2 \\ -m_{\mathrm{p_x}}\boldsymbol{e}_1^T\hat{\boldsymbol{r}}_{\mathrm{p_x}} & m_{\mathrm{p_x}}\boldsymbol{e}_1^T & m_{\mathrm{p_x}} & 0 \\ -m_{\mathrm{p_y}}\boldsymbol{e}_2^T\hat{\boldsymbol{r}}_{\mathrm{p_y}} & m_{\mathrm{p_y}}\boldsymbol{e}_2^T & 0 & m_{\mathrm{p_y}} \end{pmatrix}$$

Table 2.1 Generalized inertia matrix.

It is notationally convenient to compile the various inertia matrices into the *generalized* inertia matrix shown in Table 2.1. The generalized *added* inertia matrix is composed of the added mass matrix $\boldsymbol{M}_{\mathrm{f}}$, the added inertia matrix $\boldsymbol{I}_{\mathrm{f}}$, and the added inertial coupling matrix $\boldsymbol{C}_{\mathrm{f}}$:

$$\mathbb{M}_{\mathrm{f}} = \begin{pmatrix} \boldsymbol{I}_{\mathrm{f}} & \boldsymbol{C}_{\mathrm{f}} & \mathbb{O}_{3\times2} \\ \boldsymbol{C}^T_{\mathrm{f}} & \boldsymbol{M}_{\mathrm{f}} & \mathbb{O}_{3\times2} \\ \mathbb{O}_{2\times3} & \mathbb{O}_{2\times3} & \mathbb{O}_{2\times2} \end{pmatrix}.$$

The generalized added inertia matrix accounts for the energy necessary to accelerate the fluid around the vehicle as it rotates and translates. The inviscid (potential flow) hydrodynamic parameters are the components of the generalized added inertia matrix and, in notation similar to that defined by SNAME [34][1], are presented as:

$$\left(\begin{array}{c|c} \boldsymbol{I}_{\mathrm{f}} & \boldsymbol{C}_{\mathrm{f}} \\ \hline \boldsymbol{C}_{\mathrm{f}}^{T} & \boldsymbol{M}_{\mathrm{f}} \end{array}\right) = -\left(\begin{array}{ccc|ccc} L_{\dot{p}} & L_{\dot{q}} & L_{\dot{r}} & L_{\dot{u}} & L_{\dot{v}} & L_{\dot{w}} \\ M_{\dot{p}} & M_{\dot{q}} & M_{\dot{r}} & M_{\dot{u}} & M_{\dot{v}} & M_{\dot{w}} \\ N_{\dot{p}} & N_{\dot{q}} & N_{\dot{r}} & N_{\dot{u}} & N_{\dot{v}} & N_{\dot{w}} \\ \hline X_{\dot{p}} & X_{\dot{q}} & X_{\dot{r}} & X_{\dot{u}} & X_{\dot{v}} & X_{\dot{w}} \\ Y_{\dot{p}} & Y_{\dot{q}} & Y_{\dot{r}} & Y_{\dot{u}} & Y_{\dot{v}} & Y_{\dot{w}} \\ Z_{\dot{p}} & Z_{\dot{q}} & Z_{\dot{r}} & Z_{\dot{u}} & Z_{\dot{v}} & Z_{\dot{w}} \end{array}\right).$$

The generalized inertia for the vehicle/fluid system is

$$\mathbb{M} = \mathbb{M}_{\mathrm{rb/p/b}} + \mathbb{M}_{\mathrm{f}} \tag{2.3}$$

We define the inertia $\boldsymbol{I}$, mass $\boldsymbol{M}$, and coupling $\boldsymbol{C}$ matrices in the following form:

$$\begin{aligned} \boldsymbol{I} &= \boldsymbol{I}_{\mathrm{rb/p/b}} + \boldsymbol{I}_{\mathrm{f}} \\ \boldsymbol{M} &= \boldsymbol{M}_{\mathrm{rb/p/b}} + \boldsymbol{M}_{\mathrm{f}} \\ \boldsymbol{C} &= \boldsymbol{C}_{\mathrm{rb/p/b}} + \boldsymbol{C}_{\mathrm{f}}. \end{aligned}$$

Generalized Velocity ($\boldsymbol{\eta}$)	Generalized Momentum ($\boldsymbol{\nu}$)
$\begin{pmatrix} \boldsymbol{\omega} \\ \boldsymbol{v} \\ \dot{r}_{\mathrm{p_x}} \\ \dot{r}_{\mathrm{p_y}} \end{pmatrix}$	$\begin{pmatrix} \boldsymbol{h}_{\mathrm{sys}} \\ \boldsymbol{p}_{\mathrm{sys}} \\ p_{\mathrm{p_x}} \\ p_{\mathrm{p_y}} \end{pmatrix}$

Table 2.2 Generalized velocity and momentum.

Let $\boldsymbol{p}_{\mathrm{sys}}$ represent the total linear momentum of the vehicle/fluid system and $\boldsymbol{h}_{\mathrm{sys}}$ represent the total angular momentum. Let $\boldsymbol{p}_{\mathrm{p_x}}$ and $\boldsymbol{p}_{\mathrm{p_y}}$ represent the total translational momen-

[1] In SNAME notation, roll moment is denoted by K rather than L.

tum of the moving mass particles. Defining the generalized velocity $\boldsymbol{\eta}$ and the generalized momentum $\boldsymbol{\nu}$ as in Table 2.2, we have

$$\boldsymbol{\nu} = \mathbb{M}\boldsymbol{\eta}. \tag{2.4}$$

The dynamic equations relate external forces and moments to rates of change of momentum:

$$\begin{aligned}
\dot{\boldsymbol{h}}_{\text{sys}} &= \boldsymbol{h}_{\text{sys}} \times \boldsymbol{\omega} + \boldsymbol{p}_{\text{sys}} \times \boldsymbol{v} + (m_{\text{rb}} g \boldsymbol{r}_{\text{rb}} + m_{\text{p}_\text{x}} g \boldsymbol{r}_{\text{p}_\text{x}} + m_{\text{p}_\text{y}} g \boldsymbol{r}_{\text{p}_\text{y}}) \times \boldsymbol{\zeta} + \boldsymbol{T}_{\text{visc}} \\
\dot{\boldsymbol{p}}_{\text{sys}} &= \boldsymbol{p}_{\text{sys}} \times \boldsymbol{\omega} + \tilde{m} g \boldsymbol{\zeta} + \boldsymbol{F}_{\text{visc}} \\
\dot{p}_{\text{p}_\text{x}} &= \boldsymbol{e}_1 \cdot (\boldsymbol{p}_{\text{p}_\text{x}} \times \boldsymbol{\omega} + m_{\text{p}_\text{x}} g \boldsymbol{\zeta}) + \tilde{u}_{\text{p}_\text{x}} \\
\dot{p}_{\text{p}_\text{y}} &= \boldsymbol{e}_2 \cdot \left(\boldsymbol{p}_{\text{p}_\text{y}} \times \boldsymbol{\omega} + m_{\text{p}_\text{y}} g \boldsymbol{\zeta}\right) + \tilde{u}_{\text{p}_\text{y}} \\
\dot{m}_{\text{b}} &= u_{\text{b}}.
\end{aligned} \tag{2.5}$$

The forces $\tilde{u}_{\text{p}_\text{x}}$ and $\tilde{u}_{\text{p}_\text{y}}$ can be chosen to cancel to remaining terms in the equations for $\dot{p}_{\text{p}_\text{x}}$ and $\dot{p}_{\text{p}_\text{y}}$, so that

$$\begin{aligned}
\dot{p}_{\text{p}_\text{x}} &= u_{\text{p}_\text{x}} \\
\dot{p}_{\text{p}_\text{y}} &= u_{\text{p}_\text{y}}.
\end{aligned}$$

These inputs may then be chosen to servo-actuate the point mass positions for attitude control, although with inherent limits on point mass position and velocity. (Physically, these actuators might each consist of a large weight mounted on a lead screw that is driven by a servomotor.) The mass flow rate u_{b} is chosen to servo-actuate the vehicle's net weight, again with inherent control magnitude and rate limits. These magnitude and rate limits are significant for underwater gliders and must be accounted for in control design and analysis.

The terms $\boldsymbol{T}_{\text{visc}}$ and $\boldsymbol{F}_{\text{visc}}$ represent external moments and forces which do not derive from scalar potential functions. These moments and forces include control moments, such as the yaw moment due to a rudder, and viscous forces, such as lift and drag.

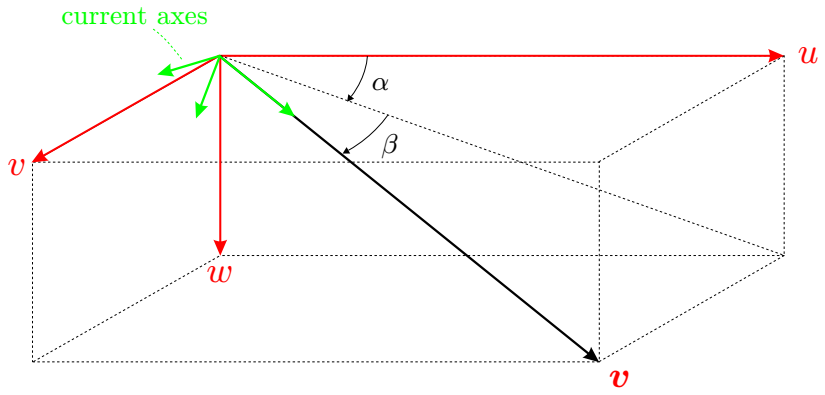

Figure 2.2 Illustration of the aerodynamic angles.

The viscous force and moment are most easily expressed in the "current" reference frame. This frame is related to the body frame through the proper rotation

$$\boldsymbol{\mathcal{R}}_{\mathrm{BC}}(\alpha,\beta) = e^{-\widehat{\boldsymbol{e}_2}\alpha} e^{\widehat{\boldsymbol{e}_3}\beta} = \begin{pmatrix} \cos\alpha\cos\beta & -\cos\alpha\sin\beta & -\sin\alpha \\ \sin\beta & \cos\beta & 0 \\ \sin\alpha\cos\beta & -\sin\alpha\sin\beta & \cos\alpha \end{pmatrix}.$$

For example, one may write

$$\boldsymbol{v} = \boldsymbol{\mathcal{R}}_{\mathrm{BC}}(\alpha,\beta)(V\boldsymbol{e}_1) = \begin{pmatrix} V\cos\alpha\cos\beta \\ V\sin\beta \\ V\sin\alpha\cos\beta \end{pmatrix}.$$

Transformations between various reference frames of interest in vehicle dynamics are illustrated in Figure 2.3. The most commonly used reference frames are the inertial, body, and current reference frames, as defined here. Also depicted is the velocity reference frame, which is related to the current frame through the bank angle μ and to the inertial frame through the flight path angle γ and the heading angle ζ. (See [2] for details and formal definitions of μ, γ, and ζ.)

The viscous forces and moments are expressed in terms of the hydrodynamic angles

$$\alpha = \arctan\left(\frac{w}{u}\right) \qquad \text{and} \qquad \beta = \arcsin\left(\frac{v}{V}\right),$$

where $V = \|\boldsymbol{v}\|$. Following standard modeling conventions, we write

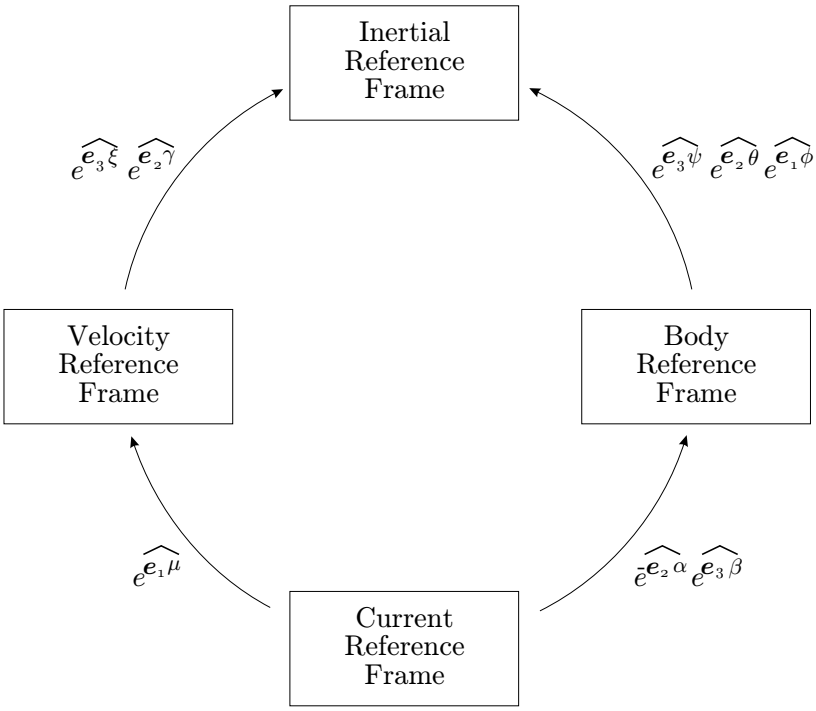

Figure 2.3 Rotational transformations between various reference frames. (Adapted from [2].)

$$\boldsymbol{F}_{\text{visc}} = -\boldsymbol{\mathcal{R}}_{\text{BC}}(\alpha,\beta)\begin{pmatrix} \mathcal{D}(\alpha) \\ \mathcal{S}_\beta\beta + S_{\delta r}\delta r \\ \mathcal{L}_\alpha\alpha \end{pmatrix} \quad \text{and} \quad \boldsymbol{T}_{\text{visc}} = \boldsymbol{D}_\omega\boldsymbol{\omega} + \begin{pmatrix} L_\beta\beta \\ M_\alpha\alpha \\ N_\beta\beta + N_{\delta r}\delta r \end{pmatrix}.$$

The various coefficients, such as $\mathcal{L}_\alpha$ and N_β, depend on the vehicle's speed, through the dynamic pressure, the geometry, and the Reynolds number. The matrix $\boldsymbol{D}_\omega$ contains terms which characterize viscous angular damping (such as pitch and yaw damping). The expressions above reflect several common assumptions:

- The zero-β side force vanishes.
- The zero-α lift force vanishes and the zero-α viscous pitch moment is zero.
- The viscous lift and side forces are linear in α and β, respectively.
- The viscous drag force is quadratic in lift (and therefore in α).

Equations (2.1), (2.2), and (2.5) completely describe the motion of a rigid underwater glider in inertial space. In studying steady motions, we typically neglect the translational kinematics (2.1). Moreover, the structure of the dynamic equations (2.5) is such that we only need to retain a portion of the rotational kinematics (2.2). Given the "tilt" vector $\boldsymbol{\zeta} = \boldsymbol{\mathcal{R}}_{\mathrm{IB}}^T \boldsymbol{i}_3$, which is simply the body frame unit vector pointing in the direction of gravity, and referring to equation (2.2), it is easy to see that $\dot{\boldsymbol{\zeta}} = \boldsymbol{\zeta} \times \boldsymbol{\omega}$. The reduced set of dynamic equations, with buoyancy control and moving mass actuator dynamics explicitly represented, are:

$$\begin{aligned}
\dot{\boldsymbol{h}}_{\mathrm{sys}} &= \boldsymbol{h}_{\mathrm{sys}} \times \boldsymbol{\omega} + \boldsymbol{p}_{\mathrm{sys}} \times \boldsymbol{v} + (m_{\mathrm{rb}} g \boldsymbol{r}_{\mathrm{rb}} + m_{\mathrm{p_x}} g \boldsymbol{r}_{\mathrm{p_x}} + m_{\mathrm{p_y}} g \boldsymbol{r}_{\mathrm{p_y}}) \times \boldsymbol{\zeta} + \boldsymbol{T}_{\mathrm{visc}} \\
\dot{\boldsymbol{p}}_{\mathrm{sys}} &= \boldsymbol{p}_{\mathrm{sys}} \times \boldsymbol{\omega} + \tilde{m} g \boldsymbol{\zeta} + \boldsymbol{F}_{\mathrm{visc}} \\
\dot{\boldsymbol{\zeta}} &= \boldsymbol{\zeta} \times \boldsymbol{\omega} \\
\dot{p}_{\mathrm{p_x}} &= u_{\mathrm{p_x}} \\
\dot{p}_{\mathrm{p_y}} &= u_{\mathrm{p_y}} \\
\dot{m}_{\mathrm{b}} &= u_{\mathrm{b}}
\end{aligned} \tag{2.6}$$

Equations (2.6) are written in mixed velocity/momentum notation. To design a control system, we convert these into a consistent set of state variables by computing

$$\dot{\boldsymbol{\eta}} = \mathbb{M}^{-1} \dot{\boldsymbol{\nu}} - \mathbb{M}^{-1} \dot{\mathbb{M}} \;\; \mathbb{M}^{-1} \boldsymbol{\nu} \tag{2.7}$$

where in (2.7), $\mathbb{M}^{-1}$ is the inverse of generalized inertia and $\dot{\mathbb{M}}$ is the time derivative of it:

$$\dot{\mathbb{M}} = \begin{pmatrix} \dot{\boldsymbol{I}} & \dot{\boldsymbol{C}} & m_{\mathrm{p_x}} \dot{\hat{\boldsymbol{r}}}_{\mathrm{p_x}} \boldsymbol{e}_1 & m_{\mathrm{p_y}} \dot{\hat{\boldsymbol{r}}}_{\mathrm{p_y}} \boldsymbol{e}_2 \\ \dot{\boldsymbol{C}}^T & \mathbb{O}_{3\times 3} & 0\boldsymbol{e}_1 & 0\boldsymbol{e}_2 \\ -m_{\mathrm{p_x}} \boldsymbol{e}_1^T \dot{\hat{\boldsymbol{r}}}_{\mathrm{p_x}} & 0\boldsymbol{e}_1^T & 0 & 0 \\ -m_{\mathrm{p_y}} \boldsymbol{e}_2^T \dot{\hat{\boldsymbol{r}}}_{\mathrm{p_y}} & 0\boldsymbol{e}_2^T & 0 & 0 \end{pmatrix}$$

with

$$\begin{aligned}
\dot{\boldsymbol{I}} &= -m_{\mathrm{p_x}} (\hat{\boldsymbol{r}}_{\mathrm{p_x}} \dot{\hat{\boldsymbol{r}}}_{\mathrm{p_x}} + \dot{\hat{\boldsymbol{r}}}_{\mathrm{p_x}} \hat{\boldsymbol{r}}_{\mathrm{p_x}}) - m_{\mathrm{p_y}} (\hat{\boldsymbol{r}}_{\mathrm{p_y}} \dot{\hat{\boldsymbol{r}}}_{\mathrm{p_y}} + \dot{\hat{\boldsymbol{r}}}_{\mathrm{p_y}} \hat{\boldsymbol{r}}_{\mathrm{p_y}}) \\
\dot{\boldsymbol{C}} &= m_{\mathrm{p_x}} \dot{\hat{\boldsymbol{r}}}_{\mathrm{p_x}} + m_{\mathrm{p_y}} \dot{\hat{\boldsymbol{r}}}_{\mathrm{p_y}}.
\end{aligned}$$

2.1.1 Simplified Vehicle Dynamic Model with Rectilinear Actuator Dynamics

As explained in Section 2.1, it is notationally convenient to compile the various inertia matrices into the *generalized* inertia matrix shown in Table 2.1. From that we have

$$\mathbb{M}_{\mathrm{rb/p/b}} = \begin{pmatrix} & \boldsymbol{I}_{\mathrm{rb/p/b}} & & \boldsymbol{C}_{\mathrm{rb/p/b}} & \begin{pmatrix} 0 \\ 0 \\ 0 \end{pmatrix} & \begin{pmatrix} 0 \\ 0 \\ 0 \end{pmatrix} \\ & \boldsymbol{C}^T_{\mathrm{rb/p/b}} & & \boldsymbol{M}_{\mathrm{rb/p/b}} & \begin{pmatrix} m_{\mathrm{p_x}} \\ 0 \\ 0 \end{pmatrix} & \begin{pmatrix} 0 \\ m_{\mathrm{p_y}} \\ 0 \end{pmatrix} \\ \begin{pmatrix} 0 & 0 & 0 \\ 0 & 0 & 0 \end{pmatrix} & & \begin{pmatrix} m_{\mathrm{p_x}} & 0 & 0 \\ 0 & m_{\mathrm{p_y}} & 0 \end{pmatrix} & & m_{\mathrm{p_x}} & 0 \\ & & & & 0 & m_{\mathrm{p_y}} \end{pmatrix}$$

The generalized *added* inertia matrix is composed of the added mass matrix $\boldsymbol{M}_{\mathrm{f}}$, the added inertia matrix $\boldsymbol{I}_{\mathrm{f}}$, and the added inertial coupling matrix $\boldsymbol{C}_{\mathrm{f}}$:

$$\mathbb{M}_{\mathrm{f}} = \begin{pmatrix} \boldsymbol{I}_{\mathrm{f}} & \boldsymbol{C}_{\mathrm{f}} & \mathbb{O}_{3\times 2} \\ \boldsymbol{C}^T_{\mathrm{f}} & \boldsymbol{M}_{\mathrm{f}} & \mathbb{O}_{3\times 2} \\ \mathbb{O}_{2\times 3} & \mathbb{O}_{2\times 3} & \mathbb{O}_{2\times 2} \end{pmatrix}$$

The added inertia accounts for energy necessary to accelerate the fluid as the body rotates. If the underwater glider's external geometry is such that the $\boldsymbol{b}_1$-$\boldsymbol{b}_2$ and $\boldsymbol{b}_1$-$\boldsymbol{b}_3$ planes are planes of symmetry, the added inertia matrix is diagonal:

$$\boldsymbol{I}_{\mathrm{f}} = -\mathrm{diag}\begin{pmatrix} L_{\dot{p}} & M_{\dot{q}} & N_{\dot{r}} \end{pmatrix}.$$

The added mass matrix accounts for the energy necessary to accelerate the fluid as the body translates. Like the added inertia matrix, the added mass matrix is diagonal for the class of underwater gliders considered here:

$$\boldsymbol{M}_{\mathrm{f}} = -\mathrm{diag}\begin{pmatrix} X_{\dot{u}} & Y_{\dot{v}} & Z_{\dot{w}} \end{pmatrix}.$$

In addition to the added inertia and the added mass, there will generally be potential flow and inertial coupling between translational and rotational kinetic energy. For the class of underwater gliders considered here,

$$\boldsymbol{C}_{\mathrm{f}} = -\begin{pmatrix} 0 & 0 & 0 \\ 0 & 0 & M_{\dot{w}} \\ 0 & N_{\dot{v}} & 0 \end{pmatrix} = -\begin{pmatrix} 0 & 0 & 0 \\ 0 & 0 & Y_{\dot{r}} \\ 0 & Z_{\dot{q}} & 0 \end{pmatrix}^{T}.$$

We note that the terms appearing in $\boldsymbol{C}_{\mathrm{f}}$ do not appear in previous glider analysis, although they can be significant.

The generalized inertia for the vehicle/fluid system is

$$\mathbb{M} = \mathbb{M}_{\mathrm{rb/p/b}} + \mathbb{M}_{\mathrm{f}} \tag{2.8}$$

and recall that

$$\begin{aligned} \boldsymbol{I} &= \boldsymbol{I}_{\mathrm{rb/p/b}} + \boldsymbol{I}_{\mathrm{f}} \\ \boldsymbol{M} &= \boldsymbol{M}_{\mathrm{rb/p/b}} + \boldsymbol{M}_{\mathrm{f}} \\ \boldsymbol{C} &= \boldsymbol{C}_{\mathrm{rb/p/b}} + \boldsymbol{C}_{\mathrm{f}}. \end{aligned}$$

Defining the generalized velocity $\boldsymbol{\eta}$ and the generalized momentum $\boldsymbol{\nu}$ as in Table 2.2, we have

$$\boldsymbol{h}_{\mathrm{sys}} = \boldsymbol{I}\boldsymbol{\omega} + \boldsymbol{C}\boldsymbol{v} + 0\dot{\boldsymbol{r}}_{\mathrm{p_x}} + 0\dot{\boldsymbol{r}}_{\mathrm{p_y}} \tag{2.9}$$

$$\boldsymbol{p}_{\mathrm{sys}} = \boldsymbol{M}\boldsymbol{v} + \boldsymbol{C}^{T}\boldsymbol{\omega} + m_{\mathrm{p_x}}\dot{\boldsymbol{r}}_{\mathrm{p_x}} + m_{\mathrm{p_y}}\dot{\boldsymbol{r}}_{\mathrm{p_y}} \tag{2.10}$$

$$\begin{aligned} p_{\mathrm{p_x}} &= m_{\mathrm{p_x}}\boldsymbol{e}_1 \cdot (\boldsymbol{v} + \boldsymbol{\omega} \times \boldsymbol{r}_{\mathrm{p_x}} + \dot{\boldsymbol{r}}_{\mathrm{p_x}}) \\ &= m_{\mathrm{p_x}}\boldsymbol{e}_1 \cdot (\boldsymbol{v} + \dot{\boldsymbol{r}}_{\mathrm{p_x}}) \Rightarrow m_{\mathrm{p_x}}\dot{\boldsymbol{r}}_{\mathrm{p_x}} = \boldsymbol{e}_1(p_{\mathrm{p_x}} - m_{\mathrm{p_x}}\boldsymbol{e}_1 \cdot \boldsymbol{v}) \end{aligned} \tag{2.11}$$

$$\begin{aligned} p_{\mathrm{p_y}} &= m_{\mathrm{p_y}}\boldsymbol{e}_2 \cdot (\boldsymbol{v} + \boldsymbol{\omega} \times \boldsymbol{r}_{\mathrm{p_y}} + \dot{\boldsymbol{r}}_{\mathrm{p_y}}) \\ &= m_{\mathrm{p_y}}\boldsymbol{e}_2 \cdot (\boldsymbol{v} + \dot{\boldsymbol{r}}_{\mathrm{p_y}}) \Rightarrow m_{\mathrm{p_y}}\dot{\boldsymbol{r}}_{\mathrm{p_y}} = \boldsymbol{e}_2(p_{\mathrm{p_y}} - m_{\mathrm{p_y}}\boldsymbol{e}_2 \cdot \boldsymbol{v}). \end{aligned} \tag{2.12}$$

From there, we can substitute equations (2.11) and (2.12) into equation (2.10) and obtain

$$\begin{aligned} \boldsymbol{h}_{\text{sys}} &= \boldsymbol{I}\boldsymbol{\omega} + \boldsymbol{C}\boldsymbol{v} \\ \boldsymbol{p}_{\text{sys}} &= (\boldsymbol{M} - [m_{\text{p}_\text{x}}\boldsymbol{e}_1\boldsymbol{e}_1^T + m_{\text{p}_\text{y}}\boldsymbol{e}_2\boldsymbol{e}_2^T])\boldsymbol{v} + \boldsymbol{C}^T\boldsymbol{\omega} + (\boldsymbol{e}_1 p_{\text{p}_\text{x}} + \boldsymbol{e}_2 p_{\text{p}_\text{y}}) \\ p_{\text{p}_\text{x}} &= m_{\text{p}_\text{x}}\boldsymbol{e}_1 \cdot (\boldsymbol{v} + \dot{\boldsymbol{r}}_{\text{p}_\text{x}}) \\ p_{\text{p}_\text{y}} &= m_{\text{p}_\text{y}}\boldsymbol{e}_2 \cdot (\boldsymbol{v} + \dot{\boldsymbol{r}}_{\text{p}_\text{y}}). \end{aligned} \tag{2.13}$$

Defining $\boldsymbol{p}_{\text{rb/f}} = \boldsymbol{p}_{\text{sys}} - (\boldsymbol{e}_1 p_{\text{p}_\text{x}} + \boldsymbol{e}_2 p_{\text{p}_\text{y}})$, we have

$$\begin{aligned} \begin{pmatrix} \boldsymbol{h}_{\text{sys}} \\ \boldsymbol{p}_{\text{rb/f}} \end{pmatrix} &= \begin{pmatrix} \boldsymbol{I} & \boldsymbol{C} \\ \boldsymbol{C}^T & (\boldsymbol{M} - [m_{\text{p}_\text{x}}\boldsymbol{e}_1\boldsymbol{e}_1^T + m_{\text{p}_\text{y}}\boldsymbol{e}_2\boldsymbol{e}_2^T]) \end{pmatrix} \begin{pmatrix} \boldsymbol{\omega} \\ \boldsymbol{v} \end{pmatrix} \\ p_{\text{p}_\text{x}} &= m_{\text{p}_\text{x}}\boldsymbol{e}_1 \cdot (\boldsymbol{v} + \dot{\boldsymbol{r}}_{\text{p}_\text{x}}) \\ p_{\text{p}_\text{y}} &= m_{\text{p}_\text{y}}\boldsymbol{e}_2 \cdot (\boldsymbol{v} + \dot{\boldsymbol{r}}_{\text{p}_\text{y}}) \end{aligned} \tag{2.14}$$

Let's call $\mathbb{M}_{\mathbb{I}} = \begin{pmatrix} \boldsymbol{I} & \boldsymbol{C} \\ \boldsymbol{C}^T & (\boldsymbol{M} - [m_{\text{p}_\text{x}}\boldsymbol{e}_1\boldsymbol{e}_1^T + m_{\text{p}_\text{y}}\boldsymbol{e}_2\boldsymbol{e}_2^T]) \end{pmatrix}$.

To design a control system, we convert dynamic equations (2.6), presented in mixed velocity/momentum notation, into a consistent set of state variables considering set of equations (2.14) into the following form:

$$\begin{pmatrix} \dot{\boldsymbol{\omega}} \\ \dot{\boldsymbol{v}} \end{pmatrix} = \mathbb{M}_{\mathbb{I}}{}^{-1} \begin{pmatrix} \dot{\boldsymbol{h}}_{\text{sys}} \\ \dot{\boldsymbol{p}}_{\text{rb/f}} \end{pmatrix} - \mathbb{M}_{\mathbb{I}}{}^{-1}\dot{\mathbb{M}}_{\mathbb{I}}\mathbb{M}_{\mathbb{I}}{}^{-1} \begin{pmatrix} \boldsymbol{h}_{\text{sys}} \\ \boldsymbol{p}_{\text{rb/f}} \end{pmatrix} \tag{2.15}$$

$$\dot{r}_{\text{p}_\text{x}} = \boldsymbol{e}_1 \cdot (\boldsymbol{v}_{\text{p}_\text{x}} - \boldsymbol{v} - \boldsymbol{\omega} \times \boldsymbol{r}_{\text{p}_\text{x}}) \tag{2.16}$$

$$\dot{v}_{\text{p}_\text{x}} = \frac{u_{\text{p}_\text{x}}}{m_{\text{p}_\text{x}}} + \boldsymbol{e}_1 \cdot (\dot{\boldsymbol{v}} + \dot{\boldsymbol{\omega}} \times \boldsymbol{r}_{\text{p}_\text{x}} + \boldsymbol{\omega} \times \dot{\boldsymbol{r}}_{\text{p}_\text{x}}) \tag{2.17}$$

$$\dot{r}_{\text{p}_\text{y}} = \boldsymbol{e}_2 \cdot \left(\boldsymbol{v}_{\text{p}_\text{y}} - \boldsymbol{v} - \boldsymbol{\omega} \times \boldsymbol{r}_{\text{p}_\text{y}}\right) \tag{2.18}$$

$$\dot{v}_{\text{p}_\text{y}} = \frac{u_{\text{p}_\text{y}}}{m_{\text{p}_\text{y}}} + \boldsymbol{e}_2 \cdot \left(\dot{\boldsymbol{v}} + \dot{\boldsymbol{\omega}} \times \boldsymbol{r}_{\text{p}_\text{y}} + \boldsymbol{\omega} \times \dot{\boldsymbol{r}}_{\text{p}_\text{y}}\right), \tag{2.19}$$

where in equation (2.15), $\dot{\boldsymbol{p}}_{\text{rb/f}} = \dot{\boldsymbol{p}}_{\text{sys}} - (\boldsymbol{e}_1 u_{\text{p}_\text{x}} + \boldsymbol{e}_2 u_{\text{p}_\text{y}})$ and

$$\dot{\mathbb{M}}_{\mathbb{I}} = \begin{pmatrix} -2(m_{\text{p}_\text{x}}\hat{\boldsymbol{r}}_{\text{p}_\text{x}}\dot{\hat{\boldsymbol{r}}}_{\text{p}_\text{x}} + m_{\text{p}_\text{y}}\hat{\boldsymbol{r}}_{\text{p}_\text{y}}\dot{\hat{\boldsymbol{r}}}_{\text{p}_\text{y}}) & m_{\text{p}_\text{x}}\dot{\hat{\boldsymbol{r}}}_{\text{p}_\text{x}} + m_{\text{p}_\text{y}}\dot{\hat{\boldsymbol{r}}}_{\text{p}_\text{y}} \\ -(m_{\text{p}_\text{x}}\dot{\boldsymbol{r}}_{\text{p}_\text{x}} + m_{\text{p}_\text{y}}\dot{\boldsymbol{r}}_{\text{p}_\text{y}}) & \mathbb{O}_{3\times 3} \end{pmatrix}.$$

2.1.2 Vehicle Dynamic Model with Fixed Actuators

Underwater gliders are so efficient because they spend much of their flight time in stable, steady motion. In studying steady motions, we do not consider the internal dynamics of the moving mass actuators. In determining a nominal wings-level glide condition, we assume that longitudinal moving mass is located at the origin of body fixed reference frame ($r_{\mathrm{p_x}} = 0$). This means that the nominal gravitational moment is due entirely to center of gravity (CG) location (r_{rb}). For simplicity, we assume that $\boldsymbol{r}_{\mathrm{rb}} \cdot \boldsymbol{e}_2 = 0$, so that the vehicle center of mass (less the contribution of m_{p}) is located in the $\boldsymbol{b}_1$-$\boldsymbol{b}_3$ plane, and we assume that $\boldsymbol{r}_{\mathrm{p}} = r_{\mathrm{p}}\boldsymbol{e}_2$, so that the mass m_{p} is located somewhere along the $\boldsymbol{b}_2$-axis.

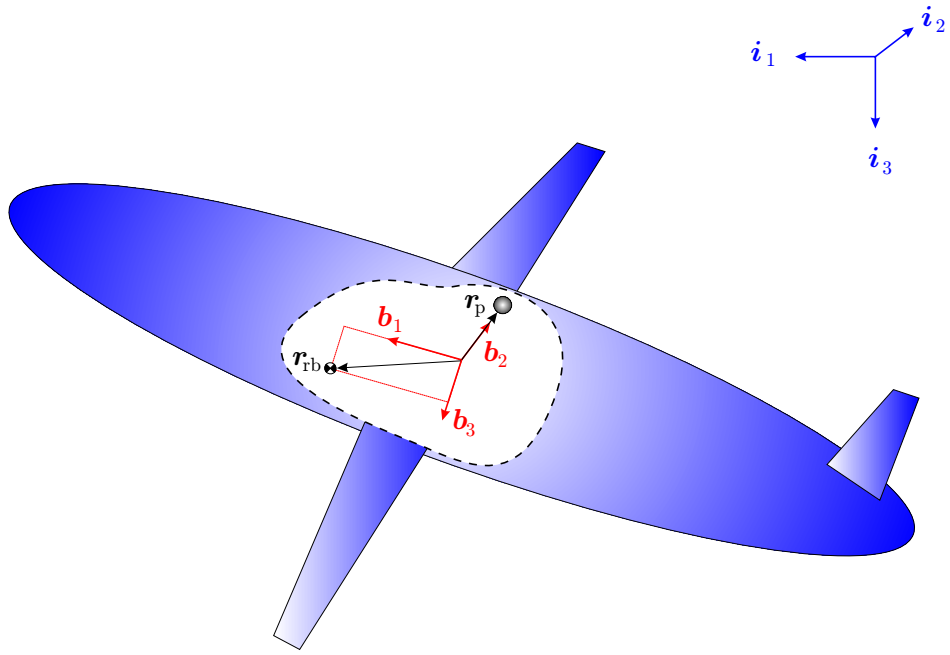

Figure 2.4 Reference frames.

Referring to Figure 2.4, the kinematic equations are

$$\dot{\boldsymbol{y}} = \boldsymbol{\mathcal{R}}_{\mathrm{IB}}\boldsymbol{v} \tag{2.20}$$

$$\dot{\boldsymbol{\mathcal{R}}}_{\mathrm{IB}} = \boldsymbol{\mathcal{R}}_{\mathrm{IB}}\hat{\boldsymbol{\omega}} \tag{2.21}$$

The angular momentum of the body/fluid system about the body frame origin is denoted by the body vector $\boldsymbol{h}$. The linear momentum of the body/fluid system is denoted by the

body vector $\boldsymbol{p}$. The vectors $\boldsymbol{h}$ and $\boldsymbol{p}$ are the conjugate momenta corresponding to $\boldsymbol{\omega}$ and $\boldsymbol{v}$, respectively. To develop expressions for $\boldsymbol{h}$ and $\boldsymbol{p}$ in terms of $\boldsymbol{\omega}$ and $\boldsymbol{v}$ requires a number of definitions.

The inertia matrix $\boldsymbol{I}$ is the sum of three components: the *added inertia matrix* $\boldsymbol{I}_{\mathrm{f}}$, the *rigid body inertia matrix* $\boldsymbol{I}_{\mathrm{rb}}$, and a third matrix $-m_{\mathrm{p}}\hat{\boldsymbol{r}}_{\mathrm{p}}\hat{\boldsymbol{r}}_{\mathrm{p}}$.

$$\boldsymbol{I} = \boldsymbol{I}_{\mathrm{f}} + \boldsymbol{I}_{\mathrm{rb}} - m_{\mathrm{p}}\hat{\boldsymbol{r}}_{\mathrm{p}}\hat{\boldsymbol{r}}_{\mathrm{p}}.$$

The mass matrix $\boldsymbol{M}$ is the sum of the *added mass matrix* $\boldsymbol{M}_{\mathrm{f}}$ and $m_{\mathrm{v}}\mathbb{1}$:

$$\boldsymbol{M} = \boldsymbol{M}_{\mathrm{f}} + m_{\mathrm{v}}\mathbb{1}.$$

In addition to the added inertia and the added mass, there will generally be potential flow and inertial coupling between translational and rotational kinetic energy. The coupling is characterized by the matrix $\boldsymbol{C} = \boldsymbol{C}_{\mathrm{f}} + \boldsymbol{C}_{\mathrm{rb}}$, where

$$\boldsymbol{C}_{\mathrm{rb}} = m_{\mathrm{rb}}\hat{\boldsymbol{r}}_{\mathrm{rb}} + m_{\mathrm{p}}\hat{\boldsymbol{r}}_{\mathrm{p}} = -\boldsymbol{C}_{\mathrm{rb}}^{T}.$$

The combined rigid body and fluid kinetic energy is therefore

$$\begin{aligned} T &= T_{\mathrm{f}} + T_{\mathrm{rb}} \\ &= \frac{1}{2}\begin{pmatrix} \boldsymbol{v} \\ \boldsymbol{\omega} \end{pmatrix}^{T} \begin{pmatrix} \boldsymbol{M}_{\mathrm{f}} & \boldsymbol{C}_{\mathrm{f}}^{T} \\ \boldsymbol{C}_{\mathrm{f}} & \boldsymbol{I}_{\mathrm{f}} \end{pmatrix} \begin{pmatrix} \boldsymbol{v} \\ \boldsymbol{\omega} \end{pmatrix} + \frac{1}{2}\begin{pmatrix} \boldsymbol{v} \\ \boldsymbol{\omega} \end{pmatrix}^{T} \begin{pmatrix} \boldsymbol{M}_{\mathrm{rb}} & \boldsymbol{C}_{\mathrm{rb}}^{T} \\ \boldsymbol{C}_{\mathrm{rb}} & \boldsymbol{I}_{\mathrm{rb}} \end{pmatrix} \begin{pmatrix} \boldsymbol{v} \\ \boldsymbol{\omega} \end{pmatrix} \\ &= \frac{1}{2}\begin{pmatrix} \boldsymbol{v} \\ \boldsymbol{\omega} \end{pmatrix}^{T} \begin{pmatrix} \boldsymbol{M} & \boldsymbol{C}^{T} \\ \boldsymbol{C} & \boldsymbol{I} \end{pmatrix} \begin{pmatrix} \boldsymbol{v} \\ \boldsymbol{\omega} \end{pmatrix}. \end{aligned}$$

The momenta $\boldsymbol{h}$ and $\boldsymbol{p}$ are defined by the kinetic energy metric and the velocities $\boldsymbol{\omega}$ and $\boldsymbol{v}$:

$$\begin{pmatrix} \boldsymbol{p} \\ \boldsymbol{h} \end{pmatrix} = \begin{pmatrix} \partial T/\partial \boldsymbol{v} \\ \partial T/\partial \boldsymbol{\omega} \end{pmatrix} = \begin{pmatrix} \boldsymbol{M} & \boldsymbol{C}^{T} \\ \boldsymbol{C} & \boldsymbol{I} \end{pmatrix} \begin{pmatrix} \boldsymbol{v} \\ \boldsymbol{\omega} \end{pmatrix}. \tag{2.22}$$

The dynamic equations, which relate external forces and moments to the rate of change of linear and angular momentum, are

$$\dot{\boldsymbol{p}} = \boldsymbol{p} \times \boldsymbol{\omega} + \tilde{m} g \left(\boldsymbol{\mathcal{R}}_{\mathrm{IB}}^T \boldsymbol{i}_3 \right) + \boldsymbol{F}_{\mathrm{visc}} \tag{2.23}$$

$$\dot{\boldsymbol{h}} = \boldsymbol{h} \times \boldsymbol{\omega} + \boldsymbol{p} \times \boldsymbol{v} + (m_{\mathrm{p}} g \boldsymbol{r}_{\mathrm{p}} + m_{\mathrm{rb}} g \boldsymbol{r}_{\mathrm{rb}}) \times \left(\boldsymbol{\mathcal{R}}_{\mathrm{IB}}^T \boldsymbol{i}_3 \right) + \boldsymbol{T}_{\mathrm{visc}}. \tag{2.24}$$

Equations (2.20), (2.21), (2.23), and (2.24) completely describe the motion of a rigid underwater glider with fixed actuators in inertial space. As explained previously in studying steady motions, given the tilt vector $\boldsymbol{\zeta} = \boldsymbol{\mathcal{R}}_{\mathrm{IB}}^T \boldsymbol{i}_3$, we consider the following reduced set of equations:

$$\dot{\boldsymbol{\zeta}} = \boldsymbol{\zeta} \times \boldsymbol{\omega} \tag{2.25}$$

$$\dot{\boldsymbol{p}} = \boldsymbol{p} \times \boldsymbol{\omega} + \tilde{m} g \boldsymbol{\zeta} + \boldsymbol{F}_{\mathrm{visc}} \tag{2.26}$$

$$\dot{\boldsymbol{h}} = \boldsymbol{h} \times \boldsymbol{\omega} + \boldsymbol{p} \times \boldsymbol{v} + (m_{\mathrm{p}} g \boldsymbol{r}_{\mathrm{p}} + m_{\mathrm{rb}} g \boldsymbol{r}_{\mathrm{rb}}) \times \boldsymbol{\zeta} + \boldsymbol{T}_{\mathrm{visc}}. \tag{2.27}$$

2.2 Vehicle Dynamic Model with Cylindrical Actuator Dynamics

Figure 2.5 depicts a rigid body (mass m_{rb}) of a glider such as *Seaglider* with a moving mass actuator (m_{p}) and a variable ballast actuator (m_{b}). The total vehicle mass is

$$m_{\mathrm{v}} = m_{\mathrm{rb}} + m_{\mathrm{p}} + m_{\mathrm{b}}.$$

As indicated in Figure 2.5, the variable mass m_{b} is located at the origin of a body-fixed reference frame. The mass particle m_{p} is constrained to move along the longitudinal axis ($\boldsymbol{r}_{\mathrm{p_x}} = r_{\mathrm{p_x}} \boldsymbol{e}_1$) and a circle (with radius R_{p}) in the vertical plane:

$$\begin{aligned} \boldsymbol{r}_{\mathrm{p}} &= r_{\mathrm{p_x}} \boldsymbol{e}_1 + R_{\mathrm{p}} (\sin \xi \boldsymbol{e}_2 + \cos \xi \boldsymbol{e}_3) \\ \boldsymbol{\omega}_{\mathrm{p}} &= \dot{\xi} \boldsymbol{e}_1 \end{aligned}$$

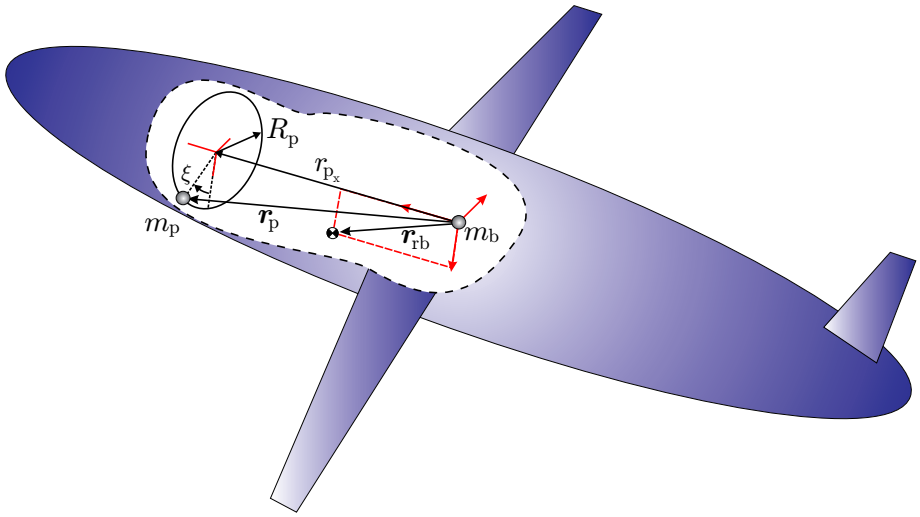

Figure 2.5 Illustration of point mass actuators.

Define:

$$\boldsymbol{e}_r = \sin\xi\boldsymbol{e}_2 + \cos\xi\boldsymbol{e}_3 \quad \text{and} \quad \boldsymbol{e}_\xi = \cos\xi\boldsymbol{e}_2 - \sin\xi\boldsymbol{e}_3.$$

Hence, in the body frame

$$\begin{aligned} \boldsymbol{r}_\mathrm{p} &= \boldsymbol{r}_{\mathrm{p_x}} + R_\mathrm{p}\boldsymbol{e}_r \\ \boldsymbol{\omega}_\mathrm{p} &= \dot{\xi}\boldsymbol{e}_1, \end{aligned} \tag{2.28}$$

so the velocity of m_p relative to the body is

$$\dot{\boldsymbol{r}}_\mathrm{p} = \dot{\boldsymbol{r}}_{\mathrm{p_x}} + \hat{\boldsymbol{r}}_\mathrm{p}\boldsymbol{\omega}_\mathrm{p}, \tag{2.29}$$

where $\hat{\boldsymbol{r}}_\mathrm{p}\boldsymbol{\omega}_\mathrm{p} = R_\mathrm{p}\dot{\xi}\boldsymbol{e}_\xi$.

Let the body vector $\boldsymbol{v}_\mathrm{p}$ denote the velocity of the moving mass particle with respect to inertial space. The kinematic equation for moving mass is

$$\dot{\boldsymbol{X}}_\mathrm{p} = \boldsymbol{\mathcal{R}}_\mathrm{IB}\boldsymbol{v}_\mathrm{p}.$$

Referring to Figure 2.6, let the inertial vector $\boldsymbol{R}_\mathrm{p} = \boldsymbol{X}_\mathrm{p} - \boldsymbol{X}$ denote the position of the mass particle relative to the origin of the body frame. An alternative kinematic equation for the moving mass is

$$\dot{\boldsymbol{R}}_\mathrm{p} = \boldsymbol{\mathcal{R}}_\mathrm{IB}(\boldsymbol{v}_\mathrm{p} - \boldsymbol{v}).$$

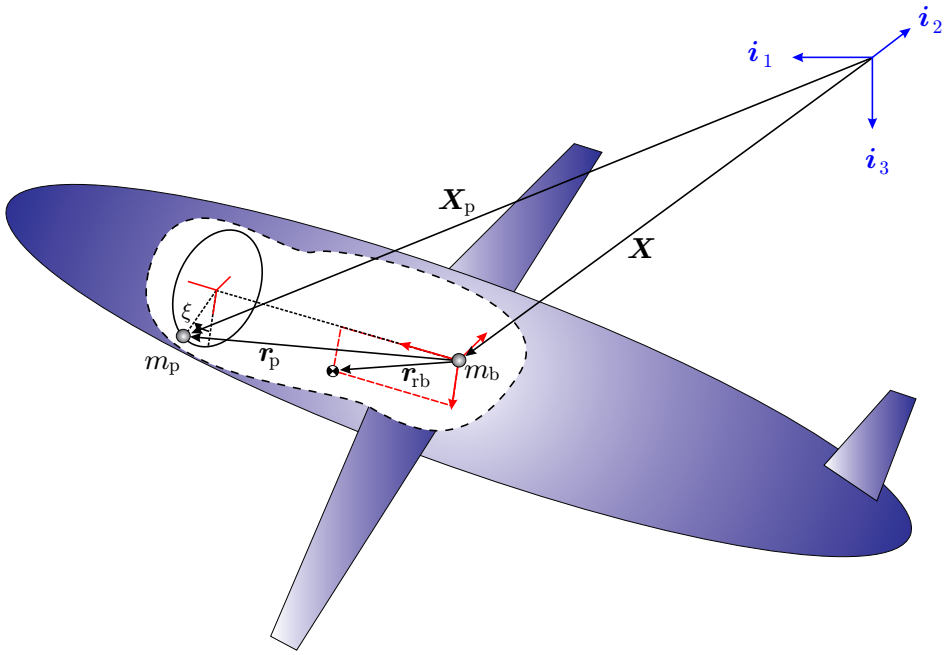

Figure 2.6 Illustration of point mass actuators.

Finally, define $\boldsymbol{r}_\mathrm{p} = \boldsymbol{\mathcal{R}}_\mathrm{IB}^T \boldsymbol{R}_\mathrm{p}$ to be the vector $\boldsymbol{R}_\mathrm{p}$ expressed in the body frame. This gives the kinematic equation for moving mass particle

$$\begin{aligned} \dot{\boldsymbol{r}}_\mathrm{p} &= \dot{\boldsymbol{\mathcal{R}}}_\mathrm{IB}^T \boldsymbol{R}_\mathrm{p} + \boldsymbol{\mathcal{R}}_\mathrm{IB}^T (\dot{\boldsymbol{X}}_\mathrm{p} - \dot{\boldsymbol{X}}) \\ &= \hat{\boldsymbol{r}}_\mathrm{p} \boldsymbol{\omega} + \boldsymbol{v}_\mathrm{p} - \boldsymbol{v} \end{aligned}$$

Then, the velocity of the moving mass particle with respect to inertial frame is

$$\boldsymbol{v}_\mathrm{p} = \boldsymbol{v} - \hat{\boldsymbol{r}}_\mathrm{p} \boldsymbol{\omega} + \dot{\boldsymbol{r}}_\mathrm{p},$$

and substituting $\dot{\boldsymbol{r}}_\mathrm{p}$ from equation (2.29) gives

$$\boldsymbol{v}_\mathrm{p} = \boldsymbol{v} - \hat{\boldsymbol{r}}_\mathrm{p} \boldsymbol{\omega} + \dot{\boldsymbol{r}}_{\mathrm{p_x}} - \hat{\boldsymbol{r}}_\mathrm{p} \boldsymbol{\omega}_\mathrm{p}. \tag{2.30}$$

Considering the moving mass actuator as a rectangular block with uniformly distributed mass instead of the particle mass, we need to include the angular momentum of the block itself about its own center of mass:

$$\boldsymbol{I}_\mathrm{p}(\xi) = \boldsymbol{R}_{b_1}(\xi)^T \boldsymbol{I}_\mathrm{block} \boldsymbol{R}_{b_1}(\xi),$$

where $\boldsymbol{I}_{\text{block}}$ represents the principal inertia matrix for the block. Assuming $a \times b \times L$ dimensions along (b_1, b_2, b_3) axis,

$$\boldsymbol{I}_{\text{block}} = \begin{pmatrix} \frac{m}{12}(b^2+L^2) & 0 & 0 \\ 0 & \frac{m}{12}(a^2+L^2) & 0 \\ 0 & 0 & \frac{m}{12}(a^2+b^2) \end{pmatrix},$$

and $\boldsymbol{R}_{b_1}(\xi)$ is a planar rotation about the body's longitudinal axis,

$$\boldsymbol{R}_{b_1}(\xi) = \begin{pmatrix} 1 & 0 & 0 \\ 0 & \cos\xi & \sin\xi \\ 0 & -\sin\xi & \cos\xi \end{pmatrix}.$$

Hence the moving mass kinetic energy is

$$T_{\text{p}} = \frac{1}{2} m_{\text{p}} \boldsymbol{v}_{\text{p}}^2 + \frac{1}{2} \boldsymbol{I}_{\text{p}}(\xi)(\boldsymbol{\omega} + \boldsymbol{\omega}_{\text{p}})^2.$$

Generalized Velocity ($\boldsymbol{\eta}$)	Generalized Momentum ($\boldsymbol{\nu}$)
$\begin{pmatrix} \boldsymbol{\omega} \\ \boldsymbol{v} \\ \boldsymbol{\omega}_{\text{p}} \\ \dot{\boldsymbol{r}}_{\text{px}} \end{pmatrix}$	$\begin{pmatrix} \boldsymbol{h}_{\text{sys}} \\ \boldsymbol{p}_{\text{sys}} \\ \boldsymbol{h}_{\text{p}} \\ \boldsymbol{p}_{\text{p}} \end{pmatrix}$

Table 2.3 Generalized velocity and momentum.

Defining the generalized velocity $\boldsymbol{\eta}$ and the generalized momentum $\boldsymbol{\nu}$ as in Table 2.3, we have

$$T_{\text{p}} = \frac{1}{2} \boldsymbol{\eta}^T \mathbb{M}_{\text{p}} \boldsymbol{\eta}, \tag{2.31}$$

where $\mathbb{M}_{\text{p}}$ is presented in Table 2.4. The kinetic energy of the rigid-body/moving mass system is

$$T_{\text{rb/p/b}} = \frac{1}{2} \boldsymbol{\eta}^T \mathbb{M}_{\text{rb/p/b}} \boldsymbol{\eta}. \tag{2.32}$$

Generalized Moving Mass Inertia $\mathbb{M}_{\rm p}$

$$\begin{pmatrix} \boldsymbol{I}_{\rm p}(\xi) - m_{\rm p}\hat{\boldsymbol{r}}_{\rm p}\hat{\boldsymbol{r}}_{\rm p} & m_{\rm p}\hat{\boldsymbol{r}}_{\rm p} & \boldsymbol{I}_{\rm p}(\xi) + m_{\rm p}\hat{\boldsymbol{r}}_{\rm p}\hat{\boldsymbol{r}}_{\rm p} & m_{\rm p}\hat{\boldsymbol{r}}_{\rm p} \\ -m_{\rm p}\hat{\boldsymbol{r}}_{\rm p} & m_{\rm p}\mathbb{1} & m_{\rm p}\hat{\boldsymbol{r}}_{\rm p} & m_{\rm p}\mathbb{1} \\ \boldsymbol{I}_{\rm p}(\xi) + m_{\rm p}\hat{\boldsymbol{r}}_{\rm p}\hat{\boldsymbol{r}}_{\rm p} & -m_{\rm p}\hat{\boldsymbol{r}}_{\rm p} & \boldsymbol{I}_{\rm p}(\xi) - m_{\rm p}\hat{\boldsymbol{r}}_{\rm p}\hat{\boldsymbol{r}}_{\rm p} & -m_{\rm p}\hat{\boldsymbol{r}}_{\rm p} \\ -m_{\rm p}\hat{\boldsymbol{r}}_{\rm p} & m_{\rm p}\mathbb{1} & m_{\rm p}\hat{\boldsymbol{r}}_{\rm p} & m_{\rm p}\mathbb{1} \end{pmatrix}$$

Table 2.4 Moving mass generalized inertia matrix.

Then the mass, inertia, and inertial coupling matrices for the combined rigid body/moving mass/variable ballast system is

$$\begin{aligned} \boldsymbol{I}_{\rm rb/p/b} &= \boldsymbol{I}_{\rm rb} + \boldsymbol{I}_{\rm p}(\xi) - m_{\rm p}\hat{\boldsymbol{r}}_{\rm p}\hat{\boldsymbol{r}}_{\rm p} \\ \boldsymbol{M}_{\rm rb/p/b} &= m_{\rm v}\mathbb{1} \\ \boldsymbol{C}_{\rm rb/p/b} &= m_{\rm rb}\hat{\boldsymbol{r}}_{\rm rb} + m_{\rm p}\hat{\boldsymbol{r}}_{\rm p}. \end{aligned}$$

The energy necessary to accelerate the fluid around the vehicle is

$$T_{\rm f} = \frac{1}{2}\boldsymbol{\eta}^T \mathbb{M}_{\rm f}\boldsymbol{\eta}. \tag{2.33}$$

where the added inertia matrix is in the following form:

$$\mathbb{M}_{\rm f} = \begin{pmatrix} \boldsymbol{I}_{\rm f} & \boldsymbol{C}_{\rm f} & \mathbb{O}_{3\times 6} \\ \boldsymbol{C}_{\rm f}^T & \boldsymbol{M}_{\rm f} & \mathbb{O}_{3\times 6} \\ \mathbb{O}_{6\times 3} & \mathbb{O}_{6\times 3} & \mathbb{O}_{6\times 6} \end{pmatrix}.$$

The total kinetic energy of the system is $T = T_{\rm rb/p/b} + T_{\rm f}$. The generalized inertia for the vehicle/fluid system is

$$\mathbb{M} = \mathbb{M}_{\rm rb/p/b} + \mathbb{M}_{\rm f}, \tag{2.34}$$

which is presented in Table 2.5. Then, the generalized momentum can be obtained from

$$\boldsymbol{\nu} = \frac{\partial T}{\partial \boldsymbol{\eta}} = \mathbb{M}\boldsymbol{\eta}. \tag{2.35}$$

Generalized Vehicle/Fluid Inertia $\mathbb{M}$

$$\begin{pmatrix} \boldsymbol{I}_{\mathrm{rb/p/b}} + \boldsymbol{I}_{\mathrm{f}} & \boldsymbol{C}_{\mathrm{rb/p/b}} + \boldsymbol{C}_{\mathrm{f}} & \boldsymbol{I}_{\mathrm{p}}(\xi) + m_{\mathrm{p}}\hat{\boldsymbol{r}}_{\mathrm{p}}\hat{\boldsymbol{r}}_{\mathrm{p}} & m_{\mathrm{p}}\hat{\boldsymbol{r}}_{\mathrm{p}} \\ \boldsymbol{C}^T_{\mathrm{rb/p/b}} + \boldsymbol{C}^T_{\mathrm{f}} & \boldsymbol{M}_{\mathrm{rb/p/b}} + \boldsymbol{M}_{\mathrm{f}} & m_{\mathrm{p}}\hat{\boldsymbol{r}}_{\mathrm{p}} & m_{\mathrm{p}}\mathbb{1} \\ \boldsymbol{I}_{\mathrm{p}}(\xi) + m_{\mathrm{p}}\hat{\boldsymbol{r}}_{\mathrm{p}}\hat{\boldsymbol{r}}_{\mathrm{p}} & -m_{\mathrm{p}}\hat{\boldsymbol{r}}_{\mathrm{p}} & \boldsymbol{I}_{\mathrm{p}}(\xi) - m_{\mathrm{p}}\hat{\boldsymbol{r}}_{\mathrm{p}}\hat{\boldsymbol{r}}_{\mathrm{p}} & -m_{\mathrm{p}}\hat{\boldsymbol{r}}_{\mathrm{p}} \\ -m_{\mathrm{p}}\hat{\boldsymbol{r}}_{\mathrm{p}} & m_{\mathrm{p}}\mathbb{1} & m_{\mathrm{p}}\hat{\boldsymbol{r}}_{\mathrm{p}} & m_{\mathrm{p}}\mathbb{1} \end{pmatrix}$$

Table 2.5 Generalized inertia matrix.

The dynamic equations are:

$$\begin{aligned} \dot{\boldsymbol{h}}_{\mathrm{sys}} &= \boldsymbol{h}_{\mathrm{sys}} \times \boldsymbol{\omega} + \boldsymbol{p}_{\mathrm{sys}} \times \boldsymbol{v} + (m_{\mathrm{rb}} g \boldsymbol{r}_{\mathrm{rb}} + m_{\mathrm{p}} g \boldsymbol{r}_{\mathrm{p}}) \times \boldsymbol{\zeta} + \boldsymbol{T}_{\mathrm{visc}} \\ \dot{\boldsymbol{p}}_{\mathrm{sys}} &= \boldsymbol{p}_{\mathrm{sys}} \times \boldsymbol{\omega} + \tilde{m} g \boldsymbol{\zeta} + \boldsymbol{F}_{\mathrm{visc}} \\ \dot{\boldsymbol{h}}_{\mathrm{p}} &= \boldsymbol{h}_{\mathrm{p}} \times \boldsymbol{\omega} + \boldsymbol{p}_{\mathrm{p}} \times \boldsymbol{v} + m_{\mathrm{p}} g \boldsymbol{r}_{\mathrm{p}} \times \boldsymbol{\zeta} + \tilde{\boldsymbol{T}}_{\mathrm{p}} \\ \dot{\boldsymbol{p}}_{\mathrm{p}} &= \boldsymbol{p}_{\mathrm{p}} \times \boldsymbol{\omega} + m_{\mathrm{p}} g \boldsymbol{\zeta} + \tilde{\boldsymbol{F}}_{\mathrm{p}} \\ \dot{m}_{\mathrm{b}} &= u_{\mathrm{b}}, \end{aligned} \tag{2.36}$$

where $\tilde{\boldsymbol{T}}_{\mathrm{p}}$ and $\tilde{\boldsymbol{F}}_{\mathrm{p}}$ represent moments and forces on moving mass which do not derive from scalar potential functions. These equations are written in mixed velocity/momentum notation and they can be converted to a set of dynamic equations in terms of a consistent set of variables in the following form,

$$\dot{\boldsymbol{\eta}} = \mathbb{M}^{-1}\dot{\boldsymbol{\nu}} - \mathbb{M}^{-1}\dot{\mathbb{M}} \;\; \mathbb{M}^{-1}\boldsymbol{\nu}, \tag{2.37}$$

where $\mathbb{M}^{-1}$ is the inverse of generalized inertia and $\dot{\mathbb{M}}$ is the time derivative of it. Note that since $\boldsymbol{I}_{\mathrm{p}}(\xi)$ depends on ξ, the computation of the rate of change of the generalized inertia will be slightly more complicated than was the case for a particle mass.

Chapter 3

Steady Motion

The steady-state flight conditions are determined by solving the nonlinear state equations (2.25–2.27) for the state and control vectors that make the state derivatives identically zero. Because of the complexity involved in computing an analytical solution, numerical algorithms for computing "trim conditions" are common [35]. Here we take an analytical approach to find (approximate) solutions for steady-state flight in terms of the model parameters presented in [32] and [31].

Analytical results, approximate or otherwise, are important for motion planning and also for vehicle design, as they may provide guidelines for sizing actuators and stabilizers. The conditions for steady turning flight of an underwater glider differ significantly from those for an aircraft. Deriving a closed-form expression is quite challenging. Instead, we begin by considering wings level equilibrium flight and consider turning motion as a perturbation. Given a desired equilibrium speed and glide path angle, one may determine the center of gravity location and the net weight required. The resulting longitudinal gliding equilibrium is the nominal solution to a regular perturbation problem in which the vehicle turn rate is the perturbation parameter.

3.1 Wings Level Gliding Flight

This section summarizes results presented in [21]. The conditions for wings level, gliding flight are that $\boldsymbol{\omega} = \mathbf{0}$, $\boldsymbol{v} \cdot \boldsymbol{e}_2 = 0$, and $\boldsymbol{\zeta} \cdot \boldsymbol{e}_2 = 0$. The second condition implies that $v = 0$ and therefore that $\beta = 0$. The third condition implies that $\phi = 0$. Also, we require that $r_{\mathrm{p}} = 0$ and that $\delta r = 0$. Inserting these conditions into equations (2.26) and (2.27) and solving for the remaining equilibrium conditions gives:

$$\mathbf{0} = \tilde{m} g \boldsymbol{\zeta}_0 + \begin{pmatrix} -\mathcal{D}(\alpha_0)\cos\alpha_0 + \mathcal{L}_\alpha \alpha_0 \sin\alpha_0 \\ 0 \\ -\mathcal{D}(\alpha_0)\sin\alpha_0 - \mathcal{L}_\alpha \alpha_0 \cos\alpha_0 \end{pmatrix} \tag{3.1}$$

$$\mathbf{0} = \boldsymbol{M}\boldsymbol{v}_0 \times \boldsymbol{v}_0 + (m_{\mathrm{rb}} g \boldsymbol{r}_{\mathrm{rb}}) \times \boldsymbol{\zeta}_0 + \begin{pmatrix} 0 \\ M_\alpha \alpha_0 \\ 0 \end{pmatrix}. \tag{3.2}$$

Following the analysis in [21], one may use equation (3.2) to show that

$$\boldsymbol{r}_{\mathrm{rb}} = \boldsymbol{r}^{\perp} + \varrho \boldsymbol{\zeta}_0, \tag{3.3}$$

where

$$\boldsymbol{r}^{\perp} = \frac{1}{m_{\mathrm{rb}} g} \left(\boldsymbol{M}\boldsymbol{v}_0 \times \boldsymbol{v}_0 + \begin{pmatrix} 0 \\ M_\alpha \alpha_0 \\ 0 \end{pmatrix} \right) \times \boldsymbol{\zeta}_0.$$

The free parameter ϱ is a measure of how bottom-heavy the vehicle is in a given, wings level flight condition. This parameter plays an important role in determining longitudinal stability of the gliding equilibrium. Note that $\boldsymbol{r} = \boldsymbol{r}^{\perp}$ is a particular solution to the linear algebraic system,

$$\hat{\boldsymbol{\zeta}}_0 \boldsymbol{r} = \frac{1}{m_{\mathrm{rb}} g} \left(\boldsymbol{M}\boldsymbol{v}_0 \times \boldsymbol{v}_0 + \begin{pmatrix} 0 \\ M_\alpha \alpha_0 \\ 0 \end{pmatrix} \right),$$

obtained from (3.2), for which $\boldsymbol{r}^{\perp} \cdot \boldsymbol{\zeta}_0 = 0$. The null space of $\hat{\boldsymbol{\zeta}}_0$ is described by $\varrho\boldsymbol{\zeta}_0$ where $\varrho \in \mathbb{R}$.

Next, one may solve (3.1) for $\boldsymbol{\zeta}_0$, $\boldsymbol{v}_0$, and $\tilde{m}_0$ given a desired speed V_0 and a desired glide path angle $\gamma_0 = \theta_0 - \alpha_0$. Expressed in the inertial frame, equation (3.1) gives

$$\begin{pmatrix} 0 \\ 0 \\ \tilde{m}g \end{pmatrix} = \begin{pmatrix} \sin(\gamma_0)\mathcal{L}_\alpha\alpha_0 + \cos(\gamma_0)\mathcal{D}(\alpha_0) \\ 0 \\ \cos(\gamma_0)\mathcal{L}_\alpha\alpha_0 - \sin(\gamma_0)\mathcal{D}(\alpha_0) \end{pmatrix}. \tag{3.4}$$

Equation (3.4) states that there is no net hydrodynamic force in the $\boldsymbol{i}_1$-direction and that net weight is balanced by the vertical components of the lift and drag forces.

The components of viscous force, in the current frame, are

$$\mathcal{D}(\alpha) = P_{\text{dyn}}SC_D(\alpha), \qquad \mathcal{S}(\beta) = P_{\text{dyn}}SC_S(\beta), \qquad \text{and} \qquad \mathcal{L}(\alpha) = P_{\text{dyn}}SC_L(\alpha)$$

where, following standard assumptions, the nondimensional coefficients take the form

$$C_D(\alpha) = C_{D_0} + KC_L(\alpha)^2, \qquad C_S(\beta) = C_{S_\beta}\beta, \qquad \text{and} \qquad C_L(\alpha) = C_{L_\alpha}\alpha.$$

The first component of equation (3.4) may be re-written as

$$\begin{aligned} \tan(\gamma_0) &= -\frac{C_D(\alpha_0)}{C_L(\alpha_0)} \\ &= -\left(\frac{C_{D_0} + KC_L(\alpha_0)^2}{C_L(\alpha_0)}\right), \end{aligned}$$

which implies that

$$KC_L^2 + \tan(\gamma_0)C_L + C_{D_0} = 0. \tag{3.5}$$

Note that a given glide path angle γ can be obtained, i.e., a real solution C_L to equation (3.5) exists, if and only if

$$\tan^2(\gamma_0) \geq 4KC_{D_0}.$$

Thus, for upward glides ($\gamma_0 > 0$), one requires that

$$\gamma_0 \geq \tan^{-1}\left(2\sqrt{KC_{D_0}}\right),$$

while for downward glides, one must choose

$$\gamma_0 \leq -\tan^{-1}\left(2\sqrt{KC_{D_0}}\right).$$

Clearly, the smaller the product KC_{D_0}, the larger the range of achievable glide path angles. Given values of K and C_{D_0}, the best possible glide path angle is

$$\gamma_0 = (\pm)\tan^{-1}\left(2\sqrt{KC_{D_0}}\right),$$

This glide path maximizes range (in still water) and corresponds to minimum drag flight:

$$C_L(\alpha_0) = \mp\sqrt{\frac{C_{D_0}}{K}} \qquad \Rightarrow \qquad \alpha_0 = \mp\frac{1}{C_{L_\alpha}}\sqrt{\frac{C_{D_0}}{K}}.$$

These conditions provide an upper bound on achievable performance, but operational considerations may dictate a steeper glide path angle.

Having obtained values for $C_D(\alpha_0)$ and $C_L(\alpha_0)$ (and for α_0 and γ_0, and therefore θ_0), one may solve the third component of equation (3.4) for the required net weight $\tilde{m}_0 g$ for a given glide speed V_0:

$$\tilde{m}_0 g = \left(\frac{1}{2}\rho V_0^2 S\right)\left(\cos(\gamma_0)C_{L_\alpha}\alpha_0 - \sin(\gamma_0)\left(C_{D_0} + K\left(C_{L_\alpha}\alpha_0\right)^2\right)\right). \tag{3.6}$$

Thus, one may independently assign the glider's equilibrium attitude, by moving the center of mass according to (3.3), and its speed, by changing the net weight $\tilde{m}_0 g$ according to (3.6). For the minimum drag flight condition, for example,

$$\tilde{m}_0 g = \left(\frac{1}{2}\rho V_0^2 S\right)\left(\mp\sqrt{\frac{C_{D_0}}{K}}\cos(\gamma_0) - 2C_{D_0}\sin(\gamma_0)\right).$$

3.2 Steady Turning Flight

For turning flight, the condition on $\boldsymbol{\omega}$ becomes $\boldsymbol{\omega} \parallel \boldsymbol{\zeta}$. One may therefore write

$$\boldsymbol{\omega} = \omega\boldsymbol{\zeta},$$

where $\omega \in \mathbb{R}$ is the turn rate. A steady turn is an asymmetric flight condition, so we no longer assume that v and ϕ are zero. Moreover, to effect and maintain such an asymmetric flight condition requires that r_{p} or δr or both be nonzero.

3.2.1 Turning Flight for Aircraft

Before discussing turning flight for an underwater glider, we first review the conditions for turning flight of aircraft in the notation that we have developed for underwater gliders. Key differences include the hydrodynamic forces (which, for AUVs, include a significant contribution from added mass and inertia) and the force of buoyancy. Since there is no appreciable buoyant force for aircraft, the body frame origin is typically chosen as the center of mass. In this case, the momenta $\boldsymbol{p}$ and $\boldsymbol{h}$ are related to the velocities $\boldsymbol{v}$ and $\boldsymbol{\omega}$ as follows:

$$\begin{pmatrix} \boldsymbol{p} \\ \boldsymbol{h} \end{pmatrix} = \begin{pmatrix} m_{\mathrm{rb}}\mathbb{1} & \mathbf{0} \\ \mathbf{0} & \boldsymbol{I} \end{pmatrix} \begin{pmatrix} \boldsymbol{v} \\ \omega\boldsymbol{\zeta} \end{pmatrix}. \tag{3.7}$$

Another important difference between aircraft and underwater gliders is the type of actuation. Aircraft use control surfaces, such as ailerons, a rudder, and an elevator to produce control moments, while underwater gliders use the gravitational moment, which can be adjusted by moving an internal mass.

For an aircraft in a steady turn, equations (2.25) through (2.27) simplify to the following:

$$\dot{\boldsymbol{\zeta}} = \mathbf{0} \tag{3.8}$$

$$\dot{\boldsymbol{p}} = \mathbf{0} = \boldsymbol{p} \times \omega\boldsymbol{\zeta} + m_{\mathrm{rb}} g\boldsymbol{\zeta} + \boldsymbol{F}_{\mathrm{visc}} \tag{3.9}$$

$$\dot{\boldsymbol{h}} = \mathbf{0} = \boldsymbol{h} \times \omega\boldsymbol{\zeta} + \boldsymbol{T}_{\mathrm{visc}} \tag{3.10}$$

Note that the first equation implies that $\boldsymbol{\zeta}$ is constant, which means that ϕ and θ are constant. Also note, in the second equation, that the term $\boldsymbol{p} \times \boldsymbol{v}$ has vanished because linear velocity and momentum are parallel for an aircraft.

The viscous forces and moments will be different from those for an underwater glider, of course, and they will include terms due to the control surfaces. Thus, terms such as roll moment due to aileron ($L_{\delta a}\delta a$) and coupling between the aileron and rudder ($N_{\delta a}\delta a$ and $L_{\delta r}\delta r$) must be included. Also, angular rate effects on the aerodynamic force and moment are included, with standard assumptions concerning vehicle symmetry.

Let T represent thrust, which is assumed to be aligned with the longitudinal axis. Then

$$\boldsymbol{F}_{\text{visc}} = \begin{pmatrix} X \\ Y \\ Z \end{pmatrix} = -\boldsymbol{\mathcal{R}}_{\text{BC}}(\alpha,\beta) \begin{pmatrix} \mathcal{D}(\alpha,\beta,\delta a,\delta e,\delta r) \\ \mathcal{S}_\beta \beta + \mathcal{S}_{\delta r}\delta r \\ \mathcal{L}_\alpha \alpha + \mathcal{L}_{\delta e}\delta e \end{pmatrix} + \begin{pmatrix} T + X_q q \\ Y_p p + Y_r r \\ Z_q q \end{pmatrix}.$$

For small sideslip angles,

$$Y = Y_\beta \beta + Y_{\delta r}\delta r + Y_p p + Y_r r.$$

The viscous moment takes the form:

$$\boldsymbol{T}_{\text{visc}} = \begin{pmatrix} L_\beta \beta + L_{\delta_a}\delta a + L_{\delta_r}\delta r + L_p p + L_r r \\ M_\alpha \alpha + M_{\delta_e}\delta e + M_q q \\ N_\beta \beta + N_{\delta_a}\delta a + N_{\delta_r}\delta r + N_p p + N_r r \end{pmatrix}.$$

For steady turning flight, the components of $\boldsymbol{v}$ and $\boldsymbol{\omega}$ are small, with the exception of $u \approx V$. Neglecting products of small terms, one finds that

$$\boldsymbol{p} \times \omega\boldsymbol{\zeta} \approx m_{\text{rb}} V \omega \begin{pmatrix} 0 \\ -\cos\phi\cos\theta \\ \sin\phi\cos\theta \end{pmatrix}_{\text{eq}} \quad \text{and} \quad \boldsymbol{h}_{\text{eq}} \times \omega\boldsymbol{\zeta}_{\text{eq}} \approx \boldsymbol{0}.$$

Substituting into (3.9) and (3.10), the conditions for steady turning motion of an aircraft are

$$\boldsymbol{0} = m_{\text{rb}} V \omega \begin{pmatrix} 0 \\ -\cos\phi\cos\theta_0 \\ \sin\phi\cos\theta_0 \end{pmatrix} + m_{\text{rb}} g \begin{pmatrix} -\sin\theta \\ \sin\phi\cos\theta \\ \cos\phi\cos\theta \end{pmatrix} + \boldsymbol{F}_{\text{visc}} \tag{3.11}$$

$$\boldsymbol{0} = \boldsymbol{T}_{\text{visc}}. \tag{3.12}$$

The key condition for steady turning flight is that the lateral aerodynamic force Y be identically zero [36]. From the second component of equation (3.11), one therefore requires that

$$0 = m_{\text{rb}} V \omega(-\cos\phi\cos\theta) + m_{\text{rb}} g(\sin\phi\cos\theta),$$

from which the roll angle ϕ can be obtained in terms of turn rate ω:

$$\tan\phi = \frac{V}{g}\omega. \tag{3.13}$$

The pitch angle θ, angle of attack α, and pitch rate q may be determined from the longitudinal components of (3.11) and (3.12), as parameterized by the elevator angle δe and thrust T. The remaining conditions for steady turning flight are then obtained from the remaining linear algebraic system:

$$\begin{pmatrix} Y_\beta & Y_{\delta r} & 0 \\ L_\beta & L_{\delta r} & L_{\delta a} \\ N_\beta & N_{\delta r} & N_{\delta a} \end{pmatrix} \begin{pmatrix} \beta \\ \delta r \\ \delta a \end{pmatrix} = \begin{pmatrix} Y_p & Y_r \\ L_p & L_r \\ N_p & N_r \end{pmatrix} \begin{pmatrix} \omega\sin\theta \\ -\omega\cos\theta\cos\phi \end{pmatrix}. \tag{3.14}$$

These equations give the sideslip angle and aileron and rudder deflections necessary for an aircraft to maintain a banked turn at a given speed V, turn rate ω, and pitch angle θ.

3.2.2 Turning Flight for Underwater Gliders

The situation for an underwater glider is considerably different. The center of mass is no longer the origin of the body reference frame and angular and linear momentum are coupled through inertial asymmetries. Linear momentum is no longer parallel to linear velocity, because added mass is directional and because of coupling between linear and angular velocity introduced by the offset center of mass. Propulsion is provided not by a thruster but by the net weight of the vehicle (weight minus buoyant force). In fact, the problem of finding analytical steady turning solutions for underwater gliders is quite challenging. We instead formulate the problem as a regular perturbation problem in the turn rate and seek a first-order approximate solution. To argue that the higher order solutions are "small corrections" requires some well-founded notion of "small," so we begin by nondimensionalizing the dynamic equations.

We choose the reference parameters

$$\text{length: } l, \qquad \text{mass: } m_{\text{rb}}, \qquad \text{and} \qquad \text{time: } T = \frac{l}{V_0},$$

where l is a characteristic length scale for the vehicle (such as length overall) and V_0 is the nominal speed. With these definitions, the nondimensional momenta $\bar{\boldsymbol{p}}$ and $\bar{\boldsymbol{h}}$ are related to the nondimensional velocities $\bar{\boldsymbol{v}}$ and $\bar{\boldsymbol{\omega}}$ through the nondimensional generalized inertia matrix as follows:

$$\begin{pmatrix} \bar{\boldsymbol{p}} \\ \bar{\boldsymbol{h}} \end{pmatrix} = \begin{pmatrix} \bar{\boldsymbol{M}} & \bar{\boldsymbol{C}}^T \\ \bar{\boldsymbol{C}} & \bar{\boldsymbol{I}} \end{pmatrix} \begin{pmatrix} \bar{\boldsymbol{v}} \\ \bar{\boldsymbol{\omega}} \end{pmatrix}$$

where

$$\bar{\boldsymbol{v}} = \frac{1}{V_0}\boldsymbol{v} \quad \text{and} \quad \bar{\boldsymbol{\omega}} = \boldsymbol{\omega}T$$

and where

$$\bar{\boldsymbol{M}} = \frac{1}{m_{\rm rb}}\boldsymbol{M}, \quad \bar{\boldsymbol{I}} = \frac{1}{m_{\rm rb}l^2}\boldsymbol{I}, \quad \text{and} \quad \bar{\boldsymbol{C}} = \frac{1}{m_{\rm rb}l}\boldsymbol{C}.$$

The nondimensional dynamic equations are

$$\dot{\bar{\boldsymbol{\zeta}}} = \bar{\boldsymbol{\zeta}} \times \bar{\boldsymbol{\omega}} \tag{3.15}$$

$$\dot{\bar{\boldsymbol{p}}} = \bar{\boldsymbol{p}} \times \bar{\boldsymbol{\omega}} + \bar{\tilde{m}}\bar{\boldsymbol{\zeta}} + \bar{\boldsymbol{F}}_{\rm visc} \tag{3.16}$$

$$\dot{\bar{\boldsymbol{h}}} = \bar{\boldsymbol{h}} \times \bar{\boldsymbol{\omega}} + \bar{\boldsymbol{p}} \times \bar{\boldsymbol{v}} + (\bar{m}_{\rm p}\bar{\boldsymbol{r}}_{\rm p} + \bar{\boldsymbol{r}}_{\rm rb}) \times \bar{\boldsymbol{\zeta}} + \bar{\boldsymbol{T}}_{\rm visc}, \tag{3.17}$$

where the overdot represents differentiation with respect to nondimensional time T and where

$$\bar{\boldsymbol{\zeta}} = \frac{\boldsymbol{\zeta}}{V_0^2/(gl)}, \quad \bar{\tilde{m}} = \frac{\tilde{m}}{m_{\rm rb}}, \quad \bar{m}_{\rm p} = \frac{m_{\rm p}}{m_{\rm rb}}, \quad \bar{\boldsymbol{r}}_{\rm rb} = \frac{\boldsymbol{r}_{\rm rb}}{l}, \quad \text{and} \quad \bar{\boldsymbol{r}}_{\rm p} = \frac{\bar{\boldsymbol{r}}}{l}$$

and

$$\bar{\boldsymbol{F}}_{\rm visc} = \frac{\boldsymbol{F}_{\rm visc}}{m_{\rm rb}V_0^2/l} \quad \text{and} \quad \bar{\boldsymbol{M}}_{\rm viscous} = \frac{\boldsymbol{T}_{\rm visc}}{m_{\rm rb}V_0^2}.$$

To express the viscous forces and moments explicitly, we also define

$$\bar{V} = \frac{V}{V_0}, \quad \bar{\rho} = \frac{\rho}{m_{\rm rb}/l^3}, \quad \text{and} \quad \bar{S} = \frac{S}{l^2}.$$

To simplify the analysis, we assume that

$$\bar{\boldsymbol{D}}_\omega = \frac{1}{2}\bar{\rho}\bar{V}^2\bar{S}\ \text{diag}\left(C_{l_p},\ C_{m_q},\ C_{n_r}\right)$$

where C_{l_p}, C_{m_q}, and C_{n_r} are nondimensional stability derivatives representing rotational damping. The assumption that roll and yaw damping are decoupled is reasonable for a vehicle with two planes of external geometric symmetry.

Recall that $\bar{\boldsymbol{\omega}} = \bar{\omega}\boldsymbol{\zeta}$ for a steady turn. Define a characteristic frequency $\omega_n = \sqrt{g/l}$ and let $\bar{\omega}_n = \omega_n T$ denote its nondimensional value. Let $\bar{\omega} = \epsilon\bar{\omega}_n$ where ϵ is a small, nondimensional parameter. One may treat the problem of solving for steady turning flight conditions as an algebraic regular perturbation problem in ϵ. When $\epsilon = 0$, the vehicle is in wings-level equilibrium flight. If $\epsilon \neq 0$, then either r_{p} or δr or both must be nonzero. (Recall that $\boldsymbol{r}_{\mathrm{rb}}$ remains fixed at its nominal value, which corresponds to the nominal wings-level flight condition when r_{p} and δr are zero.)

Having nondimensionalized the terms appearing in the dynamic equations, we simplify notation by omitting the overbar; in the sequel, all quantities are nondimensional unless otherwise stated. The nondimensional equilibrium equations are

$$\begin{aligned}
\mathbf{0} &= \boldsymbol{p}_{\mathrm{eq}} \times \omega\boldsymbol{\zeta}_{\mathrm{eq}} + \tilde{m}_{\mathrm{eq}}\boldsymbol{\zeta}_{\mathrm{eq}} - \left(\frac{1}{2}\rho V_{\mathrm{eq}}^2 S\right)\boldsymbol{\mathcal{R}}_{\mathrm{BC}}(\alpha_{\mathrm{eq}}, \beta_{\mathrm{eq}}) \begin{pmatrix} C_D(\alpha) \\ C_{S_\beta}\beta \\ C_{L_\alpha}\alpha \end{pmatrix}_{\mathrm{eq}} \\
\mathbf{0} &= \boldsymbol{h}_{\mathrm{eq}} \times \omega\boldsymbol{\zeta}_{\mathrm{eq}} + \boldsymbol{p}_{\mathrm{eq}} \times \boldsymbol{v}_{\mathrm{eq}} + (m_{\mathrm{p}}\boldsymbol{r}_{\mathrm{p}} + \boldsymbol{r}_{\mathrm{rb}}) \times \boldsymbol{\zeta}_{\mathrm{eq}} + \left(\frac{1}{2}\rho V_{\mathrm{eq}}^2 S\right) \begin{pmatrix} C_{l_\beta}\beta \\ C_{m_\alpha}\alpha \\ C_{n_\beta}\beta + C_{n_{\delta r}}\delta r \end{pmatrix}_{\mathrm{eq}} \\
&\quad + \boldsymbol{D}_\omega \omega\boldsymbol{\zeta}_{\mathrm{eq}}
\end{aligned}$$

where C_{l_β}, C_{m_α}, C_{n_β}, and $C_{n_{\delta r}}$ are nondimensional stability derivatives. Note that

$$\begin{pmatrix} \boldsymbol{p}_{\mathrm{eq}} \\ \boldsymbol{h}_{\mathrm{eq}} \end{pmatrix} = \begin{pmatrix} \boldsymbol{M} & \boldsymbol{C}^T \\ \boldsymbol{C} & \boldsymbol{I} \end{pmatrix} \begin{pmatrix} \boldsymbol{v}_{\mathrm{eq}} \\ (\omega\boldsymbol{\zeta}_{\mathrm{eq}}) \end{pmatrix}$$

where

$$\boldsymbol{v}_{\mathrm{eq}} = \boldsymbol{\mathcal{R}}_{\mathrm{BC}}(\alpha_{\mathrm{eq}}, \beta_{\mathrm{eq}})(V_{\mathrm{eq}}\boldsymbol{e}_1).$$

As we have stated, $\boldsymbol{\zeta}$ remains constant in turning flight; equivalently, ϕ and θ remain constant. We seek equilibrium solutions for which the perturbed value of $\boldsymbol{\zeta}$ takes the following form:

$$\begin{aligned}\boldsymbol{\zeta}_{\mathrm{eq}} &= e^{-\phi_{\mathrm{eq}}\widehat{\boldsymbol{e}_1}}\boldsymbol{\zeta}_0 \\ &= \begin{pmatrix} 1 & 0 & 0 \\ 0 & \cos\phi_{\mathrm{eq}} & \sin\phi_{\mathrm{eq}} \\ 0 & -\sin\phi_{\mathrm{eq}} & \cos\phi_{\mathrm{eq}} \end{pmatrix} \boldsymbol{\zeta}_0.\end{aligned}$$

By construction, the perturbed equilibrium turning motion will have the same pitch angle θ as the corresponding, unperturbed wings level flight condition.

Using the definitions and observations above, the equilibrium equations may be written more explicitly:

$$\begin{aligned}\mathbf{0} &= \left(\boldsymbol{M}\left(\boldsymbol{\mathcal{R}}_{\mathrm{BC}}(\alpha_{\mathrm{eq}},\beta_{\mathrm{eq}})(V_{\mathrm{eq}}\boldsymbol{e}_1)\right) + \boldsymbol{C}^T\left(\epsilon\omega_n e^{-\phi_{\mathrm{eq}}\widehat{\boldsymbol{e}_1}}\boldsymbol{\zeta}_0\right)\right) \times \left(\epsilon\omega_n e^{-\phi_{\mathrm{eq}}\widehat{\boldsymbol{e}_1}}\boldsymbol{\zeta}_0\right) \\ &\quad + \tilde{m}_{\mathrm{eq}} e^{-\phi_{\mathrm{eq}}\widehat{\boldsymbol{e}_1}}\boldsymbol{\zeta}_0 - \left(\frac{1}{2}\rho V_{\mathrm{eq}}^2 S\right)\boldsymbol{\mathcal{R}}_{\mathrm{BC}}(\alpha_{\mathrm{eq}},\beta_{\mathrm{eq}}) \begin{pmatrix} C_D(\alpha) \\ C_{S_\beta}\beta \\ C_{L_\alpha}\alpha \end{pmatrix}_{\mathrm{eq}} \qquad (3.18)\end{aligned}$$

$$\begin{aligned}\mathbf{0} &= \left(\boldsymbol{I}\left(\epsilon\omega_n e^{-\phi_{\mathrm{eq}}\widehat{\boldsymbol{e}_1}}\boldsymbol{\zeta}_0\right) + \boldsymbol{C}\left(\boldsymbol{\mathcal{R}}_{\mathrm{BC}}(\alpha_{\mathrm{eq}},\beta_{\mathrm{eq}})(V_{\mathrm{eq}}\boldsymbol{e}_1)\right)\right) \times \left(\epsilon\omega_n e^{-\phi_{\mathrm{eq}}\widehat{\boldsymbol{e}_1}}\boldsymbol{\zeta}_0\right) \\ &\quad + \left(\boldsymbol{M}\left(\boldsymbol{\mathcal{R}}_{\mathrm{BC}}(\alpha_{\mathrm{eq}},\beta_{\mathrm{eq}})(V_{\mathrm{eq}}\boldsymbol{e}_1)\right) + \boldsymbol{C}^T\left(\epsilon\omega_n e^{-\phi_{\mathrm{eq}}\widehat{\boldsymbol{e}_1}}\boldsymbol{\zeta}_0\right)\right) \times \left(\boldsymbol{\mathcal{R}}_{\mathrm{BC}}(\alpha_{\mathrm{eq}},\beta_{\mathrm{eq}})(V_{\mathrm{eq}}\boldsymbol{e}_1)\right) \\ &\quad + (m_{\mathrm{p}}\boldsymbol{r}_{\mathrm{p}} + \boldsymbol{r}_{\mathrm{rb}}) \times \left(e^{-\phi_{\mathrm{eq}}\widehat{\boldsymbol{e}_1}}\boldsymbol{\zeta}_0\right) + \boldsymbol{D}_\omega\left(\epsilon\omega_n e^{-\phi_{\mathrm{eq}}\widehat{\boldsymbol{e}_1}}\boldsymbol{\zeta}_0\right) \\ &\quad + \left(\frac{1}{2}\rho V_{\mathrm{eq}}^2 S\right) \begin{pmatrix} C_{l_\beta}\beta \\ C_{m_\alpha}\alpha \\ C_{n_\beta}\beta + C_{n_{\delta r}}\delta r \end{pmatrix}_{\mathrm{eq}}. \qquad (3.19)\end{aligned}$$

To obtain the regular perturbation solution in ϵ, first substitute the following polynomial expansions for r_{p}, $\tilde{m}$, ϕ, V, α, and β:

$$V = \sum_n V_n \epsilon^n = V_0 + \epsilon V_1 + \epsilon^2 V_2 + \cdots \qquad \tilde{m} = \sum_n \tilde{m}_n \epsilon^n = \tilde{m}_0 + \epsilon \tilde{m}_1 + \epsilon^2 \tilde{m}_2 + \cdots$$

$$\alpha = \sum_n \alpha_n \epsilon^n = \alpha_0 + \epsilon \alpha_1 + \epsilon^2 \alpha_2 + \cdots \qquad \phi = \sum_n \phi_n \epsilon^n = \epsilon \phi_1 + \epsilon^2 \phi_2 + \cdots$$

$$\beta = \sum_n \beta_n \epsilon^n = \epsilon \beta_1 + \epsilon^2 \beta_2 + \cdots \qquad r_{\mathrm{p}} = \sum_n r_{\mathrm{p}_n} \epsilon^n = \epsilon r_{\mathrm{p}_1} + \epsilon^2 r_{\mathrm{p}_2} + \cdots$$

(We have suppressed the subscript "eq" for convenience.) Also, let $\delta r = 0 + \epsilon \delta r_1$. (The rudder deflection δr_1 will appear as a free parameter in the solution to the regular perturbation problem.) Substituting these polynomial expansions into equations (3.18) and (3.19) and collecting powers of ϵ gives a regular perturbation series in ϵ. Solving the coefficient equation for ϵ^0 gives the nominal, wings level flight conditions. Solving the coefficient equation for ϵ^1 gives approximate values for r_{p}, $\tilde{m}$, ϕ, V, α, and β to first order in ϵ. Let

$$\begin{aligned} \Delta \;=\; & (\rho S)^2 \left(r_{b_x} \mathrm{c}\theta_0 + r_{b_z} \mathrm{s}\theta_0\right) \left(C_D(\alpha_0) + C_{S_\beta}\right) + \tilde{m}_0 \left(\rho S\right) \left(C_{n_\beta} \mathrm{c}\theta_0 - C_{l_\beta} \mathrm{s}\theta_0\right) \\ & + 2\tilde{m}_0 \left[\left(-X_{\dot{u}} + Y_{\dot{v}}\right) \mathrm{c}\alpha_0 \mathrm{c}\theta_0 + \left(-Z_{\dot{w}} + Y_{\dot{v}}\right) \mathrm{s}\alpha_0 \mathrm{s}\theta_0\right], \end{aligned} \tag{3.20}$$

where "s" represents the sine function and "c" represents cosine. The first-order solution to the regular perturbation problem defined by equations (3.18) and (3.19) is:

$$V_1 = 0 \tag{3.21}$$

$$\alpha_1 = 0 \tag{3.22}$$

$$\tilde{m}_1 = 0 \tag{3.23}$$

$$\begin{aligned} \beta_1 = -\frac{\omega_n}{\Delta} \{ & 2 \left(r_{b_x} \mathrm{c}\theta_0 + r_{b_z} \mathrm{s}\theta_0\right) \left[\left(m - X_{\dot{u}}\right) \mathrm{c}\alpha_0 \mathrm{c}\theta_0 + \left(m - Z_{\dot{w}}\right) \mathrm{s}\alpha_0 \mathrm{s}\theta_0\right] + 2\tilde{m}_0 \mathrm{c}\theta_0 \mathrm{c}(\theta_0 - \alpha_0) N_{\dot{v}} \\ & + \tilde{m}_0 \left(\rho S\right) \left(C_{l_p} \mathrm{s}^2\theta_0 + C_{n_r} \mathrm{c}^2\theta_0\right) \} - \frac{\rho S}{\Delta} \left[\tilde{m}_0 \mathrm{c}\theta_0 C_{n_{\delta r}} \delta r_1 + \left(r_{b_x} \mathrm{c}\theta_0 + r_{b_z} \mathrm{s}\theta_0\right) C_{S_{\delta r}} \delta r_1\right] \end{aligned} \tag{3.24}$$

$$\begin{aligned} \phi_1 = & \frac{\omega_n}{4\tilde{m}_0 \mathrm{c}\theta_0 \Delta} \left[\left(m + \tilde{m}_0 - X_{\dot{u}}\right) \mathrm{c}\alpha_0 \mathrm{c}\theta_0 + \left(m + \tilde{m}_0 - Z_{\dot{w}}\right) \mathrm{s}\alpha_0 \mathrm{s}\theta_0\right] \\ & + \frac{\rho S}{8\tilde{m}_0 \mathrm{c}\theta_0} \left[\left(C_D(\alpha_0) + C_{S_\beta}\right) \beta_1 + \frac{1}{\Delta} C_{S_{\delta r}} \delta r_1\right] \end{aligned} \tag{3.25}$$

$$
\begin{aligned}
r_{\mathrm{p}_1} = \frac{1}{2m_{\mathrm{p}}\Delta} \Big\{ & 2\omega_n (\rho S) \left(r_{b_x} C_{l_\beta} + r_{b_z} C_{n_\beta}\right) \left[(m - X_{\dot{u}})\, \mathrm{c}\alpha_0 \mathrm{c}\theta_0 + (m - Z_{\dot{w}})\, \mathrm{s}\alpha_0 \mathrm{s}\theta_0\right] \\
& + 2\tilde{m}_0 \omega_n (\rho S) \left[C_{l_p} (-X_{\dot{u}} + Y_{\dot{v}})\, \mathrm{c}\alpha_0 \mathrm{s}\theta_0 - C_{n_r} (-Z_{\dot{w}} + Y_{\dot{v}})\, \mathrm{s}\alpha_0 \mathrm{c}\theta_0\right] \\
& + 2\omega_n \mathrm{s}2\alpha_0 (-Z_{\dot{w}} + Y_{\dot{v}}) \left[r_{b_x} (m - X_{\dot{u}})\, \mathrm{c}\theta_0 + r_{b_z} (m - Z_{\dot{w}})\, \mathrm{s}\theta_0\right] \\
& - 2\omega_n (1 - \mathrm{c}2\alpha_0) \left[r_{b_x} (m - Z_{\dot{w}}) (-Z_{\dot{w}} + Y_{\dot{v}})\, \mathrm{s}\theta_0 - r_{b_z} (m - X_{\dot{u}}) (-X_{\dot{u}} + Y_{\dot{v}})\, \mathrm{c}\theta_0\right] \\
& - 4\tilde{m}_0 \omega_n \mathrm{s}\alpha_0 \left\{\left[M_{\dot{w}} (-X_{\dot{u}} + Y_{\dot{v}}) + N_{\dot{v}} (-X_{\dot{u}} + Z_{\dot{w}})\right] \mathrm{c}\alpha_0 \mathrm{s}\theta_0 - M_{\dot{w}} (-Z_{\dot{w}} + Y_{\dot{v}})\, \mathrm{s}\alpha_0 \mathrm{s}\theta_0\right\} \\
& + \omega_n (\rho S) \Big\{ \left[\tilde{m}_0 C_{l_\beta} - r_{b_z} \left(C_D(\alpha_0) + C_{S_\beta}\right)\right] \left[(\rho S)\, C_{n_r} \mathrm{c}\theta_0 + 2 \left(N_{\dot{v}} \mathrm{c}\alpha_0 \mathrm{c}\theta_0 - M_{\dot{w}} \mathrm{s}\alpha_0 \mathrm{s}\theta_0\right)\right] \\
& + \left[\tilde{m}_0 C_{n_\beta} + r_{b_x} \left(C_D(\alpha_0) + C_{S_\beta}\right)\right] \left[(\rho S)\, C_{l_p} \mathrm{s}\theta_0 + 2 \left(M_{\dot{w}} + N_{\dot{v}}\right) \mathrm{s}\alpha_0 \mathrm{c}\theta_0\right] \Big\} \\
& + (\rho S)\, C_{n_{\delta r}} \delta r_1 \left\{(\rho S) \left[\tilde{m}_0 C_{l_\beta} - r_{b_z} \left(C_D(\alpha_0) + C_{S_\beta}\right)\right] - 2\tilde{m}_0 (-Z_{\dot{w}} + Y_{\dot{v}})\, \mathrm{s}\alpha_0\right\} \\
& + (\rho S)\, C_{S_{\delta r}} \delta r_1 \left\{(\rho S) \left(r_{b_x} C_{l_\beta} + r_{b_z} C_{n_\beta}\right) + 2 \left[r_{b_x} (-Z_{\dot{w}} + Y_{\dot{v}})\, \mathrm{s}\alpha_0 + r_{b_z} (-X_{\dot{u}} + Y_{\dot{v}})\, \mathrm{c}\alpha_0\right]\right\} \Big\}
\end{aligned}
\tag{3.26}
$$

The explicit analytical expressions given above, particularly in equations (3.24–3.26), provide insight concerning the role of design parameters such as wing sweep angle, vertical stabilizer size, moving mass actuator size, and rudder size in determining a vehicle's turning capability. They also exhibit an interesting structure, which is discussed in Remark 3.2.1 below.

Remark 3.2.1 *That V, α, and $\tilde{m}$ remain constant to first order in ϵ suggests that the primary contributors to steady turning motion are lateral mass deflections (r_{p}) and rudder deflections (δr_1) and that these deflections have no first-order effect on speed or angle of attack. In practice, it is considerably more costly to change the vehicle's net mass $\tilde{m}$ than to shift its center of gravity. As shown in equation (3.6), $\tilde{m}$ directly controls speed, so to maximize glider speed in descent (ascent) one must drive $\tilde{m}$ to its maximum (minimum) value. Thus, at least in maximum speed operations, the problem of controlling longitudinal motion (speed and glide path angle) decouples from the problem of controlling directional motion (turn rate) to first order in ϵ. As it will be discussed in Section 6.1, this observation suggests a natural approach to motion control and path planning for underwater gliders.*

Remark 3.2.2 *Note that the rudder deflection δr_1 appears as a free parameter in expressions (3.21–3.26). For a rudderless vehicle, one simply sets $\delta r_1 = 0$. Including a rudder, however, provides additional freedom to control the lateral-directional dynamics. For example, using (3.24), one could adjust the rudder angle so as to zero the sideslip angle, to first order in ϵ, thereby reducing the total drag. (Equation (3.24) gives guidance for sizing a rudder for this purpose.) Drag reduction is especially critical for underwater gliders, whose primary operational advantage is efficiency. On the other hand, a rudder is an external actuator which is subject to damage or fouling and which introduces an additional failure mode into the system.*

Equations (3.21–3.26) provide a first-order approximation for steady turning motions. To assess stability of the true, neighboring turning motion, one may linearize about the *approximate* equilibrium condition and compute the eigenvalues. Recognizing that the eigenvalues of the resulting time-invariant state matrix depend continuously on its parameters, stability properties of the true equilibrium may be inferred from stability properties of the approximate equilibrium provided that (i) the equilibrium is hyperbolic and (ii) ϵ is small relative to the real part of every eigenvalue. See Section 1.7 of [37] for a brief discussion or Chapter 9 of [38] for more details.

3.3 Numerical Case Study: *Slocum*

To verify our steady turn predictions for a realistic vehicle model, we have applied the results to the model for *Slocum*, shown in Figure 3.1, for which hydrodynamic model parameters are given in [26]. We consider perturbations from a wings-level equilibrium flight condition at speed $V_0 = 1.5$ knots and angle of attack $\alpha_0 = 4.3°$, the angle which corresponds to the maximum lift-to-drag ratio. We assume that $\delta r_1 = 0$, noting that neither *Liberdade/XRay* nor the deep-water ("thermal") version of *Slocum* uses a rudder.

Figure 3.2 shows the wings-level equilibrium glide characteristics for the *Slocum* glider.

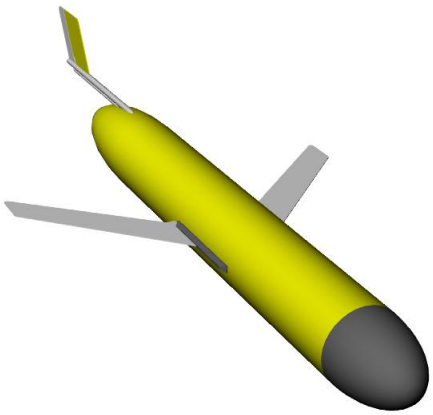

Figure 3.1 The underwater glider *Slocum*. (Solid model in Rhinoceros 3.0.)

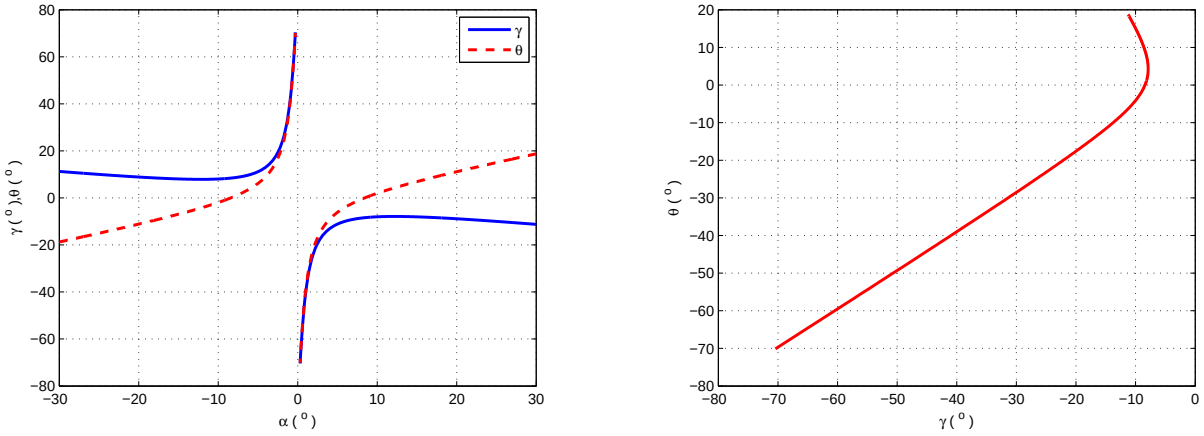

Figure 3.2 Wings level equilibrium glide characteristics for *Slocum* model.

The lift, sideforce and drag parameters are:

$$C_{L_\alpha} = 2.04 \text{ rad}^{-1}, \qquad C_{S_\beta} = 0.30 \text{ rad}^{-1}, \qquad C_{D_0} = 0.03, \qquad \text{and} \qquad K = 0.16.$$

Other important parameters include $l = 1.5$ m and $m_{\text{rb}} = 40$ kg. The rigid body inertia matrix is

$$I_{\text{rb}} = \begin{pmatrix} 0.25 & 0 & 0 \\ 0 & 9.72 & 0 \\ 0 & 0 & 9.72 \end{pmatrix}.$$

The values of the nonzero terms in the generalized added mass matrix are given below.

$$-X_{\dot{u}} = 5 \text{ kg} \qquad -L_{\dot{p}} = 3.75 \text{ kg-m}^2$$

$$-Y_{\dot{v}} = 60 \text{ kg} \qquad -M_{\dot{q}} = 2.28 \text{ kg-m}^2$$

$$-Z_{\dot{w}} = 70 \text{ kg} \qquad -N_{\dot{r}} = 1.28 \text{ kg-m}^2$$

The values of the viscous stability derivatives are given below.

C_m		C_l		C_n	
α	-0.75	β	-0.90	β	1.51
$\bar{q}$	-0.90	$\bar{p}$	-0.30	$\bar{r}$	-0.30

Once one has computed the conditions for equilibrium flight, one may examine stability. The simplest approach is spectral analysis. Using the *Slocum* model described in [26], we linearize about the wings-level, equilibrium flight condition corresponding to the following parameter values:

$$V_0 = 0.758 \text{ m/s}, \qquad \alpha_0 = 4.3^\circ, \qquad \theta_0 = -8.2^\circ, \qquad \gamma_0 = -12.5^\circ \qquad \text{and} \qquad \tilde{m}_0 = 0.61 \text{ kg}.$$

As mentioned in Section 3.1, the free parameter ϱ provides a measure of how bottom-heavy the vehicle is, in a given flight condition. This parameter plays an important role in determining longitudinal stability of wings-level gliding equilibria. The effect of varying ϱ on the stability of wings-level and turning equilibria has been investigated numerically. The results show that the equilibrium condition mentioned above is stable provided $\varrho > 0.05$, which agrees with the analysis in Section 8.3 of Bhatta's dissertation [26]. Here, the value of ϱ is fixed at 0.117, as in [26].

The eigenvalues of the state matrix corresponding to the given equilibrium condition are

$$\lambda \in \{-4.46, -2.67 \pm 1.64i, -1.26, -1.03, -0.75 \pm 0.25i, -0.07\}$$

All eight eigenvalues of the linearized system have negative real part, so the flight condition is stable.

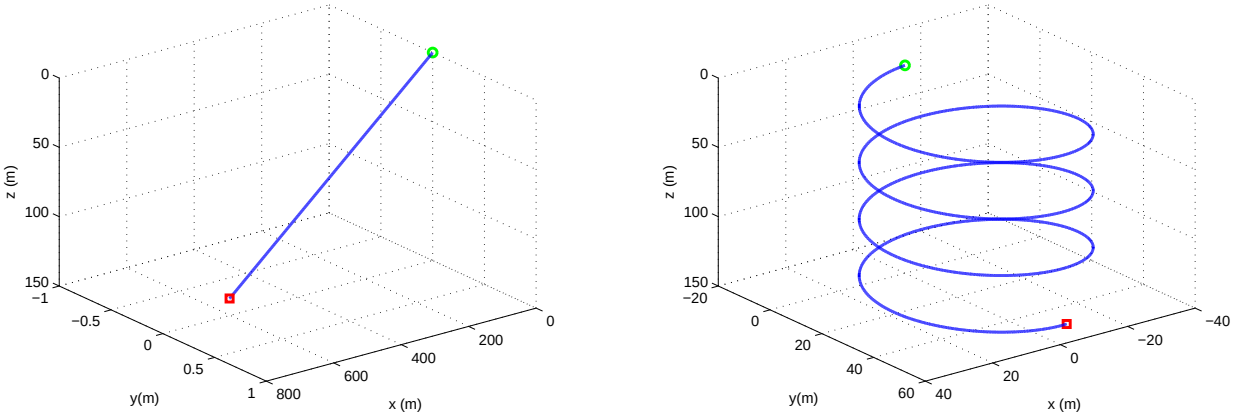

Figure 3.3 Wings level ($\epsilon = 0$) and turning ($\epsilon = 0.01$) flight paths for the *Slocum* model.

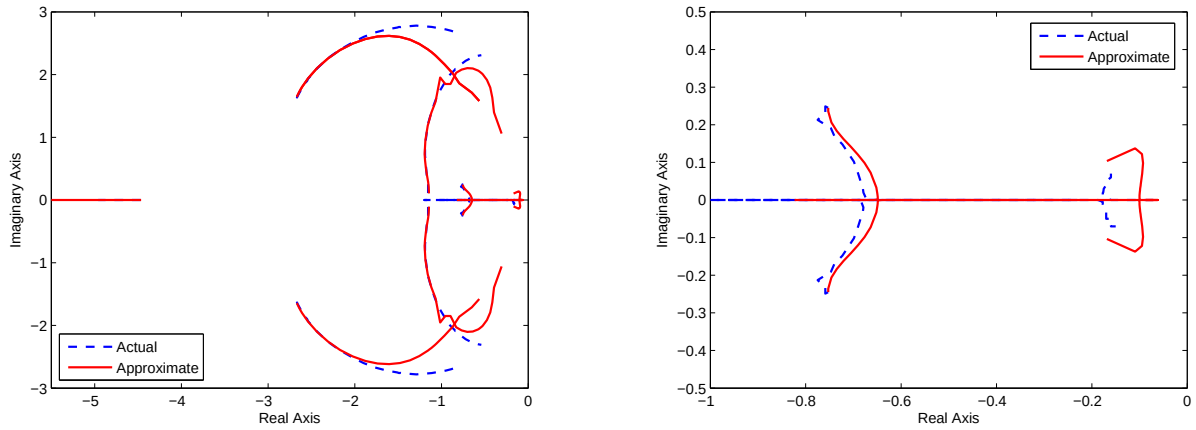

Figure 3.4 Eigenvalue plots for actual and approximate equilibria for $0 < \epsilon < 0.1$. (A closer view of the dominant eigenvalues is shown at the right.)

With stability of wings-level equilibrium flight confirmed, one may next compute the first-order solution for r_p, ϕ, and β, as described in Section 3.2:

$$r_\mathrm{p} = (4.63\omega_n\epsilon) \text{ m}, \qquad \phi = (10.06\omega_n\epsilon)\left(\frac{180}{\pi}\right) \text{ deg}, \qquad \text{and} \qquad \beta = (0.33\omega_n\epsilon)\left(\frac{180}{\pi}\right) \text{ deg}.$$

With these approximate values for lateral mass location, roll angle, and sideslip angle, the

approximate equilibrium velocity and angular velocity are

$$\boldsymbol{v} = V_0 \begin{pmatrix} \cos\alpha_0 \cos(\epsilon\beta_1) \\ \sin(\epsilon\beta_1) \\ \cos\alpha_0 \sin(\epsilon\beta_1) \end{pmatrix} \quad \text{and} \quad \boldsymbol{\omega} = \omega_n \epsilon \begin{pmatrix} \sin\theta_0 \\ \cos\theta_0 \sin(\epsilon\phi_1) \\ \cos\theta_0 \cos(\epsilon\phi_1) \end{pmatrix}.$$

When $\epsilon = 0$, the values above correspond to the given, steady, wings-level flight condition. For small, nonzero values of ϵ, the values correspond (approximately) to a steady turning motion; see Figure 3.3. To determine the range of stable turning motions that can be obtained using this approximation, the equations of motion are linearized about the approximate turning motion, parameterized by ϵ. When $\epsilon = 0$, all eight eigenvalues of the linearization have negative real part, with $\lambda_8 = -0.07$ being closest to the imaginary axis. As ϵ increases, this eigenvalue moves to the left along the real axis. The other critical eigenvalues start as a conjugate pair from $\lambda_{6,7} = .75 \mp .25i$. As ϵ increases, they move toward together to the right and break away when they meet on the real axis. One moves to the left and the other moves to the right along the real axis, which coalesces with λ_8 and then breaks away into a complex conjugate pair. One may infer that the system has a locally unique, stable fixed point provided ϵ remains smaller in order of magnitudes than the magnitude of the real part of the critical eigenvalue(s) [38]. Figure 3.4 shows the movement of eigenvalues for the approximate equilibrium as well as those for the true equilibrium (computed numerically) as ϵ increases from zero. The true and approximate root loci agree very closely for $\epsilon < 0.03$. The true system exhibits a stable turning motion for $0 < \epsilon < 0.1$. Table 3.1 gives approximate and actual values (obtained from numerical simulations) for key variables for various values of ϵ. Note that, as ϵ increases in value, so does the error between the approximate and true equilibrium values. Regardless, the system does converge to a steady turning motion for all values $\epsilon \leq 0.1$.

Remark 3.3.1 *Note in Table 3.1 that the actual turn radius R is minimum around $\epsilon = 0.05$. Since further increases in r_{p} (or equivalently in ϵ) fail to lower the turn radius, there is no point in moving the particle m_{p} beyond this critical location. Such an observation may provide*

Table 3.1 Approximate and actual steady motion conditions for $V_0 = 1.5$ knots and $\alpha = 4.3°$.

ϵ	ϕ (°)		β (°)		θ (°)	V (m/s)	ω (rad/s)		R (m)	
	app.	actual	app.	actual	actual†	actual†	app.	actual	app.	actual
0.001	1.47	1.43	0.05	0.12	-8.74	0.77	0.003	0.003	253.33	256.67
0.005	7.37	7.11	0.24	0.61	-8.82	0.78	0.013	0.014	58.46	55.71
0.01	14.73	13.89	0.49	1.28	-9.03	0.79	0.026	0.027	29.23	29.26
0.03	44.21	34.99	1.46	4.37	-9.8	0.87	0.077	0.057	9.87	15.26
0.05	73.69	47.84	2.43	6.99	-9.69	0.93	0.128	0.063	5.94	14.76
0.07	103.16	56.04	3.40	8.94	-9.01	0.97	0.179	0.060	4.25	16.17

†The approximate value of θ is $\theta_0 = -8.24°$. The approximate value of V is $V_0 = 0.758$ m/s.

guidelines for actuator sizing in future glider designs. There is no reason, for example, to provide moving mass control authority which does not yield greater turning ability.

Comparing the results for speeds of 1.0, 1.5, and 2.0 knots (illustrated in Tables 3.3, 3.1, and 3.2, respectively), one may observe several trends. For example, in every case, actual speed increases with increasing turn rate. (Recall that the approximation suggests that speed remains relatively constant, for small ϵ.) Roll angle and sideslip angle (approximate and actual) increase more rapidly with turn rate at lower nominal speeds than at higher nominal speeds. Moreover, the discrepancy between the approximate and actual values is greatest (for given ϵ) at the lowest speed. Because the relative stability of the nominal flight condition decreases with decreasing speed (i.e., the critical eigenvalues move closer to the imaginary axis), one should expect poorer agreement between the approximation and reality at these lower speeds.

Table 3.2 Approximate and actual steady motion conditions for $V_0 = 2.0$ knots and α= 4.3°.

ϵ	ϕ (°)		β (°)		θ (°)	V (m/s)	ω (rad/s)		R (m)	
	app.	actual	app.	actual	actual†	actual†	app.	actual	app.	actual
0.001	0.87	0.89	0.06	0.06	-8.02	1.002	0.003	0.003	337.00	334.00
0.005	4.34	4.42	0.29	0.29	-8.08	1.004	0.013	0.013	77.77	77.23
0.01	8.69	8.74	0.63	0.58	-8.24	1.011	0.026	0.026	39.55	39.33
0.03	26.06	23.85	2.29	2.29	-9.41	1.069	0.077	0.065	13.18	16.49
0.05	43.43	34.88	3.38	3.55	-10.41	1.144	0.128	0.085	7.91	13.46
0.07	60.80	42.80	4.70	4.92	-10.88	1.207	0.179	0.093	5.65	12.94

†The approximate value of θ is $\theta_0 = -8.24°$. The approximate value of V is $V_0 = 1.011$ m/s.

Table 3.3 Approximate and actual steady motion conditions for $V_0 = 1$ knot and α= 4.3°.

ϵ	ϕ (°)		β (°)		θ (°)	V (m/s)	ω (rad/s)		R (m)	
	app.	actual	app.	actual	actual†	actual†	app.	actual	app.	actual
0.001	2.93	2.77	0.01	0.28	-9.26	0.52	0.003	0.003	170.00	173.33
0.005	14.64	13.54	0.02	1.71	-9.31	0.53	0.013	0.015	39.23	35.33
0.01	29.28	25.42	0.03	3.43	-9.32	0.55	0.026	0.027	19.78	20.92
0.02	58.55	42.70	0.11	9.66	-8.74	0.60	0.051	0.034	9.89	17.99
0.03	87.83	53.54	0.17	12.61	-7.74	0.63	0.077	0.033	6.59	19.51
0.04	117.10	60.65	0.23	13.75	-6.75	0.65	0.102	0.029	4.95	22.03

†The approximate value of θ is $\theta_0 = -8.24°$. The approximate value of V is $V_0 = 0.5056$ m/s.

Chapter 4

Motion Control

Having characterized steady turning motions (at least approximately) in Section 3.2.2 as well as steady, wings level flight in Section 3.1, one can formulate a motion control strategy which relies on these solutions. The aim is to track desired speed (V_d), glide path angle (γ_d), and turn rate ($\dot{\psi}_\mathrm{d}$). Given feasible values for desired speed, glide path angle, and turn rate, for example, one may compute "feedforward" actuator commands to adjust the net weight and center of gravity in order to achieve the given flight condition. Because these values are only approximate, though, and because of modeling and environmental uncertainty, the commanded values must be augmented using feedback compensation. The design and analysis of such a feedforward/feedback motion control system requires a model that incorporates buoyancy and moving mass actuator dynamics as presented in Section 2.1.

An illustration of such a feedforward/feedback control system is shown in Figure 4.1. The vector field $\boldsymbol{f}(\boldsymbol{x}, \boldsymbol{u})$ represents the system dynamics with state vector $\boldsymbol{x}$ and inputs $\boldsymbol{u}$, and the vector field $\tilde{\boldsymbol{f}}(\boldsymbol{x}, \boldsymbol{u})$ notionally represents their first-order approximation in turn rate. The pair $(\tilde{\boldsymbol{x}}_\mathrm{eq}, \tilde{\boldsymbol{u}}_\mathrm{eq})$ represents the first-order solution for a given desired steady motion. The vector $\boldsymbol{\mu}$ contains parameter values which, if held constant, correspond to some stable steady motion. Such a feedforward/feedback motion control system was briefly presented in [33]; a more thorough discussion of the design and analysis was presented in [39].

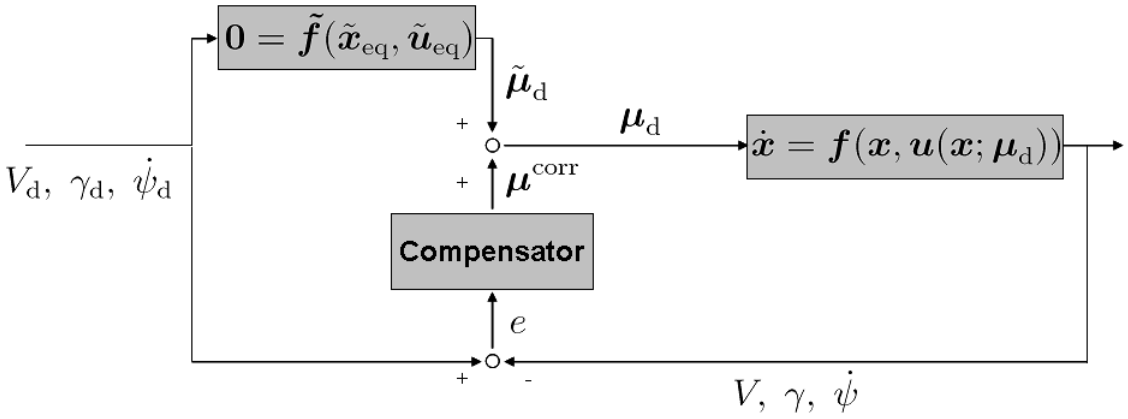

Figure 4.1 A steady motion-based feedforward/feedback control system.

The first step in the motion control scheme is to obtain the parameter values $\tilde{\boldsymbol{\mu}}_{\mathrm{d}}$ (net mass and moving mass positions) that correspond to the desired steady motion $\tilde{\boldsymbol{x}}_{\mathrm{eq}}$ (characterized by V_{d}, γ_{d}, and $\dot{\psi}_{\mathrm{d}}$), to first order in turn rate. This inverse problem is expressed notationally in the feedforward block in Figure 4.1 by the equation

$$\mathbf{0} = \tilde{\boldsymbol{f}}(\tilde{\boldsymbol{x}}_{\mathrm{eq}}, \tilde{\boldsymbol{u}}_{\mathrm{eq}}),$$

which was solved analytically for the corresponding parameter values $\tilde{\boldsymbol{\mu}}_{\mathrm{d}}$ in [32].

The feedback block compensates for the error due to the approximation and environmental uncertainty, adding a correction denoted $\boldsymbol{\mu}^{\mathrm{corr}}$.

The feedback-compensated "parameter commands" $\boldsymbol{\mu}_{\mathrm{d}}$ are then realized within the vehicle dynamics

$$\dot{\boldsymbol{x}} = \boldsymbol{f}(\boldsymbol{x}; \boldsymbol{u}(\boldsymbol{x}; \boldsymbol{\mu}_{\mathrm{d}}))$$

through an appropriately designed servo-control system. Here, $\boldsymbol{u}$ is a feedback control law that attempts to maintain commanded parameter values $\boldsymbol{\mu}_{\mathrm{d}}$ in spite of the vehicle dynamics.

The control system depicted in Figure 4.1 suggests that one may vary the steady motion according to some desired guidance objective. However, one must verify that the closed-loop system is stable. Fixing parameter values, one may examine open-loop stability by linearizing about the approximate equilibrium conditions and computing the eigenvalues of the state

matrix. Because eigenvalues depend continuously on the matrix parameters, stability of the true equilibrium may be inferred from stability of the approximate equilibrium provided (i) the equilibrium is hyperbolic and (ii) ϵ is small relative to the magnitude of the real part of each eigenvalue. See Section 1.7 of [37] for a brief discussion or Chapter 9 of [38] for more details. Given that the system does possess a stable, steady motion parameterized by a set of commanded parameter values, one must still verify that the system remains stable while varying these parameter values. For example, if one changes the reference commands in Figure 4.1 too rapidly, one might drive the nonlinear system into instability.

As explained earlier, underwater gliders steer by moving one or more internal masses. The vehicle dynamics are quite slow, relative to the actuator dynamics. Commanding a rapid change in turn rate, for example, will result in a quick change in center of mass location, but the resulting effect on the vehicle's motion will be much slower. Alternatively, one may issue reference commands that vary "quasisteadily" and treat the closed-loop system as "slowly varying" in the turn rate $\dot{\psi}_{\mathrm{d}}(t)$. We may then analyze stability of the closed-loop system in the context of slowly varying systems theory [40].

Suppose the output of a nonlinear system

$$\dot{\boldsymbol{x}} = f(\boldsymbol{x}, u_{\mathrm{p_y}}) \; ; \quad u_{\mathrm{p_y}} = \kappa(\boldsymbol{x}, \dot{\psi}_{\mathrm{d}})$$

is required to track a reference input $\dot{\psi}_{\mathrm{d}}(t)$, where the feedback controller κ is designed such that the closed-loop system has a locally exponentially stable equilibrium at $\boldsymbol{x}_{\mathrm{eq}}$ when $\dot{\psi}_{\mathrm{d}}(t)$ is constant. The turn rate $\dot{\psi}_{\mathrm{d}}(t)$ is called "slowly varying" if it is continuously differentiable and, for some sufficiently small $\varepsilon > 0$, one has $\|\ddot{\psi}_{\mathrm{d}}(t)\| \leq \varepsilon$ for all $t \geq 0$.

We will analyze the underwater glider's motion control system using slowly varying systems theory to prove stability of the closed-loop system and, simultaneously, to determine how fast one may vary the commanded turn rate and maintain stability.

To analyze this system, consider $\dot{\psi}_{\mathrm{d}}$ as a "frozen" parameter and assume that for each fixed value the frozen system has an isolated equilibrium point defined by $\boldsymbol{x}_{\mathrm{eq}} = \mathbf{h}(\dot{\psi}_{\mathrm{d}})$ where $\|\frac{\partial \mathbf{h}}{\partial \dot{\psi}_{\mathrm{d}}}\| \leq L$. To analyze stability of the frozen equilibrium point, we shift it to the origin via

the change of the variables $\acute{\boldsymbol{x}} = \boldsymbol{x} - \mathbf{h}(\dot{\psi}_{\mathrm{d}})$ to obtain equation

$$\dot{\acute{\boldsymbol{x}}} = g(\acute{\boldsymbol{x}}).$$

Based on Theorem 9.3 of Khalil [40], if there is a positive definite and decrescent Lyapunov function $V(\acute{\boldsymbol{x}})$ that has a negative definite derivative along the trajectories of the system, and which satisfies certain inequalities to handle the perturbation –and the fact that $\dot{\psi}_{\mathrm{d}}(t)$ is not constant–, the solution will be uniformly ultimately bounded within a ball around the equilibrium point, with a radius proportional to ε, for sufficiently small ε. Moreover, if $\ddot{\psi}_{\mathrm{d}}(t) \to 0$ as $t \to \infty$, then the tracking error tends to zero.

4.1 Feedforward/Feedback Controller Design

The feedforward block takes the commanded steady motion parameters (speed, glide path angle, and turn rate) and generates the corresponding values for buoyancy and center of mass location, as predicted by perturbation analysis. Because the turning motion results are only approximate, however, and to compensate for model and environmental uncertainty, we incorporate feedback. The objective here is to design single-input, single-output PID control loops to *modify* the feedforward commands based on measured errors in the values of speed V, glide path angle $\gamma = \theta - \alpha$, and heading rate $\dot{\psi} = \frac{\sin\phi}{\cos\theta} q + \frac{\cos\phi}{\cos\theta} r$. Speed and glide path angle are inherently coupled for underwater gliders, just as they are for airplanes. For a *fixed* glide path angle, speed can be directly modulated by changing the net mass $\tilde{m}$. Changing $\tilde{m}$ requires pressure-volume work, however, which is relatively expensive, especially at depth. In practice, it is best to modulate $\tilde{m}$ as infrequently as possible. Here, we focus on controlling the glide path angle γ by varying the longitudinal moving mass position $r_{\mathrm{p_x}}$.

A sophisticated dynamic model presented in Section 2.1 has been used to design the feedback compensator. The model incorporates the buoyancy and moving mass actuator dynamics and servo-control laws. It is convenient to replace the velocity $\boldsymbol{v}$, as expressed in the body reference frame, with speed, angle of attack, and sideslip angle (V, α, β). To do so,

note that

$$\begin{aligned}
\boldsymbol{v} &= e^{-\widehat{\boldsymbol{e}_2}\alpha} e^{\widehat{\boldsymbol{e}_3}\beta} (V\boldsymbol{e}_1) \\
\dot{\boldsymbol{v}} &= e^{-\widehat{\boldsymbol{e}_2}\alpha} e^{\widehat{\boldsymbol{e}_3}\beta} \begin{pmatrix} 1 & 0 & 0 \\ 0 & 0 & V \\ 0 & V\cos\beta & 0 \end{pmatrix} \begin{pmatrix} \dot{V} \\ \dot{\alpha} \\ \dot{\beta} \end{pmatrix}.
\end{aligned}$$

The change of variables is well-defined for $\beta \in (-\frac{\pi}{2}, \frac{\pi}{2})$.

The equations of motion (2.7) can be written in the form

$$\mathbb{F}(\dot{\mathbb{X}}, \mathbb{X}, \mathbb{U}) = \mathbf{0}$$

where the system state and control vectors are

$$\begin{aligned}
\mathbb{X} &= \left[\phi, \theta, V, \alpha, \beta, p, q, r, r_{\mathrm{p_x}}, v_{\mathrm{p_x}}, r_{\mathrm{p_y}}, v_{\mathrm{p_y}}\right]^T \\
\mathbb{U} &= \left[u_{\mathrm{p_x}}, u_{\mathrm{p_y}}, u_{\mathrm{b}}\right]^T.
\end{aligned}$$

Note that $v_{\mathrm{p_x}}$ and $v_{\mathrm{p_y}}$ represent the translational velocity of the moving masses relative to the inertial frame expressed in the body frame.

To design a servo-controller for the moving mass actuators and the variable ballast actuator, we linearize the dynamic equations about a wings-level equilibrium $(\mathbb{X}_0, \mathbb{U}_0)$ and compute the transfer function for each input-output channel of interest. Let U denote one of the available input signals $U \in \left\{u_{\mathrm{p_x}}, u_{\mathrm{p_y}}, u_{\mathrm{b}}\right\}$ and define a corresponding output $Y(\mathbb{X})$. With these definitions, we obtain the perturbation equations

$$\triangle\dot{\mathbb{X}} = \boldsymbol{A}\triangle\mathbb{X} + \boldsymbol{B}\triangle U \tag{4.1}$$

$$\triangle Y = \boldsymbol{C}\triangle\mathbb{X} \tag{4.2}$$

where

$$\begin{aligned}
\boldsymbol{A} &= -\left[\left(\frac{\partial\mathbb{F}}{\partial\dot{\mathbb{X}}}\right)^{-1}\left(\frac{\partial\mathbb{F}}{\partial\mathbb{X}}\right)\right]_{\mathrm{eq}} \\
\boldsymbol{B} &= -\left[\left(\frac{\partial\mathbb{F}}{\partial\dot{\mathbb{X}}}\right)^{-1}\left(\frac{\partial\mathbb{F}}{\partial U}\right)\right]_{\mathrm{eq}} \\
\boldsymbol{C} &= \left[\frac{\partial Y}{\partial\mathbb{X}}\right]_{\mathrm{eq}}.
\end{aligned}$$

The matrix $\frac{\partial \mathbb{F}}{\partial \dot{\mathbb{X}}}$ is non-singular within the vehicle's normal performance envelope.

In designing moving mass servo-controllers, the objective is to choose an input $u_{\mathrm{p}} \in \{u_{\mathrm{p}_x}, u_{\mathrm{p}_y}\}$ such that the position of the moving mass $r_{\mathrm{p}} \in \{r_{\mathrm{p}_x}, r_{\mathrm{p}_y}\}$ asymptotically tracks a desired trajectory $r_{\mathrm{p_d}} \in \{r_{\mathrm{p}_{x_{\mathrm{d}}}}, r_{\mathrm{p}_{y_{\mathrm{d}}}}\}$. With $U = u_{\mathrm{p}}$ and $Y = r_{\mathrm{p}}$ in equations (4.1) and (4.2), the scalar $\boldsymbol{CAB}$ is nonzero. Let $e = r_{\mathrm{p_d}} - r_{\mathrm{p}}$ represent the error between the desired position of a moving mass and its current position. In order to drive e to zero, one may choose

$$u_{\mathrm{p}} = \frac{1}{\mathbf{CAB}}(\ddot{r}_{\mathrm{p_d}} - \mathbf{CA}^2 \triangle \mathbb{X} + [\omega_{\mathrm{n}}^2 \quad 2\zeta\omega_{\mathrm{n}}]\mathbf{e}),$$

where $\mathbf{e} = [e, \dot{e}]^T$ and where $\omega_{\mathrm{n}} \in \{\omega_{\mathrm{n}_x}, \omega_{\mathrm{n}_y}\}$ and $\zeta \in \{\zeta_x, \zeta_y\}$ are appropriately chosen control parameters, assuming that $r_{\mathrm{p_d}}$ is twice differentiable.

To design a PID compensator to correct the feedforward commands, let $G(s)$ represent the transfer function for a particular control channel and let $G_{\mathrm{c}}(s)$ represent the PID controller:

$$G_c(s) = K_p(1 + \frac{1}{T_i s} + T_d s).$$

The proportional gain K_p, the integrator time T_i, and the derivative time T_d are control parameters to be tuned by the control designer. In the time domain, the control signal is

$$r_{\mathrm{p}}^{\mathrm{corr}} = K_p e + K_i \int_{t_0}^{t} e(\tau)d\tau + K_d \dot{e},$$

where $K_i = K_p/T_i$ and $K_d = K_p T_d$. The error signal $e(t)$ measures the difference between the actual and commanded value of the output.

The approximate equilibrium value of $\tilde{r}_{\mathrm{p_d}} \in \{\tilde{r}_{\mathrm{p}_{x_{\mathrm{d}}}}, \tilde{r}_{\mathrm{p}_{y_{\mathrm{d}}}}\}$, as predicted by analytical solutions, is augmented with feedback compensation to compensate for approximation error:

$$r_{\mathrm{p_d}} \quad = \quad \tilde{r}_{\mathrm{p_d}} + r_{\mathrm{p}}^{\mathrm{corr}}.$$

To smooth the commanded parameter value so that the reference command to the internal servo-actuators is twice differentiable, we define a linear reference model:

$$F(s) : r_{\mathrm{p_d}} \rightarrow r_{\mathrm{p_d}}^{\mathrm{comm}} \qquad \text{where} \qquad F(s) = \frac{1}{(s/\omega_{\mathrm{r}})^2 + 2\zeta_{\mathrm{r}}(s/\omega_{\mathrm{r}}) + 1}.$$

Equivalently, in time domain, define the following reference model dynamics for each servo-actuator:

$$\begin{aligned} \dot{\mathbf{z}} &= \begin{pmatrix} 0 & 1 \\ -\omega_{\mathrm{r}}^2 & -2\zeta_{\mathrm{r}}\omega_{\mathrm{r}} \end{pmatrix} \mathbf{z} + \begin{pmatrix} 0 \\ \omega_{\mathrm{r}}^2 \end{pmatrix} r_{\mathrm{p_d}} \\ r_{\mathrm{p_d}}^{\mathrm{comm}} &= \begin{pmatrix} 1 & 0 \end{pmatrix} \mathbf{z} \end{aligned}$$

where $r_{\mathrm{p_d}}(t) \in \{r_{\mathrm{p_{x_d}}}(t), r_{\mathrm{p_{y_d}}}(t)\}$ is the (possibly discontinuous) reference command to be filtered.

In physical implementations, the servo-actuation system is self-contained and there is no need to include it in the motion control system. Referring to the control system schematic in Figure 4.1, this reference command filter is internal to the system dynamics block appearing at the right. We include this element explicitly here in order to account for the full complexity of the multi-body mechanical system and to allow analysis of issues such as actuator magnitude and rate saturation. Actuator rate and magnitude saturation can be important issues for underwater gliders. The natural frequency and damping ratio parameters in the reference model above may be chosen to accommodate actuator performance limitations through analysis and simulation.

For a *fixed* glide path angle, speed can be directly modulated by changing the net mass $\tilde{m}$. That is, given values θ_0 and γ_0, one may solve relation (3.6) for the corresponding values of $\tilde{m}_{\mathrm{d}}$. We design an input u_{b} such that the net mass $\tilde{m}$ asymptotically tracks a desired value $\tilde{m}_{\mathrm{d}}$. The simplest approach is to choose

$$u_{\mathrm{b}} = k_{\mathrm{b}} \left(\tilde{m}_{\mathrm{d}} - \tilde{m} \right)$$

where the constant k_{b} is chosen to accommodate the rate limit on u_{b}.

4.2 Flight Path Control

We control the glide path angle γ by modulating the longitudinal moving mass position $r_{\mathrm{p_x}}$. Let $e_\gamma(t) = \gamma_\mathrm{d} - \gamma(t)$, where γ_d is the desired value of the glide path angle. The longitudinal moving mass reference signal is

$$r_{\mathrm{p_x}}^{\mathrm{corr}} = K_{p_\gamma} e_\gamma + K_{i_\gamma} \int_{t_0}^{t} e_\gamma(\tau) d\tau + K_{d_\gamma} \dot{e}_\gamma.$$

The first step is to tune the flight path controller for the linearized system dynamics. Having done so, the next step is to re-tune the controller as necessary for the nonlinear dynamics through simulation. Adding the result to the longitudinal moving mass position from the feedforward block gives the required position of the longitudinal moving mass to maintain a constant flight path angle:

$$r_{\mathrm{p_{x_d}}} \quad = \quad \tilde{r}_{\mathrm{p_{x_d}}} + r_{\mathrm{p_x}}^{\mathrm{corr}}.$$

As explained in Section 2.1.2 we assumed that the nominal gravitational moment is due entirely to $\mathbf{r}_{\mathrm{rb}}$ and that $\tilde{r}_{\mathrm{p_{x_d}}} = 0$. Hence, for $\gamma_\mathrm{d} = \gamma_0$, we have only the feedback term $r_{\mathrm{p_{x_d}}} = r_{\mathrm{p_x}}^{\mathrm{corr}}$.

The reference command should be filtered to accommodate the magnitude and rate limit on the longitudinal moving mass actuator due to limited range of travel of the moving mass and the operational limit of the servomotor driving it:

$$r_{\mathrm{p_{x_d}}}^{\mathrm{comm}} \quad = \quad \begin{pmatrix} 1 & 0 \end{pmatrix} \mathbf{z}_\mathrm{x} \;\; \text{where} \;\; \dot{\mathbf{z}}_\mathrm{x} = \begin{pmatrix} 0 & 1 \\ -\omega_{\mathrm{r_x}}^2 & -2\zeta_{\mathrm{r_x}}\omega_{\mathrm{r_x}} \end{pmatrix} \mathbf{z}_\mathrm{x} + \begin{pmatrix} 0 \\ \omega_{\mathrm{r_x}}^2 \end{pmatrix} r_{\mathrm{p_{x_d}}}(t).$$

The input $u_{\mathrm{p_x}}$ guarantees that the position of the longitudinal moving mass $r_{\mathrm{p_x}}$ asymptotically tracks the (twice-differentiable) trajectory $r_{\mathrm{p_{x_d}}}^{\mathrm{comm}}$ generated by filtering (possibly discontinuous) desired value $r_{\mathrm{p_{x_d}}}$:

$$u_{\mathrm{p_x}} = \frac{(\ddot{r}_{\mathrm{p_{x_d}}}^{\mathrm{comm}} - \boldsymbol{C}_\mathrm{x}\boldsymbol{A}^2\boldsymbol{X} + [\omega_{\mathrm{n_x}}^2 \quad 2\zeta_\mathrm{x}\omega_{\mathrm{n_x}}]\mathbf{e}_\mathrm{x})}{\boldsymbol{C}_\mathrm{x}\boldsymbol{A}\boldsymbol{B}_\mathrm{x}} \qquad \text{where} \qquad \boldsymbol{e}_\mathrm{x} = (e_\mathrm{x}, \dot{e}_\mathrm{x})^T \;\; \& \;\; e_\mathrm{x} = r_{\mathrm{p_{x_d}}}^{\mathrm{comm}} - r_{\mathrm{p_x}}.$$

4.3 Turn Rate Control

The channel from lateral mass position $r_{\mathrm{p_y}}^{\mathrm{corr}}$ to turn rate $\dot{\psi}$ is non-minimum phase, with a single zero in the right half plane. This non-minimum phase zero limits closed-loop bandwidth. In any case, closing the loop from turn rate to lateral mass location is quite effective, provided the performance limitations are respected in control parameter selection. Let $e_{\dot{\psi}}(t) = \dot{\psi}_{\mathrm{d}}(t) - \dot{\psi}(t)$, where $\dot{\psi}_{\mathrm{d}}(t)$ is the desired turn rate. The lateral moving mass control signal is

$$r_{\mathrm{p_y}}^{\mathrm{corr}} = K_{p_{\dot{\psi}}} e_{\dot{\psi}} + K_{i_{\dot{\psi}}} \int_{t_0}^{t} e_{\dot{\psi}}(\tau) d\tau + K_{d_{\dot{\psi}}} \dot{e}_{\dot{\psi}}.$$

The turn rate PID controller was first tuned for the linearized system dynamics, and then re-tuned for the nonlinear dynamics through simulation. Adding the result to the lateral moving mass position from the feedforward block gives the required position of the lateral moving mass to maintain the desired turn rate:

$$r_{\mathrm{p_{y_d}}} \;=\; \tilde{r}_{\mathrm{p_{y_d}}} + r_{\mathrm{p_y}}^{\mathrm{corr}}.$$

The reference command should be filtered to accommodate magnitude and rate limits on the lateral moving mass actuator due to the limited range of travel of battery pack and the operational limit of servomotor driving it:

$$r_{\mathrm{p_{y_d}}}^{\mathrm{comm}} \;=\; \begin{pmatrix} 1 & 0 \end{pmatrix} \mathbf{z}_{\mathrm{y}} \;\text{ where }\; \dot{\mathbf{z}}_{\mathrm{y}} = \begin{pmatrix} 0 & 1 \\ -\omega_{\mathrm{r_y}}^2 & -2\zeta_{\mathrm{r_y}}\omega_{\mathrm{r_y}} \end{pmatrix} \mathbf{z}_{\mathrm{y}} + \begin{pmatrix} 0 \\ \omega_{\mathrm{r_y}}^2 \end{pmatrix} r_{\mathrm{p_{y_d}}}(t).$$

The input $u_{\mathrm{p_y}}$ guarantees that the position of the lateral moving mass $r_{\mathrm{p_y}}$ asymptotically tracks the (twice-differentiable) trajectory $r_{\mathrm{p_{y_d}}}^{\mathrm{comm}}$ generated by filtering (possibly discontinuous) desired value $r_{\mathrm{p_{y_d}}}$:

$$u_{\mathrm{p_y}} = \frac{(\ddot{r}_{\mathrm{p_{y_d}}}^{\mathrm{comm}} - \boldsymbol{C}_{\mathrm{y}}\boldsymbol{A}^2\boldsymbol{X} + [\omega_{\mathrm{n_y}}^2 \quad 2\zeta_{\mathrm{y}}\omega_{\mathrm{n_y}}]\mathbf{e}_{\mathrm{y}})}{\boldsymbol{C}_{\mathrm{y}}\boldsymbol{A}\boldsymbol{B}_{\mathrm{y}}} \qquad \text{where} \qquad \boldsymbol{e}_{\mathrm{y}} = (e_{\mathrm{y}}, \dot{e}_{\mathrm{y}})^T \;\;\&\;\; e_{\mathrm{y}} = r_{\mathrm{p_{y_d}}}^{\mathrm{comm}} - r_{\mathrm{p_y}}.$$

4.4 Stability Analysis of Closed-Loop System

To analyze this system, consider $\dot{\psi}_{\mathrm{d}}$ as a frozen parameter. For each fixed value the frozen system has an isolated equilibrium point. Consider the linearized equations about this equilibrium point:

$$\begin{aligned} \dot{\mathbb{X}} &= \boldsymbol{A}\mathbb{X} + \boldsymbol{B}_{\mathrm{y}} u_{\mathrm{p_y}} \\ r_{\mathrm{p_y}} &= \boldsymbol{C}_{\mathrm{y}}\mathbb{X}, \end{aligned}$$

where $\mathbb{X}$ is the state vector

$$\mathbb{X} = \left[\phi, \theta, V, \alpha, \beta, p, q, r, r_{\mathrm{p_x}}, v_{\mathrm{p_x}}, r_{\mathrm{p_y}}, v_{\mathrm{p_y}}\right]^T.$$

Defining the lateral mass error $e_{\mathrm{y}} = r^{\mathrm{comm}}_{\mathrm{p_{y_d}}} - r_{\mathrm{p_y}}$ and the heading rate error $e_{\dot{\psi}} = \dot{\psi}_{\mathrm{d}} - \dot{\psi}$, the input $u_{\mathrm{p_y}}$ is

$$u_{\mathrm{p_y}} = \frac{(\ddot{r}^{\mathrm{comm}}_{\mathrm{p_{y_d}}} - \boldsymbol{C}_{\mathrm{y}}\boldsymbol{A}^2\mathbb{X} + \begin{pmatrix} \omega^2_{\mathrm{n_y}} & 2\zeta_{\mathrm{y}}\omega_{\mathrm{n_y}} \end{pmatrix} \mathbf{e}_{\mathrm{y}})}{\boldsymbol{C}_{\mathrm{y}}\boldsymbol{A}\boldsymbol{B}_{\mathrm{y}}} \quad \text{where} \quad \boldsymbol{e}_{\mathrm{y}} = (e_{\mathrm{y}}, \dot{e}_{\mathrm{y}})^T$$

$$r^{\mathrm{comm}}_{\mathrm{p_{y_d}}} = \begin{pmatrix} 1 & 0 \end{pmatrix} \mathbf{z}_{\mathrm{y}} \quad \text{where} \quad \dot{\mathbf{z}}_{\mathrm{y}} = \begin{pmatrix} 0 & 1 \\ -\omega^2_{\mathrm{r_y}} & -2\zeta_{\mathrm{r_y}}\omega_{\mathrm{r_y}} \end{pmatrix} \mathbf{z}_{\mathrm{y}} + \begin{pmatrix} 0 \\ \omega^2_{\mathrm{r_y}} \end{pmatrix} r_{\mathrm{p_{y_d}}}(t)$$

$$r_{\mathrm{p_{y_d}}} = \tilde{r}_{\mathrm{p_{y_d}}} + r^{\mathrm{corr}}_{\mathrm{p_y}} \quad \text{with} \quad r^{\mathrm{corr}}_{\mathrm{p_y}} = K_{p_{\dot{\psi}}} e_{\dot{\psi}} + K_{i_{\dot{\psi}}} z_{\dot{\psi}} + K_{d_{\dot{\psi}}} \dot{e}_{\dot{\psi}} \quad \text{where} \quad \dot{z}_{\dot{\psi}} = e_{\dot{\psi}}.$$

Putting all the parts together, we have

$$\begin{aligned} \dot{\mathbb{X}} &= \boldsymbol{A}\mathbb{X} + \boldsymbol{B}_{\mathrm{y}} u_{\mathrm{p_y}} \\ \dot{\mathbf{z}}_{\mathrm{y}} &= \begin{pmatrix} 0 & 1 \\ -\omega^2_{\mathrm{r_y}} & -2\zeta_{\mathrm{r_y}}\omega_{\mathrm{r_y}} \end{pmatrix} \mathbf{z}_{\mathrm{y}} + \begin{pmatrix} 0 \\ \omega^2_{\mathrm{r_y}} \end{pmatrix} (\tilde{r}_{\mathrm{p_{y_d}}} + K_{p_{\dot{\psi}}} e_{\dot{\psi}} + K_{i_{\dot{\psi}}} z_{\dot{\psi}} + K_{d_{\dot{\psi}}} \dot{e}_{\dot{\psi}}) \\ \dot{z}_{\dot{\psi}} &= \dot{\psi}_d - \dot{\psi} \end{aligned}$$

where

$$
\begin{aligned}
u_{\mathrm{p_y}} &= \frac{1}{\boldsymbol{C}_{\mathrm{y}}\boldsymbol{A}\boldsymbol{B}_{\mathrm{y}}}\left[\begin{pmatrix} 0 & 1 \end{pmatrix}\dot{\mathbf{z}}_{\mathrm{y}} - \boldsymbol{C}_{\mathrm{y}}\boldsymbol{A}^2\mathbb{X} + \begin{pmatrix} \omega_{\mathrm{n_y}}^2 & 2\zeta_{\mathrm{y}}\omega_{\mathrm{n_y}} \end{pmatrix}\begin{pmatrix} \begin{pmatrix} 1 & 0 \end{pmatrix}\mathbf{z}_{\mathrm{y}} - r_{\mathrm{p_y}} \\ \begin{pmatrix} 1 & 0 \end{pmatrix}\dot{\mathbf{z}}_{\mathrm{y}} - v_{\mathrm{p_y}} \end{pmatrix}\right] \\
&= \frac{1}{\boldsymbol{C}_{\mathrm{y}}\boldsymbol{A}\boldsymbol{B}_{\mathrm{y}}}\left[-\begin{pmatrix} \omega_{\mathrm{r_y}}^2 & 2\zeta_{\mathrm{r_y}}\omega_{\mathrm{r_y}} \end{pmatrix}\mathbf{z}_{\mathrm{y}} + \omega_{\mathrm{r_y}}^2[\tilde{r}_{\mathrm{p_{y_d}}} + \begin{pmatrix} K_{p_{\dot{\psi}}} & K_{d_{\dot{\psi}}} \end{pmatrix}\begin{pmatrix} e_{\dot{\psi}} \\ \dot{e}_{\dot{\psi}} \end{pmatrix} + K_{i_{\dot{\psi}}}z_{\dot{\psi}}]\right] \\
&\quad + \frac{1}{\boldsymbol{C}_{\mathrm{y}}\boldsymbol{A}\boldsymbol{B}_{\mathrm{y}}}\left[\begin{pmatrix} \omega_{\mathrm{n_y}}^2 & 2\zeta_{\mathrm{y}}\omega_{\mathrm{n_y}} \end{pmatrix}\mathbf{z}_{\mathrm{y}} - \begin{pmatrix} \omega_{\mathrm{n_y}}^2 & 2\zeta_{\mathrm{y}}\omega_{\mathrm{n_y}} \end{pmatrix}\begin{pmatrix} r_{\mathrm{p_y}} \\ v_{\mathrm{p_y}} \end{pmatrix} - \boldsymbol{C}_{\mathrm{y}}\boldsymbol{A}^2\mathbb{X}\right] \\
&= \frac{1}{\boldsymbol{C}_{\mathrm{y}}\boldsymbol{A}\boldsymbol{B}_{\mathrm{y}}}\left[\omega_{\mathrm{r_y}}^2\tilde{r}_{\mathrm{p_{y_d}}} + \omega_{\mathrm{r_y}}^2\begin{pmatrix} K_{p_{\dot{\psi}}} & K_{d_{\dot{\psi}}} \end{pmatrix}\begin{pmatrix} e_{\dot{\psi}} \\ \dot{e}_{\dot{\psi}} \end{pmatrix} - \begin{pmatrix} \omega_{\mathrm{n_y}}^2 & 2\zeta_{\mathrm{y}}\omega_{\mathrm{n_y}} \end{pmatrix}\begin{pmatrix} r_{\mathrm{p_y}} \\ v_{\mathrm{p_y}} \end{pmatrix}\right] \\
&\quad + \frac{1}{\boldsymbol{C}_{\mathrm{y}}\boldsymbol{A}\boldsymbol{B}_{\mathrm{y}}}\left[\begin{pmatrix} -1 & 1 \end{pmatrix}\begin{pmatrix} \omega_{\mathrm{r_y}}^2 & 2\zeta_{\mathrm{r_y}}\omega_{\mathrm{r_y}} \\ \omega_{\mathrm{n_y}}^2 & 2\zeta_{\mathrm{y}}\omega_{\mathrm{n_y}} \end{pmatrix}\mathbf{z}_{\mathrm{y}} + \omega_{\mathrm{r_y}}^2 K_{i_{\dot{\psi}}}z_{\dot{\psi}} - \boldsymbol{C}_{\mathrm{y}}\boldsymbol{A}^2\mathbb{X}\right].
\end{aligned}
$$

Define $\boldsymbol{C}_{\dot{\psi}}$ so that $\boldsymbol{C}_{\dot{\psi}}\mathbb{X} = \begin{pmatrix} e_{\dot{\psi}} \\ \dot{e}_{\dot{\psi}} \end{pmatrix}$ and $\boldsymbol{C}_{\mathrm{p_y}}$ so that $\boldsymbol{C}_{\mathrm{p_y}}\mathbb{X} = \begin{pmatrix} r_{\mathrm{p_y}} \\ v_{\mathrm{p_y}} \end{pmatrix}$.

Next, we shift the frozen equilibrium point $\mathbf{h}(\dot{\psi}_{\mathrm{d}}) = (\mathbb{X}_{\mathrm{eq}}^T, \mathbf{z}_{\mathrm{y_{eq}}}^T, z_{\dot{\psi}_{\mathrm{eq}}})^T$ to the origin to analyze stability. Define

$$
(\acute{\mathbb{X}}^T, \acute{\mathbf{z}}_{\mathrm{y}}^T, \acute{z}_{\dot{\psi}})^T = (\mathbb{X}^T, \mathbf{z}_{\mathrm{y}}^T, z_{\dot{\psi}})^T - \mathbf{h}(\dot{\psi}_{\mathrm{d}}).
$$

The complete linearized equations are

$$
\begin{aligned}
\dot{\acute{\mathbb{X}}} &= \left[\boldsymbol{A} + \boldsymbol{B}_{\mathrm{y}}\frac{1}{\boldsymbol{C}_{\mathrm{y}}\boldsymbol{A}\boldsymbol{B}_{\mathrm{y}}}\left[\omega_{\mathrm{r_y}}^2\begin{pmatrix} K_{p_{\dot{\psi}}} & K_{d_{\dot{\psi}}} \end{pmatrix}\boldsymbol{C}_{\dot{\psi}} - \begin{pmatrix} \omega_{\mathrm{n_y}}^2 & 2\zeta_{\mathrm{y}}\omega_{\mathrm{n_y}} \end{pmatrix}\boldsymbol{C}_{\mathrm{p_y}} - \boldsymbol{C}_{\mathrm{y}}\boldsymbol{A}^2\right]\right]\acute{\mathbb{X}} \\
&\quad + \boldsymbol{B}_{\mathrm{y}}\frac{1}{\boldsymbol{C}_{\mathrm{y}}\boldsymbol{A}\boldsymbol{B}_{\mathrm{y}}}\left[\begin{pmatrix} -1 & 1 \end{pmatrix}\begin{pmatrix} \omega_{\mathrm{r_y}}^2 & 2\zeta_{\mathrm{r_y}}\omega_{\mathrm{r_y}} \\ \omega_{\mathrm{n_y}}^2 & 2\zeta_{\mathrm{y}}\omega_{\mathrm{n_y}} \end{pmatrix}\right]\acute{\mathbf{z}}_{\mathrm{y}} + \boldsymbol{B}_{\mathrm{y}}\frac{1}{\boldsymbol{C}_{\mathrm{y}}\boldsymbol{A}\boldsymbol{B}_{\mathrm{y}}}\omega_{\mathrm{r_y}}^2 K_{i_{\dot{\psi}}}\acute{z}_{\dot{\psi}} \\
\dot{\acute{\mathbf{z}}}_{\mathrm{y}} &= \begin{pmatrix} 0 \\ \omega_{\mathrm{r_y}}^2 \end{pmatrix}\begin{pmatrix} K_{p_{\dot{\psi}}} & K_{d_{\dot{\psi}}} \end{pmatrix}\boldsymbol{C}_{\dot{\psi}}\acute{\mathbb{X}} + \begin{pmatrix} 0 & 1 \\ -\omega_{\mathrm{r_y}}^2 & -2\zeta_{\mathrm{r_y}}\omega_{\mathrm{r_y}} \end{pmatrix}\acute{\mathbf{z}}_{\mathrm{y}} + \begin{pmatrix} 0 \\ \omega_{\mathrm{r_y}}^2 \end{pmatrix}K_{i_{\dot{\psi}}}\acute{z}_{\dot{\psi}} \quad (4.3) \\
\dot{\acute{z}}_{\dot{\psi}} &= \begin{pmatrix} -1 & 0 \end{pmatrix}\boldsymbol{C}_{\dot{\psi}}\acute{\mathbb{X}}
\end{aligned}
$$

Consider $\acute{\boldsymbol{x}} = (\acute{\mathbb{X}}^T, \acute{\mathbf{z}}_{\mathrm{y}}^T, \acute{z}_{\psi})^T$ as the new state vector of the system. The set of equations (4.3) is equivalent to

$$\dot{\acute{\boldsymbol{x}}} \;=\; \acute{\boldsymbol{A}}\acute{\boldsymbol{x}}$$

where the elements of $\acute{\boldsymbol{A}}$ are continuously differentiable functions of $\dot{\psi}_{\mathrm{d}} \in \Gamma = [0, a)$, where a is the maximum turn rate for the underwater glider. Suppose that $\acute{\boldsymbol{A}}$ is Hurwitz uniformly. This means the controller has been designed such that the closed-loop system is Hurwitz:

$$\mathrm{Re}[\lambda(\acute{\boldsymbol{A}})] \leq -\sigma < 0, \;\forall\; \dot{\psi}_{\mathrm{d}} \;\in\; \Gamma$$

Then, from Lemma 9.9 in [40], the Lyapunov equation

$$\mathbf{P}\acute{\boldsymbol{A}} + \acute{\boldsymbol{A}}^T\mathbf{P} = -\mathbb{I}.$$

has a unique positive definite solution $\mathbf{P}$ for every $\dot{\psi}_{\mathrm{d}} \in \Gamma$. $\mathbf{P}(\dot{\psi}_{\mathrm{d}})$ is continuously differentiable and satisfies

$$\begin{aligned} c_1\acute{\boldsymbol{x}}^T\acute{\boldsymbol{x}} \;\leq\; \acute{\boldsymbol{x}}^T\,\mathbf{P}(\dot{\psi}_{\mathrm{d}})\,\acute{\boldsymbol{x}} \;&\leq\; c_2\acute{\boldsymbol{x}}^T\acute{\boldsymbol{x}} \\ \|\frac{\partial}{\partial\dot{\psi}_{\mathrm{d}}}\mathbf{P}(\dot{\psi}_{\mathrm{d}})\| \;&\leq\; \vartheta \end{aligned}$$

for all $(\acute{\boldsymbol{x}}, \dot{\psi}_{\mathrm{d}}) \in \mathbb{R}^n \times \Gamma$, where c_1, c_2, and ϑ are positive constants independent of $\dot{\psi}_{\mathrm{d}}$. Consequently, the Lyapunov function $V(\acute{\boldsymbol{x}}, \dot{\psi}_{\mathrm{d}}) = \acute{\boldsymbol{x}}^T\,\mathbf{P}\,\acute{\boldsymbol{x}}$ satisfies the following inequalities

$$\begin{aligned} c_1\|\acute{\boldsymbol{x}}\|^2 \;\leq\; V(\acute{\boldsymbol{x}}, \dot{\psi}_{\mathrm{d}}) \;&\leq\; c_2\|\acute{\boldsymbol{x}}\|^2 \\ \|\frac{\partial V}{\partial\acute{\boldsymbol{x}}}\|g(\acute{\boldsymbol{x}}, \dot{\psi}_{\mathrm{d}}) \;&\leq\; -c_3\|\acute{\boldsymbol{x}}\|^2 \\ \|\frac{\partial V}{\partial\acute{\boldsymbol{x}}}\| \;&\leq\; c_4\|\acute{\boldsymbol{x}}\| \\ \|\frac{\partial V}{\partial\dot{\psi}_{\mathrm{d}}}\| \;&\leq\; c_5\|\acute{\boldsymbol{x}}\|^2 \end{aligned}$$

for all $\acute{\boldsymbol{x}} \in D = \{\acute{\boldsymbol{x}} \in \mathbb{R}^n | \|\acute{\boldsymbol{x}}\| < r\}$ and $\dot{\psi}_{\mathrm{d}} \in \Gamma = [0, a)$ where, once again, a is the maximum turn rate for the underwater glider. The positive constants in inequalities are: $c_1 = \lambda_{\min}(\mathbf{P})$, $c_2 = \lambda_{\max}(\mathbf{P})$, $c_3 = 1$, $c_4 = 2\lambda_{\max}(\mathbf{P})$, and $c_5 = 0$ (Lemma 9.9 in [40]). The solutions are

uniformly ultimately bounded with an ultimate bound proportional to ε, the upper bound of the turn acceleration. The upper bound of ε can be calculated from the following relation:

$$\| \ddot{\psi}_{\mathrm{d}}(t) \| \leq \varepsilon < \frac{c_1 c_3}{c_2} \times \frac{r}{r c_5 + c_4 L} \ , \quad \| \frac{\partial \mathbf{h}}{\partial \dot{\psi}_{\mathrm{d}}} \| \leq L. \tag{4.4}$$

The norm of the tracking error remains smaller than $k\varepsilon$ for some finite $k > 0$. Moreover, if $\ddot{\psi}_{\mathrm{d}}(t) \to 0$ as $t \to \infty$, the tracking error tends to zero by Theorem 9.3 in [40].

Solving the Lyapunov equation and calculating the eigenvalues of $\mathbf{P}$, one obtains the c_i, $i = 1, 2, \ldots, 5$ and an upper bound for ε, the limit for commanded turn accelerations. Applying the proposed motion control system to the *Slocum* model given in [26], and performing the analysis outlined above, one obtains the constants:

$$c_1 = \lambda_{\min}(\mathbf{P}) = -378.75, \quad c_2 = \lambda_{\max}(\mathbf{P}) = 979.82, \quad c_3 = 1, \quad c_4 = 2\lambda_{\max}(\mathbf{P}), \quad \text{and} \quad c_5 = 0,$$

which gives

$$|\ddot{\psi}_{\mathrm{d}}(t)| \leq \varepsilon < 2 \times 10^{-4} \frac{r}{L}.$$

This is a conservative upper bound for acceleration in turn rate reference commands. A relaxed bound could be obtained by applying similar analysis in the time varying setting. (See Theorems 7.4 and 7.8 in [41], for example.)

4.5 Simulation Results

A sophisticated glider model based on the *Slocum* model given in [26] was linearized about the following equilibrium flight condition, which corresponds to wings-level, descending flight:

$$V_0 = 0.77 \text{ m/s}, \quad \alpha_0 = 4.3^\circ, \quad \theta_0 = -8.4^\circ, \quad \gamma_0 = -12.7^\circ, \quad \text{and} \quad \tilde{m}_0 = 0.63 \text{ kg}.$$

The moving mass values are $m_{\mathrm{p_x}} = m_{\mathrm{p_y}} = 9$ kg. The servo-actuator parameter values are

$$\omega_{\mathrm{n_x}} = 20 \text{ rad/s}, \quad \zeta_{\mathrm{x}} = 0.001, \quad \omega_{\mathrm{r_x}} = 0.8 \text{ rad/s}, \quad \text{and} \quad \zeta_{\mathrm{r_x}} = 1$$

$$\omega_{\mathrm{n_y}} = 20 \text{ rad/s}, \quad \zeta_{\mathrm{y}} = 0.01, \quad \omega_{\mathrm{r_y}} = 0.8 \text{ rad/s}, \quad \text{and} \quad \zeta_{\mathrm{r_y}} = 1$$

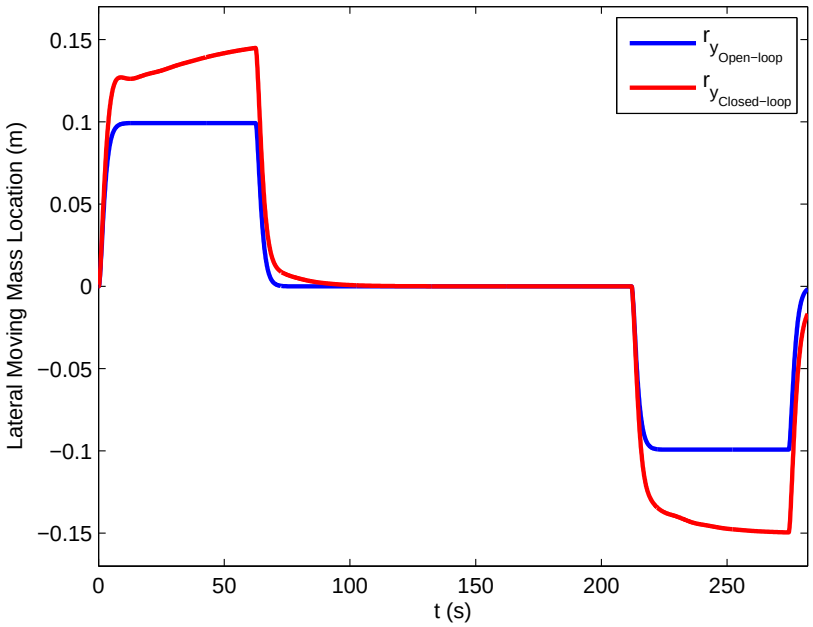

Figure 4.2 Lateral moving mass location (open- and closed-loop).

The PID control parameter values are

$$K_{p_\gamma} = -0.2 \text{ m}, \qquad T_{i_\gamma} = 2.3 \text{ s}, \qquad \text{and} \qquad T_{d_\gamma} = 2 \text{ s}$$

$$K_{p_{\dot\psi}} = 0.2 \text{ m/(rad/s)}, \qquad T_{i_{\dot\psi}} = 0.65 \text{ s}, \qquad \text{and} \qquad T_{d_{\dot\psi}} = 0.39 \text{ s}.$$

Figures 4.2 through 4.6 compare the results of simulations using open- and closed-loop control. Figure 4.2 shows the lateral mass location in response to a command sequence that is intended to effect a right turn, a straight segment, and a left turn (viewed from above) from an initial point to a desired final point. In the open-loop case, the moving mass is simply commanded to move to the (approximate) equilibrium value corresponding to a desired heading rate $\dot{\psi}_\text{d}$. In the closed-loop case, however, the heading rate is directly commanded, with the lateral moving mass actuator responding as necessary. The resulting path is depicted in Figure 4.3. It shows the result path when the vehicle performs the desired sequence in the open-loop case. The closed-loop path shows the effectiveness of the motion control system in compensating for the error from the approximation.

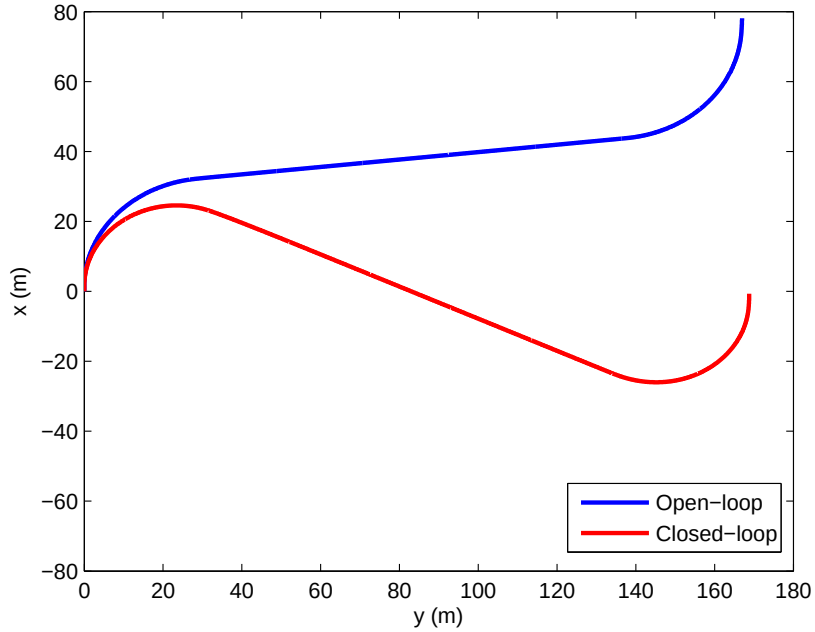

Figure 4.3 *Slocum* path in response to command sequence.

Figures 4.4 and 4.5 show desired, open-loop, and closed-loop values of the vehicle's glide path angle and turn rate. As expected, the deviation between the open-loop values and the desired values is significant. In Figure 4.5, the small spikes at the end of each segment correspond to reaction forces due to the movement of the lateral mass within the vehicle. We note that the turn rate magnitudes are of the same order as turn rates seen in glider operations. The *Slocum* glider, for example, can achieve a 20–30 m turn radius at speeds on the order of 0.5 m/s. A shallow-water variant of *Slocum*, which includes a movable rudder, can perform turns with a 7 m radius [13]. Figure 4.6 shows the location of the longitudinal moving mass, which regulates the glide path angle.

Remark 4.5.1 *The path in Figure 4.3 is reminiscent of a Dubins path, although the vehicle and actuator dynamics are included here. Time-optimal paths for a Dubins car with acceleration limits are discussed in [42] and [43], where it is recognized that extremal paths comprise sequences of straight, clothoidal, and circular segments. We call these "suboptimal Dubins paths."*

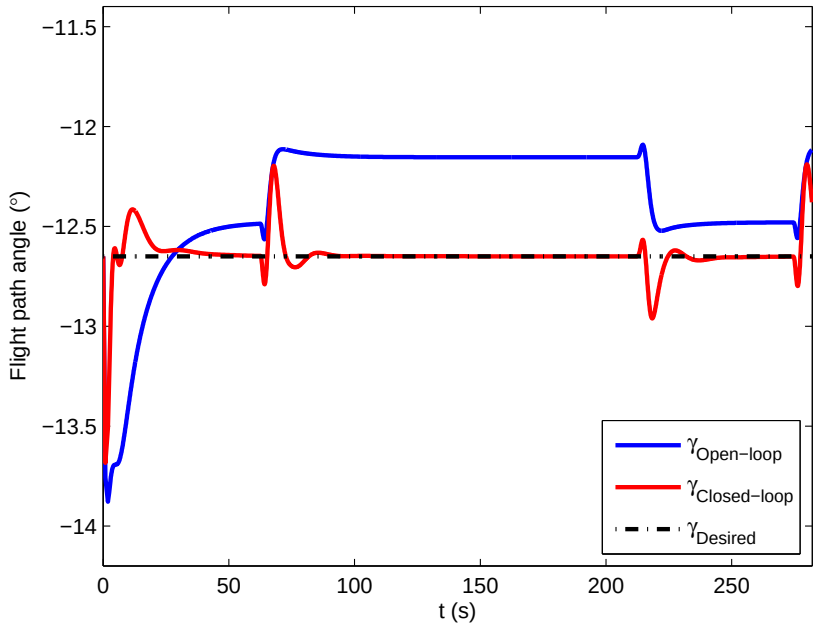

Figure 4.4 Glide path angle response to command sequence.

It must be stressed that the final guidance loop has not been closed, at this point. That is, we have not presented a control law to make the vehicle track a commanded *path*, such as a suboptimal Dubins path. Rather, we have presented the underlying motion control system over which a guidance loop might be imposed.

Figures 4.7 through 4.9 compare results of the simulation for the common feedback motion control system and the feedforward/feedback motion control system presented in this work. Figure 4.7 shows that the steady-motion based feedforward/feedback system reaches the desired turn rate much faster. Hence, the vehicle reaches the desired final point at the turn rate and flight path angle in shorter time (Figure 4.9). Figure 4.8 illustrates the effectiveness of both control loops in maintaining a constant flight path angle. The result illustrates that adding the feedforward term and starting at a near hyperbolic equilibria gives the vehicle the ability to perform tighter turns. The designed motion control system opens a new perspective to the use of the intrinsic efficiency of these buoyancy-driven gliders.

In closing, we note that the feedforward component of the proposed control system, as

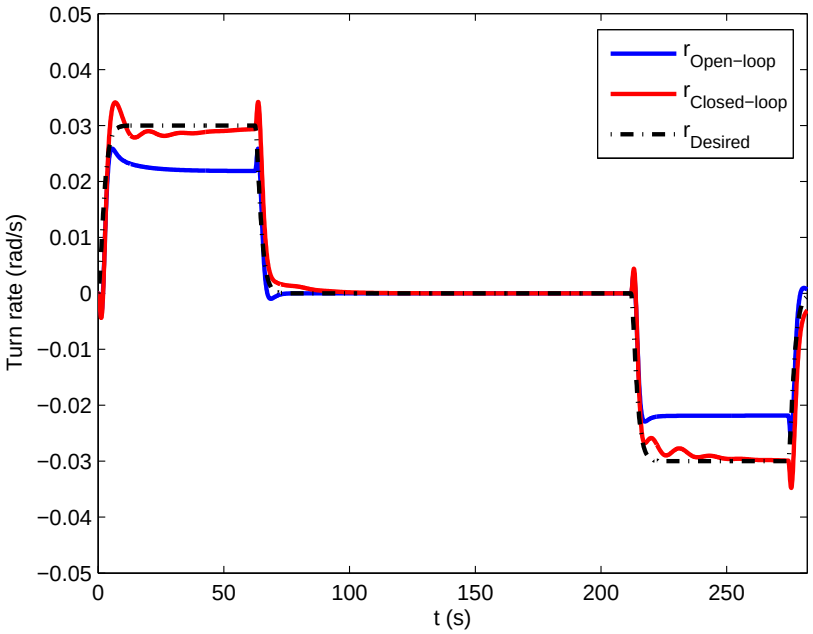

Figure 4.5 Turn rate response to command sequence.

presented, relies on the analytical solution for the steady turning motions of an underwater glider. This analysis is based on a sophisticated model of the underwater glider dynamics. In the absence of such a model, and the corresponding solution for steady motions, one may instead use a look-up table which maps vehicle configurations to stable, steady motions. Although such a table would have to be developed through an exhaustive series of experimental sea trials, the approach may, in some cases, be more expedient than developing a complete dynamic model.

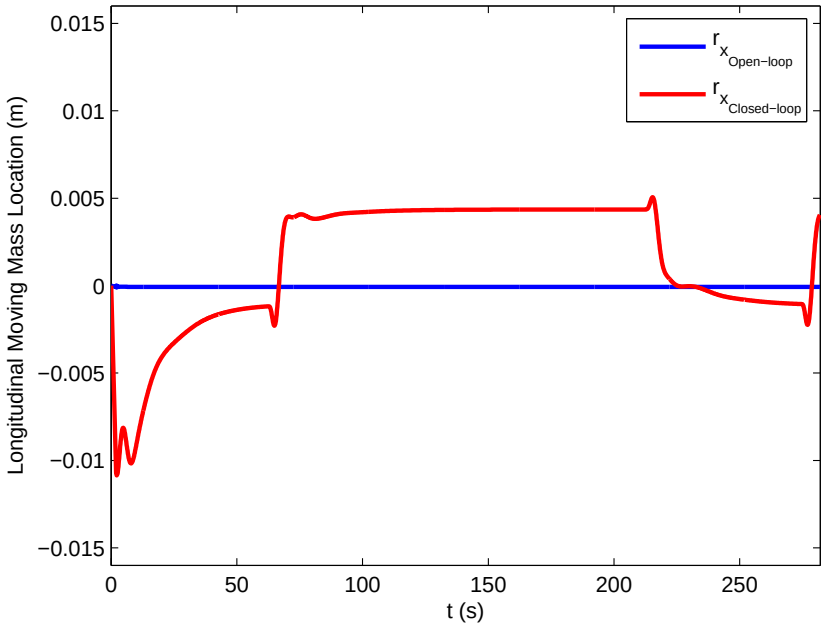

Figure 4.6 Variation in longitudinal moving mass position from nominal.

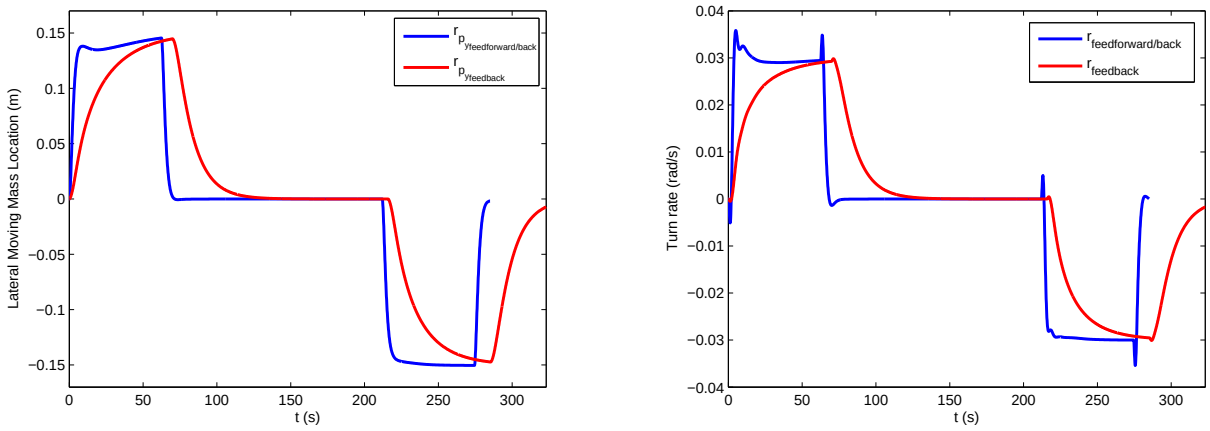

Figure 4.7 Lateral moving mass position and turn rate.

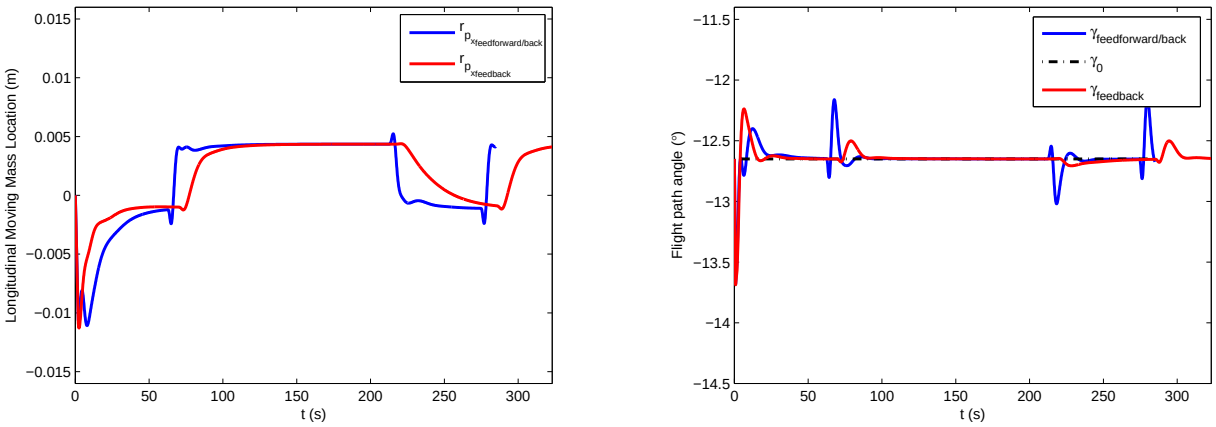

Figure 4.8 Longitudinal moving mass position and flight path angle.

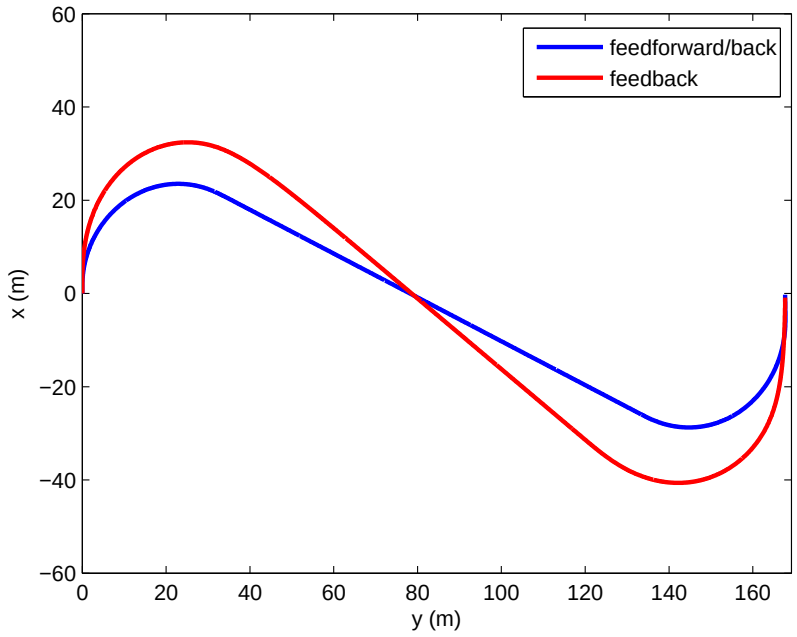

Figure 4.9 *Slocum* path in response to feedback and feedforward/feedback compensator.

Chapter 5

An Illustrative Example

Inspired by the problem of motion control for an underwater glider, we develop and analyze stability of a feedforward/feedback controller for a simple dynamical system that exhibits a saddle-node bifurcation. In analogy with the underwater glider problem, the stable manifold of the dynamical system is approximated in the neighborhood of a particular equilibrium, to first order in the bifurcation parameter, using regular perturbation theory. The control objective is to track a slowly varying desired state which corresponds, at any instant, to an equilibrium state of the system, i.e., a point on the (true) stable manifold. To meet this objective, a feedforward term commands a value of the perturbation parameter that corresponds, to first order in the perturbation parameter, to the desired equilibrium state. A proportional-integral feedback term then compensates for the error due to the approximation. Stability of the closed-loop system is examined using slowly varying systems theory. The example was first presented at the 2009 Spring Southeastern Meeting of the American Mathematical Society [44].

5.1 Problem Definition

Consider the nonlinear system

$$\dot{x} = (1+\epsilon) - x^2 \tag{5.1}$$

where ϵ is a small parameter. The system (5.1) equilibria are:

$$x_{eq} \in \{\pm\sqrt{1+\epsilon}\}.$$

When $\epsilon < -1$ there are no equilibrium points. When $\epsilon = -1$, there is a saddle-node point. When $\epsilon > -1$ there are two equilibrium points: that is, one saddle point and one node (either an attractor or a repellor).

Suppose, however, that we were unable to compute these equilibria exactly. Since ϵ is a small parameter, one may develop an approximation for the equilibria by assuming a series expansion for x in ϵ as follows:

$$x = x_0 + \epsilon x_1 + \epsilon^2 x_2$$

Substituting into the right-hand side of the dynamic equation, collecting like powers of ϵ and setting the coefficients equal to zero gives:

$$\begin{aligned} 0 &= (1+\epsilon) - x^2 \\ &= (1 - x_0^2) + \epsilon(1 - 2x_0x_1) - \dots \end{aligned}$$

- Setting the coefficient of ϵ^0 to zero gives $x_0 \in \{\pm 1\}$, which is the zeroth order equilibrium value.
- Setting the coefficient of ϵ^1 to zero gives, $x_1 = \frac{1}{2x_0}$.

Thus, we find that, to first order in ϵ,

$$\tilde{x}_{eq} = x_0 + \epsilon x_1 = x_0 + \epsilon\frac{1}{2x_0} \in \{1 + \frac{\epsilon}{2}, -1 - \frac{\epsilon}{2}\}.$$

Figure 5.1 shows the difference between the true and approximate equilibrium parameterized

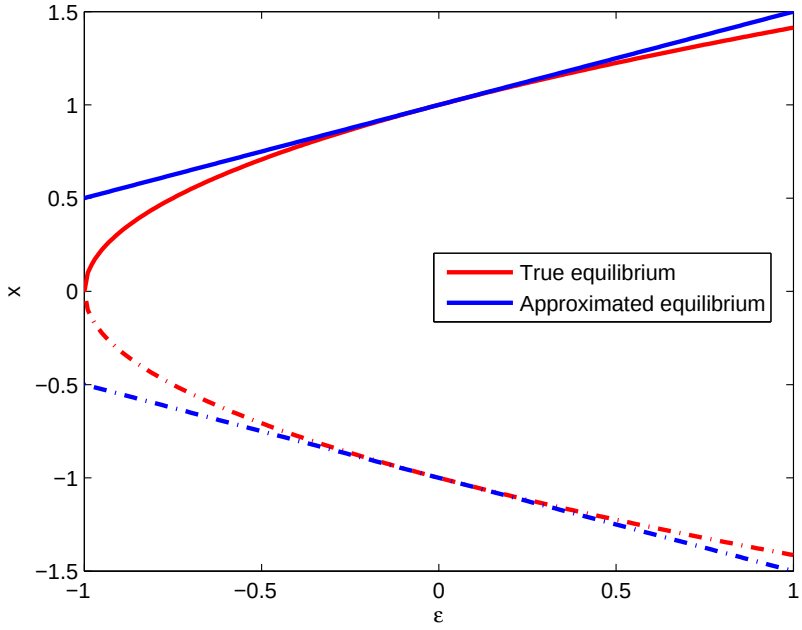

Figure 5.1 True and approximate equilibrium parameterized by ϵ.

by ϵ. Now suppose that ϵ may be modulated to drive the system along the stable equilibrium manifold. Consider, for example, the equilibrium $x_{eq} = \sqrt{1+\epsilon}$, which is approximated to first order in ϵ as $\tilde{x}_{eq} = 1 + \frac{\epsilon}{2}$.

5.2 Stability Near Hyperbolic Equilibria

To assess stability of the true, neighboring equilibria, one may linearize about the *approximate* equilibrium condition and compute the eigenvalues. Linearizing (5.1) about $\tilde{x}_{eq} = 1 + \frac{\epsilon}{2}$ gives

$$\dot{\tilde{x}} = -\tilde{x}. \tag{5.2}$$

So the system has a real negative eigenvalue of $\tilde{\lambda} = -1$. For this simple example, we can linearize (5.1) about the true equilibrium condition $x_{eq} = \sqrt{1+\epsilon}$

$$\dot{x} = (1 + \epsilon - 2\sqrt{1+\epsilon})x \tag{5.3}$$

and calculate the eigenvalue of the system, which is $\lambda = 1 + \epsilon - 2\sqrt{1+\epsilon}$. Recognizing that the eigenvalue of the system depends continuously on its parameter (ϵ), the question is, when can the stability of the true equilibrium be inferred from stability of the approximate equilibrium?

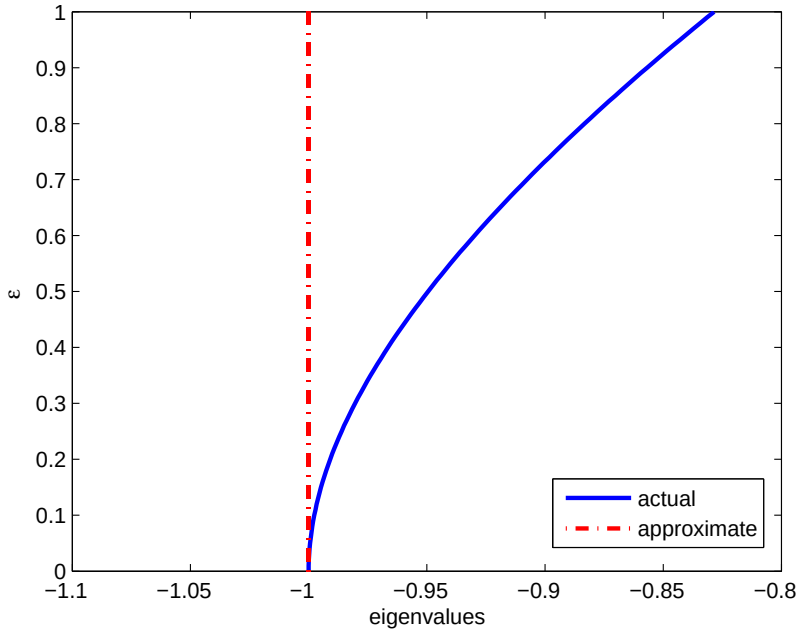

Figure 5.2 True and approximate eigenvalues parameterized by $0 < \epsilon < 1$.

From Chapter 9 of Hartman [38], the behavior of solutions of a smooth autonomous system near a stationary point can, in some cases, be determined by comparing solutions of a linear system

$$\dot{x} = Ax \tag{5.4}$$

and solutions of a perturbed system

$$\dot{x} = Ax + \epsilon f(x) \tag{5.5}$$

where $f(x)$ is of class C^1 for small $\|x\|$ and where

$$f(0) = 0,\ \partial_x f(0) = 0 \tag{5.6}$$

where ∂_x is the Jacobian matrix of f with respect to x.

Let $x_t = \eta(t, x_0)$ be the solution of (5.5) satisfying the initial condition $\eta(0, x_0) = x_0$. For fixed t, consider $x_t = \eta(t, x_0)$ as a map $T^t : x_0 \to x_t$ of a neighborhood D_t of $x = 0$ in the x-space into a neighborhood of $x = 0$ in the same space. The map T^t is defined on the set D_t of points x_0 for which the solution $\eta(t, x_0)$ is defined on a t-interval containing 0 and t. A set S in the x-space which is invariant with respect to the family of maps T^t will be called invariant with respect to (5.5). S is invariant with respect to (5.5) if and only if it has the property that $x_0 \in S$ implies that $\eta(t, x_0) \in S$ for all t on the maximal interval of existence of the solution $\eta(t, x_0)$.

From Theorem 6.1. from Chapter 9 of [38], in the differential equation

$$\dot{x} = Ax + \epsilon f(x) \tag{5.7}$$

let $f(x)$ be of class C^1 and $f(0) = 0, \quad \partial_x f(0) = 0$. Let the constant matrix A possess $d(> 0)$ eigenvalues having negative real parts, say, d_i eigenvalues with real parts equal to α_i, where $\alpha_1 < \ldots < \alpha_r < 0$ and $d_1 + \ldots + d_r = d$, whereas the other eigenvalues, if any, have non-negative real parts. If $0 < \epsilon < -\alpha_r$, then (5.7) has solutions $x = x(t) \neq 0$ satisfying

$$\|x(t)\| e^{\epsilon t} \to 0 \text{ as } t \to \infty \tag{5.8}$$

and any such solution satisfies

$$\lim t^{-1} \log \|x(t)\| = \alpha_i \quad \text{for some} \quad i. \tag{5.9}$$

Furthermore, for sufficiently small $\epsilon > 0$, the point $x = 0$ and the set of points x on solutions $x(t)$ satisfying $\lim t^{-1} \log \|x(t)\| \leq \alpha_i$ for a fixed i as $t \to \infty$ constitute a locally invariant C^1 manifold S_i [or S_r] of dimension $d_1 + \ldots + d_i$ [or $d_1 + \ldots + d_r = d$].

In the differential equation

$$\dot{x} = Ax + \epsilon f(x) \tag{5.10}$$

suppose that no eigenvalue of A has a vanishing real part. Assume there is a C^1 change of variables $R : x \to \tilde{x}$ with non-vanishing Jacobian in a neighborhood of $x = 0$ which transforms (5.10) into the linear system

$$\dot{\tilde{x}} = A\tilde{x} \tag{5.11}$$

in a neighborhood of $\tilde{x} = 0$.

From Theorem 7.1. from Chapter 9 of [38], suppose that no eigenvalue of A has a vanishing real part and that $f(x)$ is of class C^1 for small $\|x\|$, $f(0) = 0$, $\partial_x f(0) = 0$. Let $T^t : x_t = \eta(t, x_0)$ and $L^t : \tilde{x}_t = e^{At}\tilde{x}_0$ be the general solution of (5.10) and (5.11), respectively. Then exists a continuous one-to-one map of a neighborhood if $x = 0$ onto a neighborhood of $\tilde{x} = 0$ such that $RT^tR^{-1} = L^t$; in particular, $R : x \to \tilde{x}$ maps solutions of (5.10) near $x = 0$ onto solutions of (5.11) preserving parametrizations.

Thus, the topological structure of the set of solutions of (5.10) in a neighborhood of $x = 0$ is identical with that of the solutions of (5.11) near $\tilde{x} = 0$.

Based on Theorem 6.1. from Chapter 9 of [38], since system (5.2) has one negative real eigenvalue equal to -1, if $0 < \epsilon < 1$, then system (5.3) has a unique fixed point with invariant manifolds of the same dimension as system (5.2). Furthermore, based on Theorem 7.1. from Chapter 9 of [38], if ϵ remains small with respect to the magnitude of the real part of the eigenvalue of the system (5.2) ($0 < \epsilon \leq 0.1$), then there exists a continuous one-to-one map of a neighborhood if $\tilde{x} = 1$ onto a neighborhood of $x = 1$. Thus, the topological structure of the set of solutions of (5.2) in a neighborhood of $\tilde{x} = 1$ is identical with that of the solution of (5.3) near $x = 1$. Figures 5.3 and 5.2 illustrate the change of eigenvalue of system (5.2) and (5.3) as ϵ varies. Hence, in general, the stability of the true equilibrium can be inferred from stability of the neighboring approximate equilibrium provided that (i) the equilibrium is hyperbolic and (ii) ϵ is small relative to the magnitude of the real part of every eigenvalue.

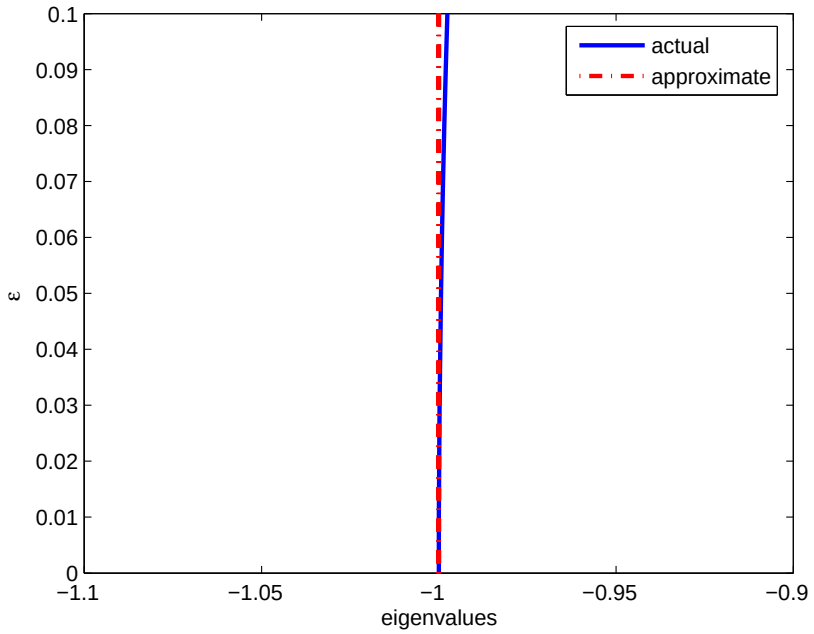

Figure 5.3 True and approximate eigenvalues parameterized by $0 < \epsilon \leq 0.1$.

5.3 Feedforward/Feedback Controller Design

Now, suppose that the dynamical system is augmented as follows

$$\begin{aligned} \dot{x} &= 1 + \epsilon - x^2 \\ \dot{\epsilon} &= u_\epsilon \end{aligned} \tag{5.12}$$

It is required that the output of the system tracks a slowly varying reference input x_d. The following three steps are necessary to design the controller:

1. Servo-controller for ϵ

   Choose an input u such that parameter ϵ asymptotically tracks a desired trajectory ϵ_{ref}

   $$u_\epsilon = -\frac{1}{\tau}(\epsilon - \epsilon_{\text{ref}}) \text{ with } \tau > 0,$$

   where parameter τ can be chosen to give the desired convergence properties. Then $\tau\dot{\epsilon} = -\epsilon + \epsilon_{\text{ref}}$.

2. Feedback compensator for tracking error

   Consider $e = x_d - x$ where $x_d \in C'$ is slow varying. Define $\dot{z} = e = x_d - x$ to integrate error. Define a PI controller:

$$u = K_p e + K_i z = K_p(x_d - x) + K_i z.$$

3. Feedforward/feedback controller (ϵ_{ref})

   The corresponding equilibrium value of $\tilde{\epsilon}_d$ to desired input, as predicted by perturbation analysis (feedforward) is augmented with feedback compensation to compensate for approximation error.

$$\begin{aligned} \epsilon_{\text{ref}} &= \tilde{\epsilon}_d + (K_p e + K_i z) \\ &= 2(x_d - 1) + [K_p(x_d - x) + K_i z] \end{aligned}$$

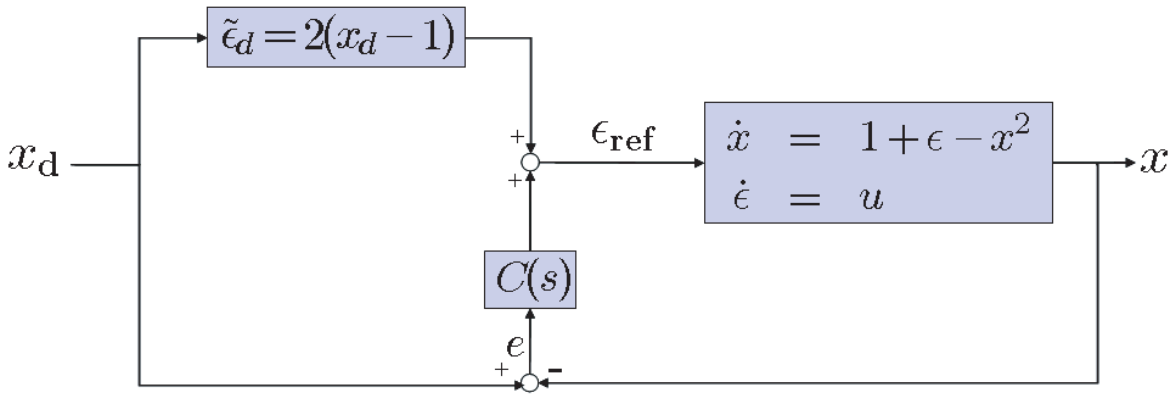

Figure 5.4 Control loop.

The complete control system is shown in Figure 5.4. The complete closed-loop dynamics can be obtained by substituting the controller:

$$\begin{aligned} \dot{x} &= 1 + \epsilon - x^2 \\ \tau\dot{\epsilon} &= -\epsilon + 2(x_d - 1) + [K_p(x_d - x) + K_i z] \\ \dot{z} &= x_d - x \end{aligned}$$

Rearranging the equations gives:

$$\begin{pmatrix} \dot{x} \\ \dot{\epsilon} \\ \dot{z} \end{pmatrix} = \begin{pmatrix} 1+\epsilon-x^2 \\ -\frac{1}{\tau}\epsilon + \frac{1}{\tau}(-2-K_p x + K_i z)) \\ -x \end{pmatrix} + \begin{pmatrix} 0 \\ \frac{1}{\tau}(2+K_p) \\ 1 \end{pmatrix} x_d. \tag{5.13}$$

5.4 Stability Analysis of Closed-Loop System

The output of the nonlinear system (5.13) is required to track the slowly varying reference input $x_d(t)$, a continuously differentiable signal whose time derivative satisfies $\|\dot{x}_d(t)\| \leq \varepsilon$ for all time, for some small value ε. To analyze this system following [40], define $\boldsymbol{x} = (x, \epsilon, z)^T$ and consider x_d as a "frozen" parameter. Assume that for each fixed value of x_d the frozen system has an isolated equilibrium point defined by:

$$\tilde{\mathbf{h}}(x_d) = \boldsymbol{x}_{\text{eq}} = \begin{pmatrix} \tilde{x}_{\text{eq}} \\ \tilde{\epsilon}_{\text{eq}} \\ z_{eq} \end{pmatrix} = \begin{pmatrix} x_d \\ 2(x_d-1) \\ 0 \end{pmatrix}.$$

Note that $\|\frac{\partial \tilde{\mathbf{h}}}{\partial x_d}\| \leq L$ for some positive scalar L.

We linearize the nonlinear system (5.13) about $\tilde{\mathbf{h}}(x_d)$ and make the change of variables $\acute{\boldsymbol{x}} = \boldsymbol{x} - \tilde{\mathbf{h}}(x_d)$ to shift the frozen equilibrium point to origin, so that we may analyze stability.

$$\begin{pmatrix} \dot{\acute{x}} \\ \dot{\acute{\epsilon}} \\ \dot{\acute{z}} \end{pmatrix} = \underbrace{\begin{pmatrix} -2x_d & 1 & 0 \\ -\frac{K_p}{\tau} & -\frac{1}{\tau} & \frac{K_i}{\tau} \\ -1 & 0 & 0 \end{pmatrix}}_{\tilde{\mathbf{h}}(x_d)} \begin{pmatrix} \acute{x} \\ \acute{\epsilon} \\ \acute{z} \end{pmatrix} = \underbrace{\begin{pmatrix} \alpha & \beta & 0 \\ -\frac{K_p}{\tau} & -\frac{1}{\tau} & \frac{K_i}{\tau} \\ -1 & 0 & 0 \end{pmatrix}}_{\acute{\boldsymbol{A}}} \begin{pmatrix} \acute{x} \\ \acute{\epsilon} \\ \acute{z} \end{pmatrix}. \tag{5.14}$$

Consider the Lyapunov function

$$V(\acute{\boldsymbol{x}}, x_d) = \acute{\boldsymbol{x}}^T \mathbf{P} \acute{\boldsymbol{x}}$$

where $\mathbf{P}$ is the solution of the Lyapunov equation

$$\mathbf{P}\acute{\boldsymbol{A}} + \acute{\boldsymbol{A}}^T \mathbf{P} = -\mathbb{I}. \tag{5.15}$$

Based on Theorem 9.3. of Khalil [40], if there is a positive definite and decrescent Lyapunov function $V(\acute{\boldsymbol{x}}, x_d)$ that has a negative definite derivative along the trajectories of the system and that satisfies certain inequalities to handle the perturbation and the fact that $x_d(t)$ is not constant, the solution will be uniformly ultimately bounded within a ball around the equilibrium point. If $\dot{x}_d(t) \to 0$ as $t \to \infty$, then the tracking error tends to zero. In fact, the function V given above does satisfy the required inequalities:

$$\begin{aligned} c_1\|\acute{\boldsymbol{x}}\|^2 \;\leq\; V(\acute{\boldsymbol{x}}, x_d) \;\leq\; c_2\|\acute{\boldsymbol{x}}\|^2 \\ \|\frac{\partial V}{\partial \acute{\boldsymbol{x}}}\|g(\acute{\boldsymbol{x}}, x_{\mathrm{d}}) \;\leq\; -c_3\|\acute{\boldsymbol{x}}\|^2 \\ \|\frac{\partial V}{\partial \acute{\boldsymbol{x}}}\| \;\leq\; c_4\|\acute{\boldsymbol{x}}\| \\ \|\frac{\partial V}{\partial x_d}\| \;\leq\; c_5\|\acute{\boldsymbol{x}}\|^2, \end{aligned}$$

for all $\acute{\boldsymbol{x}} \in D = \{\acute{\boldsymbol{x}} \in \mathbb{R}^n | \|\acute{\boldsymbol{x}}\| < r\}$ and $x_d \in \Gamma$, where $c_1 = \lambda_{\min}(\mathbf{P})$, $c_2 = \lambda_{\max}(\mathbf{P})$, $c_3 = 1$, $c_4 = 2\lambda_{\max}(\mathbf{P})$, and $c_5 = 0$. The solutions are uniformly ultimately bounded with an ultimate bound proportional to ε, the upper bound on $\dot{x}_{\mathrm{d}}$. An upper bound for ε, which provides guidance for how one may choose the reference trajectory, may be computed from the following relation:

$$\| \dot{x}_{\mathrm{d}}(t) \| \leq \varepsilon < \frac{c_1 c_3}{c_2} \times \frac{r}{r c_5 + c_4 L} \;, \quad \|\frac{\partial h}{\partial x_d}\| \leq L. \tag{5.16}$$

Substituting the matrices

$$\acute{A} = \begin{pmatrix} \alpha & \beta & 0 \\ -\frac{K_p}{\tau} & -\frac{1}{\tau} & \frac{K_i}{\tau} \\ -1 & 0 & 0 \end{pmatrix} \;, \quad \mathbf{P} = \begin{pmatrix} P_{11} & P_{12} & P_{13} \\ P_{12} & P_{22} & P_{23} \\ P_{13} & P_{23} & P_{33} \end{pmatrix}$$

into the Lyapunov equation gives the left side of equation (5.15) as:

$$\begin{pmatrix} 2(\alpha P_{11} - P_{13} - \frac{K_p}{\tau}P_{12}) & \beta P_{11} + (\alpha - \frac{1}{\tau})P_{12} - \frac{K_p}{\tau}P_{22} - P_{23} & \alpha P_{13} + \frac{K_i}{\tau}P_{12} - \frac{K_p}{\tau}P_{23} - P_{33} \\ & 2(\beta P_{12} - \frac{1}{\tau}P_{22}) & \beta P_{13} + \frac{K_i}{\tau}P_{22} - \frac{1}{\tau}P_{23} \\ & & 2\frac{K_i}{\tau}P_{23} \end{pmatrix},$$

where $\alpha = -2x_d$ and $\beta = 1$. Solving the Lyapunov equation and calculating the eigenvalues of $\mathbf{P}$, one obtains the constants c_i for $i = 1, 2, \ldots, 5$. From these, the upper bound for ε, and thus the ultimate bound on solutions, may computed. For completeness, we include the solution for the components of $\mathbf{P}$ below.

$$\begin{aligned}
P_{23} &= -\frac{\tau}{2K_i} \\
P_{22} &= \frac{\tau}{2K_i}\frac{\tau\beta(-\alpha\tau + K_i\beta) + \alpha K_i(\alpha\tau - 1) + \beta(\tau + K_pK_i)}{(\alpha - K_p\beta)(\alpha\tau - 1) - K_i\tau\beta} \\
&= \frac{\tau}{2K_i}\frac{\tau(2x_d\tau + K_i) - 2x_dK_i(-2x_d\tau - 1) + (\tau + K_pK_i)}{(-2x_d - K_p)(-2x_d\tau - 1) - K_i\tau} \\
P_{12} &= \frac{1}{\beta}(\frac{1}{\tau}P_{22} - \frac{1}{2}) = (\frac{1}{\tau}P_{22} - \frac{1}{2}) \\
P_{13} &= -\frac{1}{\beta}(\frac{K_i}{\tau}P_{22} + \frac{1}{2K_i}) = -(\frac{K_i}{\tau}P_{22} + \frac{1}{2K_i}) \\
P_{11} &= \frac{1}{\alpha}(\frac{-1}{2} + P_{13} + \frac{K_p}{\tau}P_{12}) = -\frac{1}{2x_d}(\frac{-1}{2} + P_{13} + \frac{K_p}{\tau}P_{12}) \\
P_{33} &= \alpha P_{13} + \frac{K_i}{\tau}P_{12} + \frac{K_p}{2K_i} = -2x_dP_{13} + \frac{K_i}{\tau}P_{12} + \frac{K_p}{2K_i}
\end{aligned} \tag{5.17}$$

5.5 Simulation Results

Numeric simulation would help to better understand the process explained in previous sections (5.3 and 5.4). To design the PI controller, consider the nonlinear dynamic system (5.12) in the form

$$\begin{aligned}
\dot{x} &= 1 + \epsilon - x^2 \\
\dot{\epsilon} &= -\frac{1}{\tau}(\epsilon - \tilde{\epsilon_d}) + \frac{1}{\tau}u.
\end{aligned}$$

Linearizing the system about the approximate equilibrium gives

$$\begin{pmatrix} \dot{x} \\ \dot{\epsilon} \end{pmatrix} = \begin{pmatrix} \alpha & \beta \\ 0 & -1/\tau \end{pmatrix} \begin{pmatrix} x \\ \epsilon \end{pmatrix} + \begin{pmatrix} 0 \\ 1/\tau \end{pmatrix} u$$
$$y = \begin{pmatrix} 1 & 0 \end{pmatrix} \begin{pmatrix} x \\ \epsilon \end{pmatrix}.$$

The system transfer function is

$$\begin{aligned} G(s) &= \mathbf{C}(s\mathbb{I} - \mathbf{A})^{-1}B \\ &= \begin{pmatrix} 1 & 0 \end{pmatrix} \begin{pmatrix} s-\alpha & -\beta \\ 0 & s+1/\tau \end{pmatrix}^{-1} \begin{pmatrix} 0 \\ 1/\tau \end{pmatrix} \\ &= \frac{\frac{\beta}{\tau}}{(s-\alpha)(s+\frac{1}{\tau})} \end{aligned}$$

where $\alpha = -2x_d$ and $\beta = 1$. Let $G_c(s)$ represent the PI controller

$$G_c(s) = K_p + \frac{K_i}{s} \quad \text{where} \quad K_i = K_p/T_i.$$

The closed-loop transfer function is

$$\frac{C(s)}{R(s)} = \frac{\frac{\beta}{\tau}(K_p + \frac{K_i}{s})}{(s-\alpha)(s+\frac{1}{\tau}) + \frac{\beta}{\tau}(K_p + \frac{K_i}{s})}.$$

We obtain experimentally the response of the system to a unit-step input. Setting $x_d = 1$, hence $\alpha = -2$ and $\beta = 1$, and considering $\tau = 1$, Figure 5.5 illustrates that the response to a step input exhibits an S-shaped curve. The step response in Figure 5.5 can be characterized by the delay time $L = 0.25$ and the time constant $T = 2.5$. From these values the controller gain can be calculated as $K_p = 0.9\frac{T}{L} = 9.0$, $T_i = \frac{L}{0.3} = 0.83$, and $K_i = \frac{K_p}{T_i} = 10.8$ using the Ziegler-Nichols tuning rule based on the step response of the plant. Figure 5.6 shows the closed-loop response to a step input.

The next step is tuning the controller for the nonlinear system. Further tuning suggests that the gains need to be relaxed to maximum of $K_i = 3$ and $K_p = T_i K_i = 2.49$.

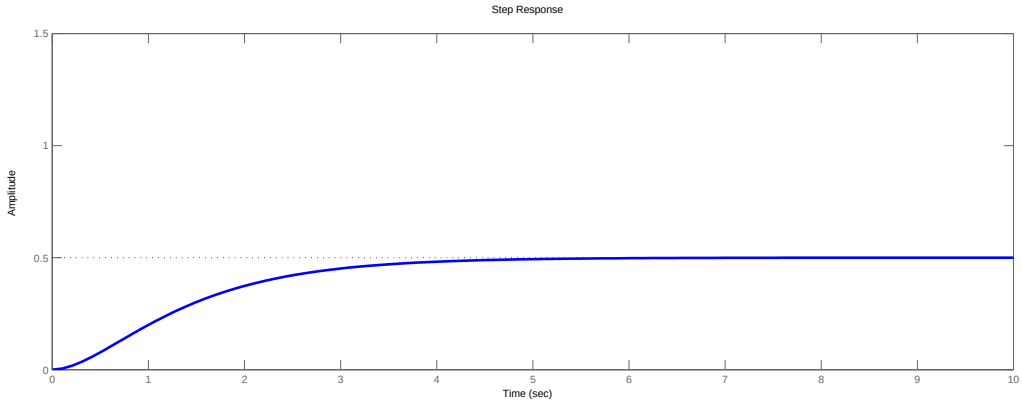

Figure 5.5 Open-loop response to step input.

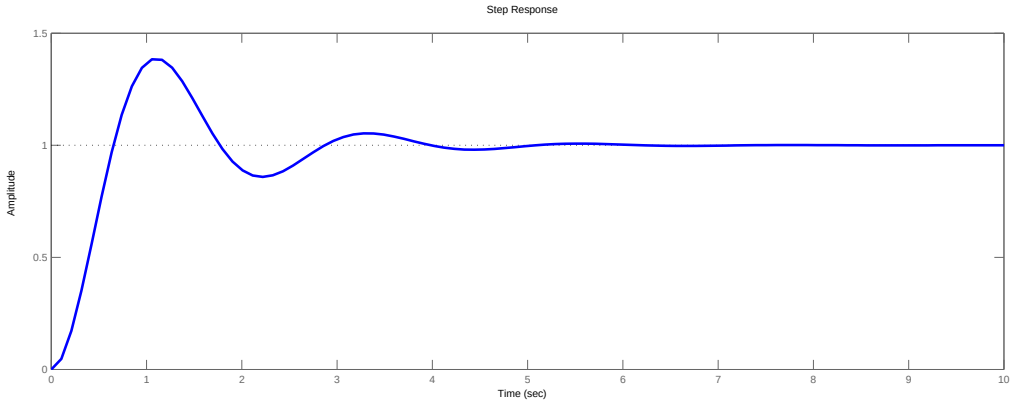

Figure 5.6 Closed-loop response to step input.

From Section 5.4 remember that the solutions are uniformly ultimately bounded, with an ultimate bound proportional to ε. The upper bound of ε can be calculated from (5.16) based on calculated $c_1, \ldots, c_5$ coefficients.

When $x_d = 1$ the true and approximate equilibrium are equal, and the solution of the Lyapunov equation is

$$\mathbf{P} = \begin{pmatrix} 1.084 & 0.001 & -1.670 \\ 0.001 & 0.501 & -0.167 \\ -1.670 & -0.167 & 3.757 \end{pmatrix}$$

and the eigenvalues are $\lambda(\mathbf{P}) = \{0.26, 0.52, 4.57\}$, hence $c_1 = \lambda_{min}(\mathbf{P}) = 0.26$, $c_2 =$

$\lambda_{max}(\mathbf{P}) = 4.57$, $c_3 = 1$, $c_4 = 2\lambda_{max}(\mathbf{P}) = 9.14$, and $c_5 = 0$. The result for coefficients show that the upper bound for the ε will decrease with the increase of convergence time (τ).

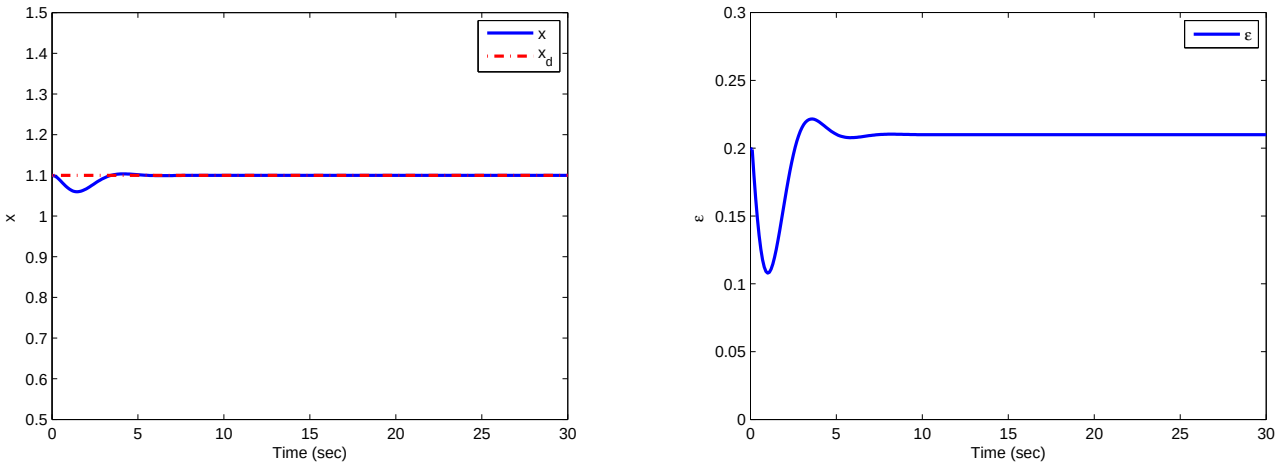

Figure 5.7 Tracking response of the system $\tau = 1$ and $x_d = 1.1$.

Figure 5.7 shows the tracking result when $x_d = 1.1$. The figure on the left illustrates the resulting trajectory (x) for the closed-loop system. The figure on the right shows the parameter value ϵ, which must change in order to regulate the trajectory. Figure 5.8 illustrates the tracking result of the designed controller when $x = 1.4$. In this case, the solution of the Lyapunov equation is

$$\mathbf{P} = \begin{pmatrix} 0.738 & -0.053 & -1.507 \\ -0.053 & 0.447 & -0.167 \\ -1.507 & -0.167 & 4.625 \end{pmatrix}.$$

The eigenvalues are $\lambda(\mathbf{P}) = \{0.18, 0.48, 5.15\}$, hence $c_1 = 0.18$, $c_2 = 5.15$, $c_3 = 1$, $c_4 = 10.30$, and $c_5 = 0$. Increasing $\tau = 1$ to $\tau = 10$, Figure 5.9 shows the effectiveness of the designed controller when $x_d = 1.4$. For this case, when $x_d = 1$, the solution of the Lyapunov equation

is

$$\mathbf{P} = \begin{pmatrix} 1.727 & 0.468 & -3.071 \\ 0.468 & 9.682 & -1.667 \\ -3.071 & -1.667 & 6.698 \end{pmatrix}.$$

The eigenvalues are $\lambda(\mathbf{P}) = \{0.25, 7.06, 10.80\}$. These values show a decrease in the upper limit of ε when increasing the τ value.

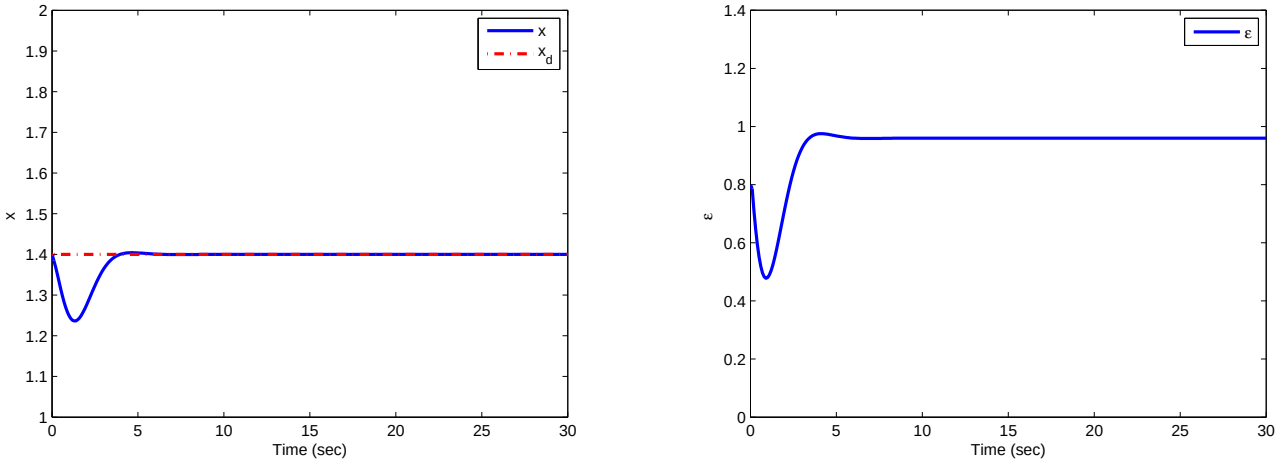

Figure 5.8 Tracking response of the system $\tau = 1$, and $x_d = 1.4$.

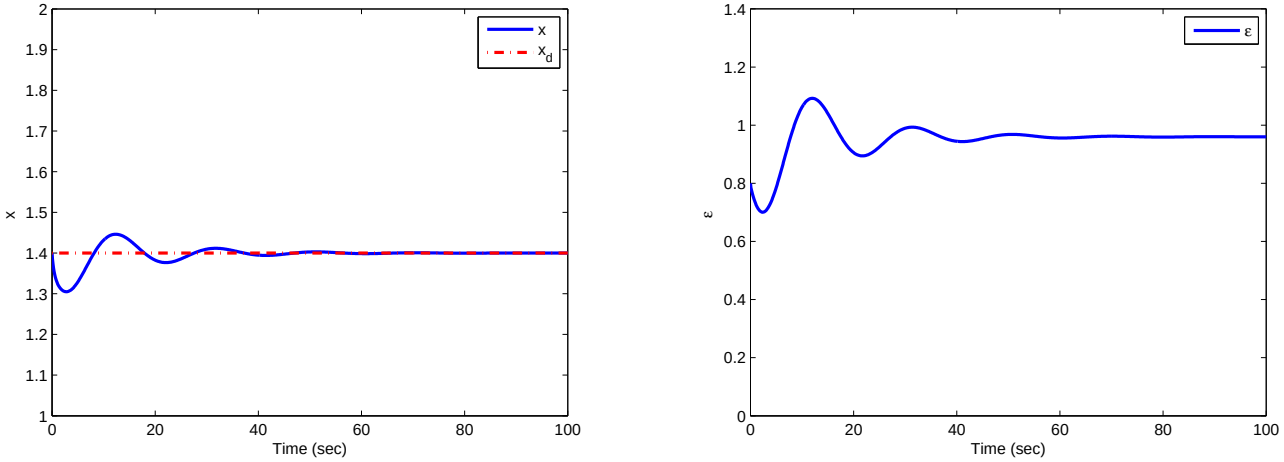

Figure 5.9 Tracking response of the system $\tau = 10$, and $x_d = 1.4$.

Here, we simultaneously proved the stability of the closed loop system and found the

upper bound of reference input rate ($\dot{x}_d$) represented by ε. Comparing the results for the coefficients obtained for the three cases of $x_d = 1, 1.1,$ and 1.4 shows that the upper bound for the ε will decrease with the increase in x_d. Moreover, the upper limit of ε will decrease when increasing the τ value. These results show that the upper bound of reference input rate (ε) should be calculated for the largest desired input through design.

Chapter 6

Guidance

The next step is to implement general guidance strategies, such as a line-of-sight strategy to track energy-optimal paths generated in real time. Figure 6.1 illustrates the complete underwater glider guidance and control system.

As mentioned earlier, the gliders behavior in the horizontal plane is reminiscent of kinematic

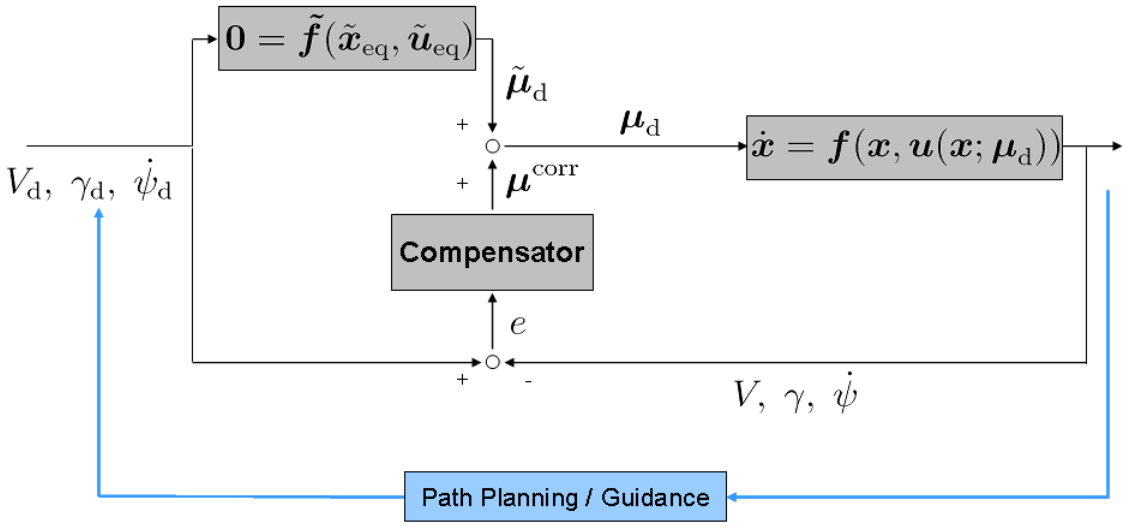

Figure 6.1 Complete guidance control system.

cars (nonholonomic mobile robots). A variety of existing guidance, control, and coordination algorithms can be directly applied, like such as Dubins' paths when there is no current and

"convected" Dubins' paths in the presence of uniform currents ([45] and [46]). These Dubins-like paths accommodate turn rate and turn acceleration limits, which are essential aspects of underwater glider motion. For underwater gliders travelling at constant speed and maximum flight efficiency, minimum arclength paths are minimum energy paths. Hence, energy-efficient paths can be obtained by generating sequences of steady wings-level and turning motions. This chapter illustrates tracking a Dubins path and the coordinated flight of two underwater gliders [47].

6.1 Path Planning

A logical next step is to develop a procedure for optimal path planning which makes use of the preceding approximate results for equilibrium turning flight. A reasonable objective would be to concatenate these approximate equilibrium motions in order to minimize the time of transit from a given initial point to a given final point with a specified initial and final heading. The question of reachability naturally arises, since an underwater glider must ascend or descend to locomote. A glider cannot progress between two points at the same depth, for example, without concatenating at least one ascending and one descending motion. For the moment, we will restrict our attention to situations in which the final point is strictly below (or above) the initial point and can be reached in a single descending (or ascending) flight without exceeding the vehicle's physical limitations (such as the minimum glide slope). More precisely, we will project the vehicle path onto the horizontal plane and simply ignore the vertical component of motion. A fortunate consequence of the structure of our approximate solution for turning flight is that, to first-order in ϵ, the horizontal and vertical components of velocity remain constant. Thus, the minimum time problem in the horizontal plane corresponds to minimizing the *change in depth* for a given horizontal point-to-point transition. Since an underwater glider propels itself by the force of gravity, minimizing the change in depth is equivalent to minimizing the energy expenditure.

To see that the horizontal component of velocity remains constant, to first order in ϵ, recall that the speed V remains constant to first order in ϵ and note that

$$\begin{aligned}
\dot{z} &= \boldsymbol{e}_3^T \boldsymbol{\mathcal{R}}_{\mathrm{IB}}(\phi,\theta,\psi)\boldsymbol{\mathcal{R}}_{\mathrm{BC}}(\alpha,\beta)\,(V\boldsymbol{e}_1) \\
&= \boldsymbol{e}_3^T \left(e^{\widehat{\boldsymbol{e}_3}\psi} e^{\widehat{\boldsymbol{e}_2}\theta} e^{\widehat{\boldsymbol{e}_1}\phi}\right)\left(e^{-\widehat{\boldsymbol{e}_2}\alpha} e^{\widehat{\boldsymbol{e}_3}\beta}\right)(V\boldsymbol{e}_1) \\
&= \boldsymbol{e}_3^T \left(e^{\widehat{\boldsymbol{e}_2}(\theta_0)} e^{\widehat{\boldsymbol{e}_1}(\epsilon\phi_1+O(\epsilon^2))}\right)\left(e^{-\widehat{\boldsymbol{e}_2}(\alpha_0+O(\epsilon^2))} e^{\widehat{\boldsymbol{e}_3}(\epsilon\beta_1+O(\epsilon^2))}\right)\left((V_0+O(\epsilon^2))\boldsymbol{e}_1\right) \\
&= -V_0 \sin(\theta_0-\alpha_0) + O(\epsilon^2).
\end{aligned}$$

Of course, $-V_0 \sin(\theta_0 - \alpha_0)$ is precisely the vertical component of velocity in unperturbed, wings level flight. An important consequence of this observation is that, since both the magnitude and the vertical component of velocity remain constant, to first order in ϵ, so does the horizontal component of velocity. Projecting the vehicle's motion onto the horizontal plane, glider equilibrium motions correspond to constant-speed straight-line and circular paths. The speed is determined solely by the vehicle net weight and, in practice, may be assumed to take the maximum achievable value. Considering only motion in the horizontal plane, the control problem reduces to the following: *choose the turn rate to minimize the time of transit from a given initial point to a given final point with a specified initial and final heading.*

6.1.1 Dubins' Car

Viewing the glider motion from directly above, the minimum time control problem is reminiscent of Dubins' car [45], a planar vehicle which drives forward at constant speed and which may turn, in either direction, at any rate up to some maximum value. Dubins showed that the minimum time control policy which brings the car from a given point to another, with specified initial and final directions, is a concatenation of three motions: a left or right turn at maximum rate, a straight transit or a second turn at maximum rate, and a final turn at maximum rate. Note that a constant speed turn at maximum turn rate corresponds to a turn of minimum radius. (Actually, Dubins considered the problem in terms of minimizing

the length of a continuous curve with limits on the curvature, but the two problems are equivalent.) Variations of Dubins' problem have enjoyed renewed attention in recent years, in part because of increasing interest in mobile robotics. Reeds and Shepp [48] characterized the family of optimal trajectories for a variation of Dubins' car in which the vehicle could move in reverse, as well as forward. Sussmann and Tang [49] generalized further by "convexifying" the non-convex control set defined in [48], managing to sharpen the results presented by Reeds and Shepp and by Dubins. Parallel studies, as outlined in a series of INRIA technical reports and papers [50–53], also investigated controllability and optimal path planning for Dubins and Reeds-Shepp mobile robots. Anisi's thesis [3] reviews some of the recent results and provides some historical context.

For the purpose of explaining the Dubins' car problem, let $\boldsymbol{x} = [x, y, \psi]^T$ represent the vehicle's state (i.e., its position and heading in the horizontal plane) and let the turn rate $u = r$ be the input, which satisfies the inequality constraint $|r| \leq |r_{\max}|$. The vehicle moves at some constant, nonzero forward speed V. Then the equations of motion are

$$\dot{\boldsymbol{x}} = \boldsymbol{f}(\boldsymbol{x}, u) \qquad \text{where} \qquad \boldsymbol{f}(\boldsymbol{x}, u) = \begin{pmatrix} V\cos\psi \\ V\sin\psi \\ u \end{pmatrix}. \tag{6.1}$$

Although Dubins' problem was originally presented as one of minimizing the arclength of a continuously differentiable curve, it may be re-stated as follows: Find an input history which brings the system from a specified initial state $\boldsymbol{x}(0) = \boldsymbol{x}_0$ to a specified final state $\boldsymbol{x}(t_f) = \boldsymbol{x}_f$ while minimizing $t_f > 0$. Note that, since the speed is constant, this minimum time problem is equivalent to Dubins' minimum arclength problem.

As shown in [45], the optimal history contains at most three distinct segments (i.e., two switches of the control among its three possible values). These results are sharpened in [49], where the control histories are shown to be of the type "BSB" (for "bang-singular-bang") or "BBB" (for "bang-bang-bang"). Having characterized the family of candidate optimal input histories, it remains to actually choose the best one for a given initial and final state.

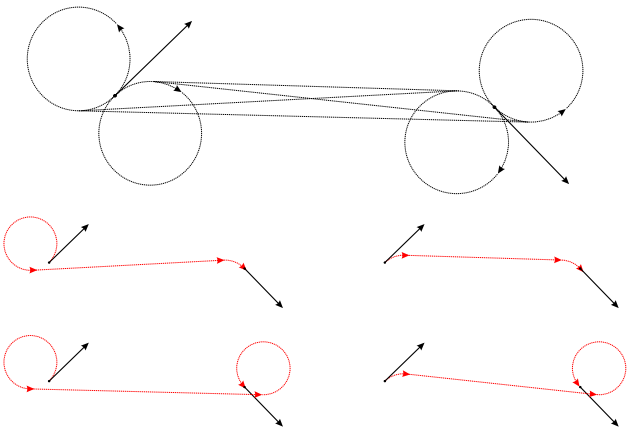

Figure 6.2 A geometric method for selecting the time-optimal path for Dubins' car when the endpoints are more than twice the minimum turn radius apart [3].

Considering, for example, the case where the intermediate transit is a straight path that is much longer than the vehicle turn radius, a simple, geometric algorithm as illustrated in Figure 6.2 provides the optimal path. One defines two oriented circles of minimum radius that are tangent to the initial velocity vector and two more oriented circles of minimum radius that are tangent to the final velocity vector. Connecting the circles by directed tangents that are consistent with the sense of the circles yields four admissible paths. Because the vehicle moves at constant speed, the path of minimum arclength is the minimum time path.

To apply the approach described here to an underwater glider, assume that the glider is executing some nominal gliding motion at a given glide slope and speed. Given an initial heading, a desired final heading may be attained, at least approximately, by solving the Dubins' problem for the horizontal projected motion. Recall that the minimum time problem in the horizontal plane corresponds to minimizing the change in depth, which equates to minimizing the propulsive energy expenditure. This is an appealing feature of Dubins' paths, given that underwater gliders are specifically designed for propulsive efficiency.

6.1.2 Dubins' Car with Control Rate Limits

The classical Dubins' car problem assumes that turn rate can be treated as an input with magnitude limits but no rate limits. (Equivalently, the arclength minimization problem

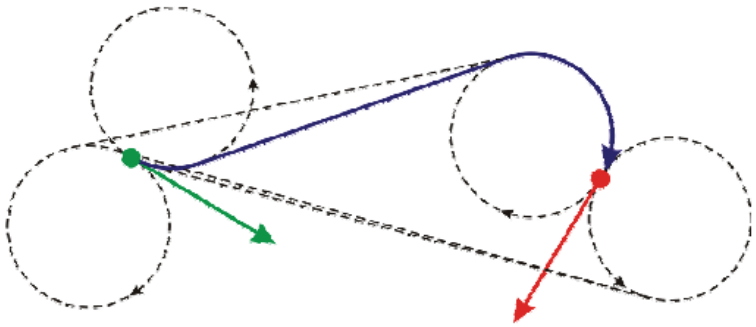

Figure 6.3 Dubins' paths: Constant speed; no current.

imposes limits on the curvature but not on its derivative.) The assumption may or may not be appropriate for wheeled robotic vehicles, but it is certainly not appropriate for underwater gliders. For these vehicles, turn rate is controlled indirectly by shifting the center of gravity to effect a banked turn. To explore the effect of control rate limits on the Dubins optimal path result, one may augment the state vector given in Section 6.1.1 as follows: $\boldsymbol{x} = [x, y, \psi, r]^T$. Let the turn *acceleration* be the input $u = \dot{r}$, where r satisfies the *state* inequality constraint $|r| \leq |r_{\max}|$ and u satisfies the *input* inequality constraint $|u| \leq |u_{\max}|$. The equations of motion are

$$\dot{\boldsymbol{x}} = \boldsymbol{f}(\boldsymbol{x}, u) \qquad \text{where} \qquad \boldsymbol{f}(\boldsymbol{x}, u) = \begin{pmatrix} V\cos\psi \\ V\sin\psi \\ r \\ u \end{pmatrix}.$$

Although we now consider turn acceleration as an input, we still assume that the underwater glider state varies in a quasi-steady manner. That is, we assume that the vehicle state varies along the continuum of (approximate) equilibrium states, as parameterized by the turn rate. Under this assumption, as shown in Section 3.2, the vehicle's speed V remains constant to first-order in the turn rate.

In fact, this problem has been treated in some detail by Scheuer [54], as summarized in

[43]. Her work extends that of Boissonnat and colleagues [55] and of Kostov and Degtiariova-Kostova [56], who considered the case where the derivative of the turn rate (equivalently, the derivative of curvature) is constrained, but not the magnitude of the turn rate. In [55], it was shown that time-optimal paths exist and that they consist of straight segments and clothoids at maximum turn acceleration. It was also shown that the minimum time curves can be quite complicated, possibly including infinitely many clothoidal segments. Independently, Kostov and Degtiariova-Kostova [56] proposed a method for constructing suboptimal paths from clothoids and straight segments. The term "suboptimal," as used in [56], means that the amount by which the transit time exceeds the minimum time is bounded by a function of the turn acceleration limit.

6.1.3 Dubins' Car in the Presence of Currents

Ocean currents can also significantly influence a glider's motion, even at depth. Because underwater gliders move quite slowly, relative to conventional AUVs, and operate over much longer time spans, even light currents can have a large, cumulative effect on vehicle motion. The Dubins path planning procedure has recently been extended to the case of a constant ambient current in [46, 57]. In the approach described in these papers, the Dubins path is planned relative to the (moving) ambient fluid with suitably re-defined endpoint conditions. In [46], authors provide a geometric method for generating candidate time-optimal paths in steady wind by concatenating straight and trochoidal segments (see Figure 6.4). With wind approaching from the west in Figure 6.4, there are two candidate extremals, shown by blue curves, corresponding to trochoidal segments with clockwise and counter-clockwise orientations, respectively. The path with shorter arc length is the one with shorter total time requirement.

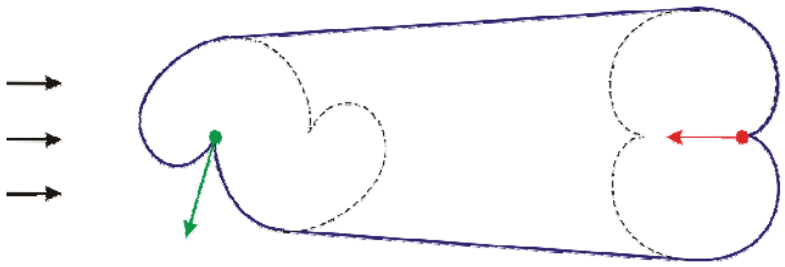

Figure 6.4 Convected Dubins paths: Constant speed; uniform current.

6.2 Guidance Strategies

The goal here is to present examples of guidance strategies which use the previously developed motion control system to make underwater gliders fly in a desired pattern. The desired pattern is mission specific. We present two cases. First, we consider the energy-efficient paths discussed in Section 6.1. Second, we consider the problem of forcing two or more gliders to follow the same ground track at different depths. In Section 6.2.1 we describe a trajectory tracking approach in the horizontal plane that has been described in [58]. In Section 6.2.2 we describe a method for planar collective motion described in [59]. In both cases, the authors assumed a kinematic car model. Here, we consider the actual dynamics of the underwater glider and seek a desired turn rate $\dot{\psi}_{\mathrm{d}}$ as in Figure 6.1.

6.2.1 Planar Trajectory Tracking

The aim is to drive the vehicle along a desired path with constant speed. We assume that we have prior knowledge of the vehicle's mission path and the path can be constructed of line segments or segments with a constant curvature, such as Dubins' paths. The path following controller should eliminate both cross-track error (the distance from the vehicle to the path) and heading error (the angle between the vehicle velocity and the tangent to the path) [60]. This motivates the development of the vehicle kinematic model in terms of path parameters

in a Serret-Frenet frame and the use of the cross track and heading error as coordinates of the error space where the control problem will be formulated.

Following [58], consider a frame F_s along the desired path, with its x-axis in the direction of the desired inertial velocity, i.e., tangential to the path, and its y-axis normal to the path. Let s be the arclength along the desired path. With s indicating a position on the path, the curvature $\kappa(s)$ at that position is defined as $\kappa(s) = 1/R(s)$, where $R(s)$ is the radius of the path at that point. If the direction of the path is indicated as ψ_s then the path parameters are related to yaw-rate as $\dot{\psi}_s(s) = \kappa(s)\dot{s}$,

$$\begin{pmatrix} \dot{s} \\ \dot{y}_s \\ \dot{\tilde{\psi}} \end{pmatrix} = \begin{pmatrix} \frac{\cos(\tilde{\psi})}{1-\kappa y_s} & 0 \\ \sin\tilde{\psi} & 0 \\ -\kappa\frac{\cos(\tilde{\psi})}{1-\kappa y_s} & 1 \end{pmatrix} \begin{pmatrix} V_0 \\ \dot{\psi}_d \end{pmatrix}$$

where $\tilde{\psi} = \psi_d - \psi_s$, which is the difference between desired path and the vehicle's heading. The guidance objective is to force $\tilde{\psi}$ and y_s simultaneously to zero. This may be achieved by constructing the commanded control signal ($\tilde{\psi}_c(y_s)$) as a function of "cross-track error" y_s. A common logic is a pursuit-guidance law,

$$\tilde{\psi}_c(y_s) = -\arctan(\frac{y_s}{d})$$

where d is a constant "look-ahead" distance. Or the Helmsman logic can be used

$$\tilde{\psi}_c = \tilde{\psi}_{icpt}\frac{(e^{-\frac{a}{2}y_s} - 1)}{(e^{-\frac{a}{2}y_s} + 1)}$$

$$\dot{\tilde{\psi}}_c = -a\tilde{\psi}_{icpt}\frac{e^{-\frac{a}{2}y_s}}{(e^{-\frac{a}{2}y_s} + 1)^2}V_0\sin(\tilde{\psi}),$$

where a is Helmsman sensitivity parameter and $\tilde{\psi}_{icpt}$ is the intercept heading [58].

The desired turn rate can be obtained from

$$\dot{\tilde{\psi}}_d = -k_d\dot{\tilde{\psi}} + k_{d_0}(\dot{\tilde{\psi}}_c - \dot{\tilde{\psi}}) + k_p(\tilde{\psi}_c - \tilde{\psi}) + \nu_k.$$

One must choose k_d, k_{d_0}, and k_p properly. A kinematics feedforward term $\nu_k = \kappa V_0$ replaces the need for integral action for constant-curvature path following.

Figures 6.6–6.10 illustrate the effectiveness of the described guidance method, together with the motion control system developed in Chapter 4, when a *Slocum* glider tracks a Dubins path.

6.2.2 Coordination on Helical Paths

In many environmental sampling problems, it is important to characterize the flux (direction and magnitude) through a control volume boundary. Underwater gliders can follow a helical path and collect ocean data in the desired control volume. Multiple gliders, working in coordination, can enable or enhance this capability. For example, one application would be measuring the flux of energy through sea-floor hydrothermal vents. This is important to determine the nature of hydrothermal systems, as well as their role in the oceans and, more generally, the Earth's ecosystem [61]. Underwater gliders can measure the ocean's vertical temperature independently while flying in coordination at different depths. This is necessary to account for the fact that turbulent mixing does not occur uniformly over the entire ocean [7].

Following the algorithm presented in [59], we consider each glider moving in constant speed V_0 subject to steering control u_k. Choosing the control law for glider $k \in \{1, \ldots, N\}$,

$$u_k = u_{k_1} + u_{k_2},$$

enforces motion of all gliders in the same direction in synchronization, where u_{k_1} guarantees the convergence on the circle and u_{k_2} gives the desired phase arrangement. For parallel formation on a cylinder with radius R_0, they are defined as

$$u_{k_1} = -\frac{K_c}{N} \sum_{j=1}^{N} \sin(\psi_j - \psi_k)$$

$$u_{k_2} = \omega_0 (1 + \kappa_c R_0 V_0 \cos(\psi_k - \vartheta_k))$$

where $\vartheta_k = \arctan(\frac{y_k}{x_k})$. One can choose control gains K_c and κ_c properly. Then, the desired turn rate can be obtained from $\dot{\psi}_{k_d} = u_k$.

Figures 6.11–6.15 illustrate the effectiveness of this guidance method, together with the motion control system developed in Chapter 4, when two *Slocum* gliders fly in coordination on a helical path.

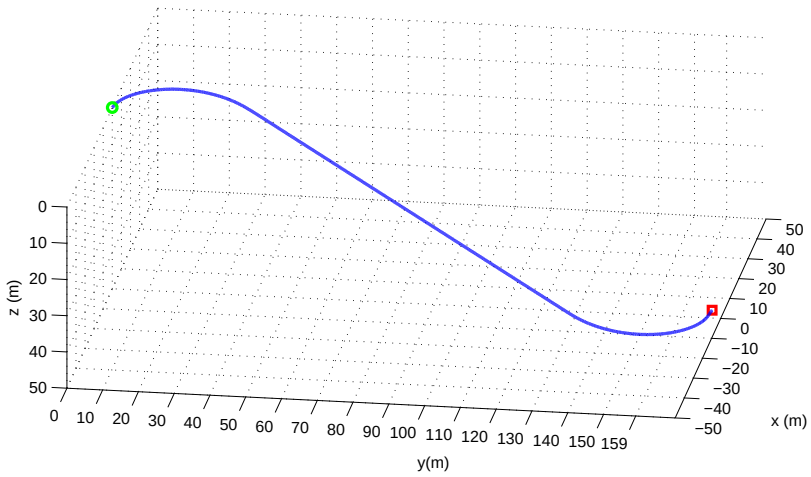

Figure 6.5 *Slocum* trajectory in 3D following a Dubins path.

6.3 Simulation Results

We present simulation results for two cases: first a *Slocum* tracks a commanded Dubins path, and then two *Slocum* gliders perform coordinated flight on a helical path. We consider the flight condition and PID control parameters presented in Section 4.5 to obtain the results.

Figure 6.5 shows the result of planar path following of *Slocum* in 3D, considering the following values for the servo-actuator parameters

$$\omega_{n_x} = 20 \text{ rad/s}, \quad \zeta_x = 0.001, \quad \text{and} \quad \zeta_{r_x} = 1$$
$$\omega_{n_y} = 20 \text{ rad/s}, \quad \zeta_y = 0.01, \quad \text{and} \quad \zeta_{r_y} = 1$$

with $\omega_{r_x} = \omega_{r_y} = 1$ rad/s, which means we are not considering the actuators' rate limit in this case. The guidance law parameters are $a = 2$, $\tilde{\psi}_{icpt} = \pi/4$, $k_p = 10$, $k_d = 1$, $k_{d_0} = 0$, and $\nu_k = 0$. Figure 6.6 illustrates the effectiveness of the guidance control system in following a

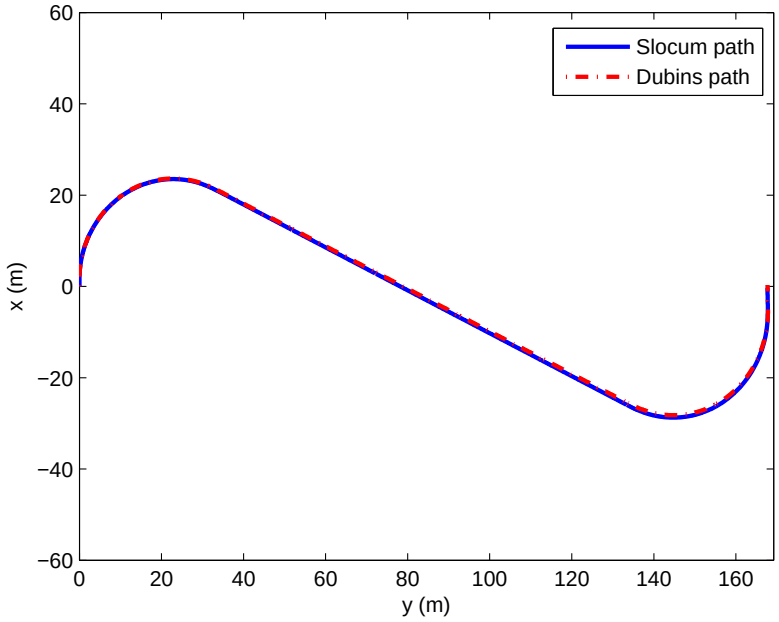

Figure 6.6 *Slocum* following a Dubins path.

desired Dubins path. Figure 6.7 shows the lateral mass location in response to a command sequence that is intended to effect a right turn, a straight segment, and left turn (viewed from above) from an initial point to a desired final point. The heading rate $\dot{\psi}_{\mathrm{d}}$ is directly commanded as shown in Figure 6.8, with the lateral moving mass actuator responding as necessary. Figure 6.9 illustrates the location of the longitudinal moving mass, which must move in order to regulate the glide path angle shown in Figure 6.10.

Figure 6.11 illustrates glide synchronization of two *Slocum* gliders on a helical path, where Glider 1 starts at $(x_1(0), y_1(0), z_1(0)) = (5, 5, 25)$ and Glider 2 starts at $(x_2(0), y_2(0), z_2(0)) = (-5, -5, 0)$. For this case, we consider $\omega_{\mathrm{r_x}} = \omega_{\mathrm{r_y}} = 0.8$ rad/s for both gliders. The guidance parameters are $K_c = -0.01$ and $\kappa_c = 0.04$.

Figure 6.12 shows the variation of the position of the lateral moving mass of two gliders while coordinating to achieve the desired turn rate. Figure 6.13 illustrates time history of turn rate to reach 0.025 rad/s and perform a synchronized flight on a circle with radius of 27.5 m. The time history of the position of the longitudinal moving mass of the two gliders

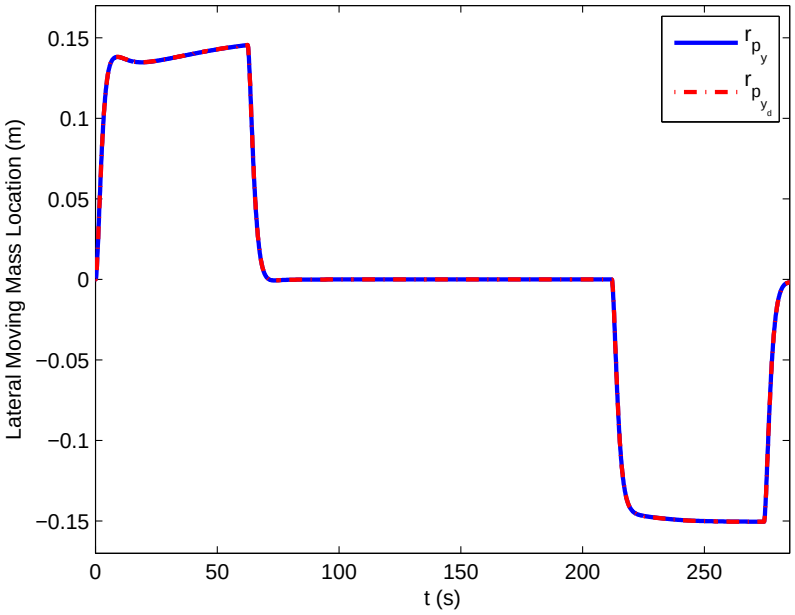

Figure 6.7 Lateral moving mass location.

to maintain the nominal flight path angle is shown in Figure 6.14. See Figure 6.15 for the time history of the flight path angle.

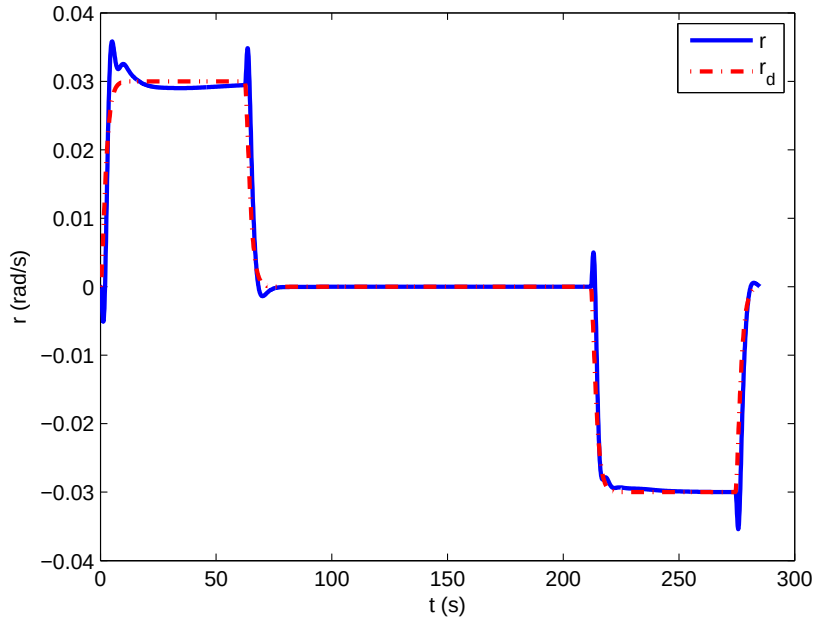

Figure 6.8 Turn rate response following Dubins' path.

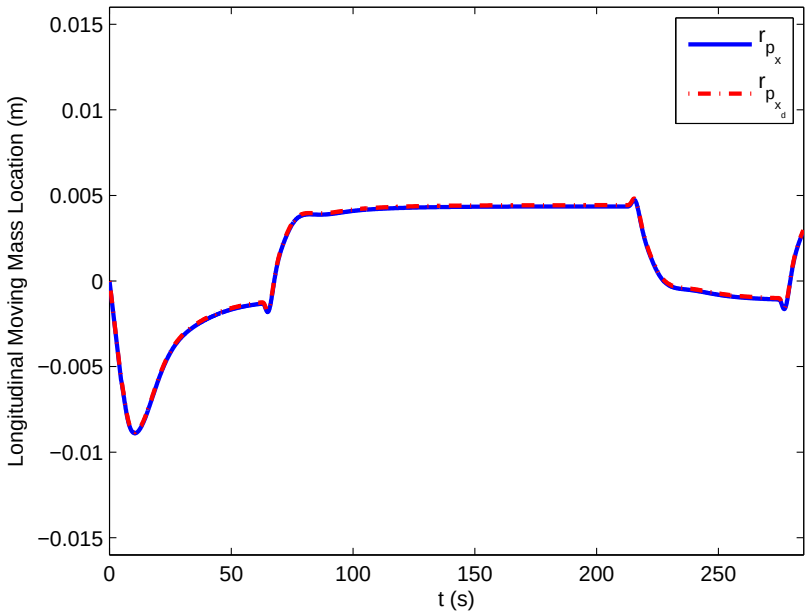

Figure 6.9 Longitudinal moving mass position.

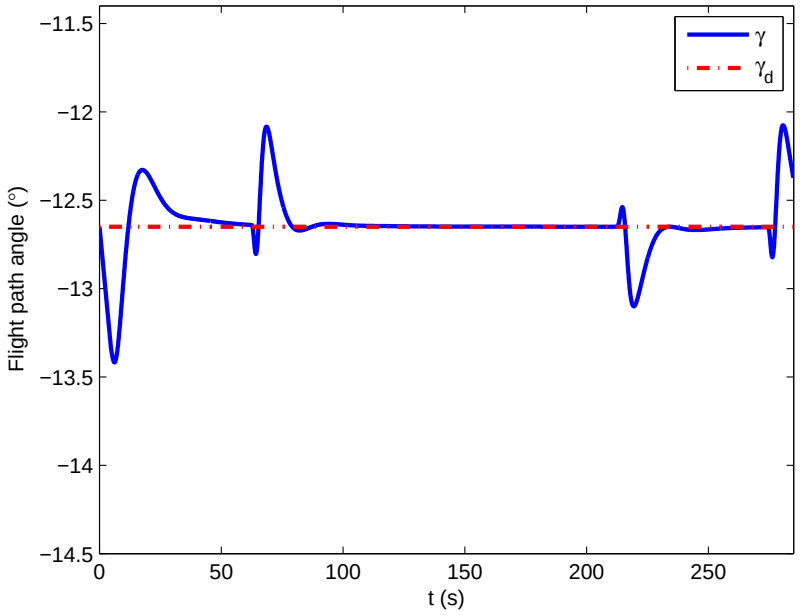

Figure 6.10 Glide path angle response following Dubins' path.

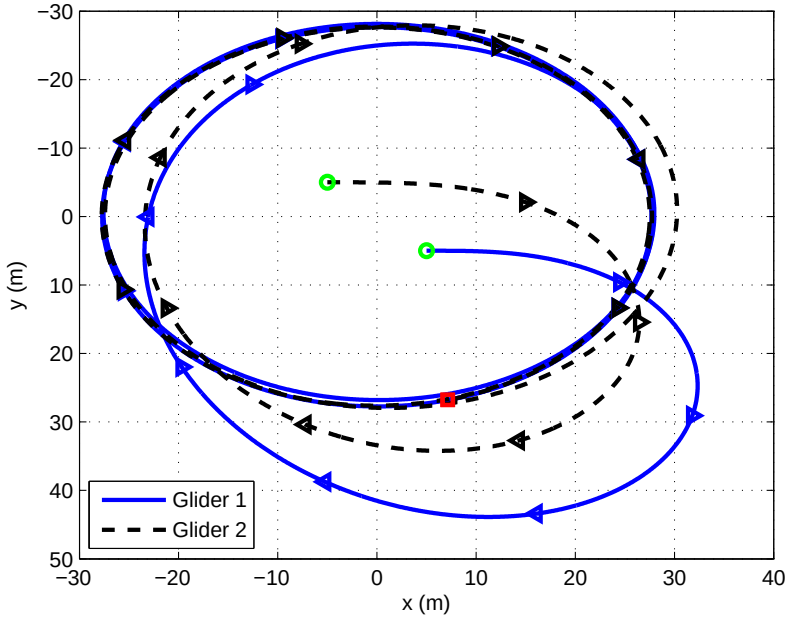

Figure 6.11 Synchronization of two *Slocum* gliders for control volume sampling.

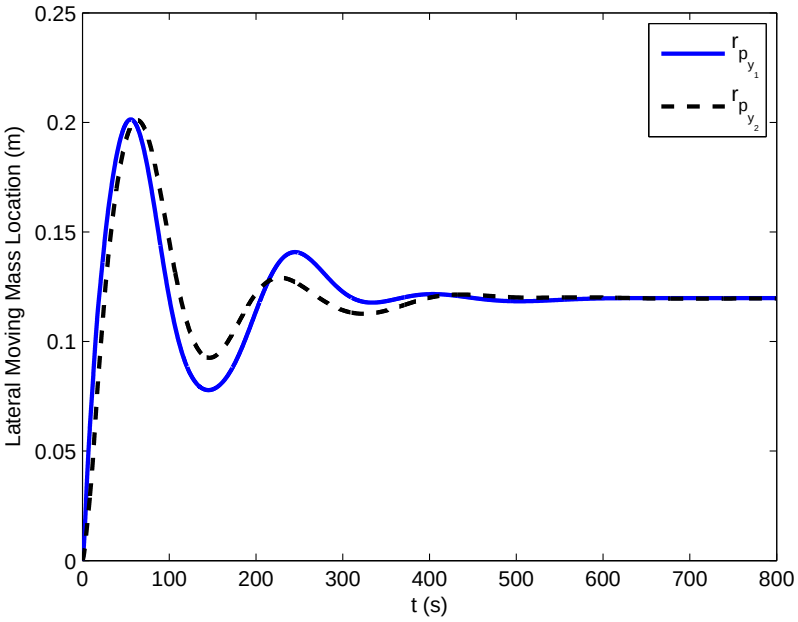

Figure 6.12 Position of lateral moving mass.

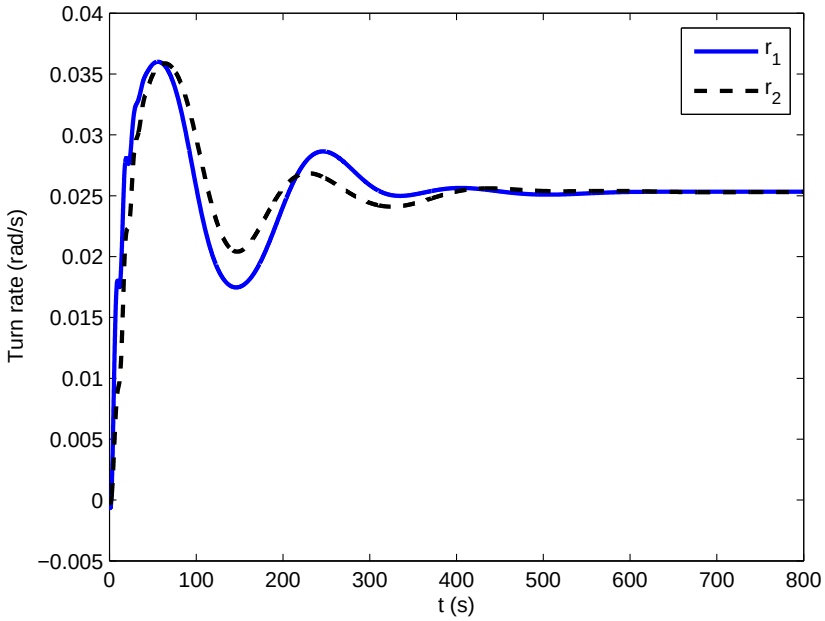

Figure 6.13 *Slocum* gliders' turn rate.

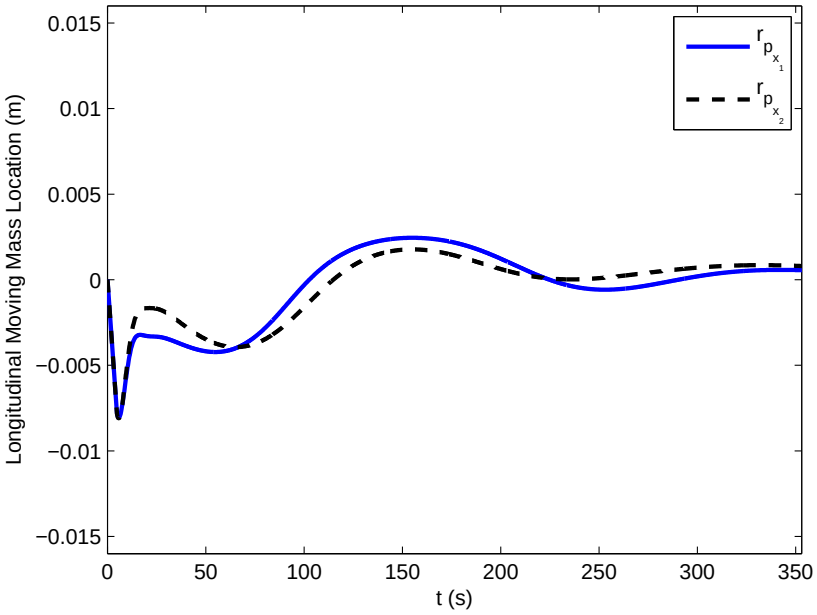

Figure 6.14 Position of longitudinal moving mass.

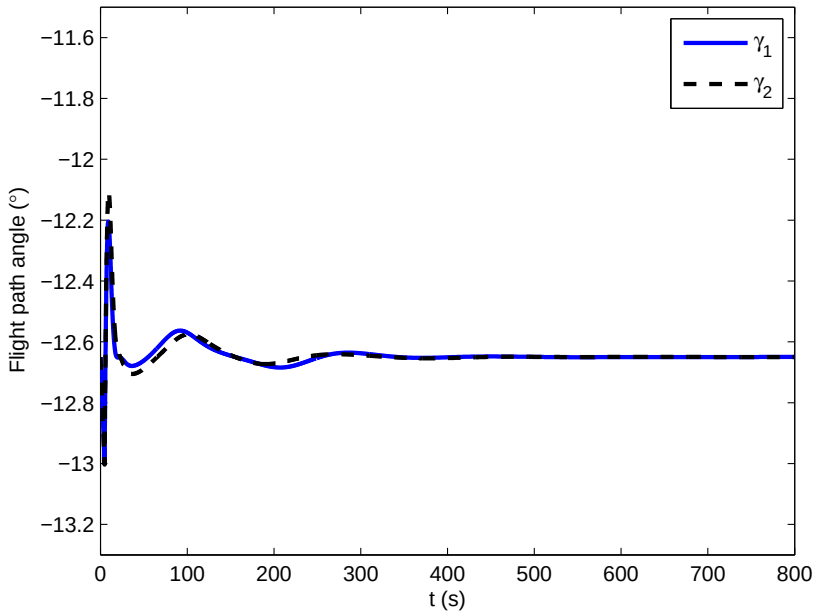

Figure 6.15 *Slocum* gliders' glide path angle.

Chapter 7

Conclusions and Future Work

An approximate solution for steady turning motions of underwater gliders has been derived using a sophisticated dynamic model. The problem was formulated as a regular perturbation problem using wings-level, equilibrium flight as the nominal state and turn rate as the small perturbation parameter. As an illustration, the result was applied to an existing model of the *Slocum* underwater glider. The analytical result, though approximate, is valuable because it gives better insight into the effect of parameters on vehicle motion and stability. This insight can, in turn, lead to better usage guidelines for current vehicles and design guidelines (e.g., actuator sizing) for future vehicles.

Building on results in glider steady motion analysis, a feedforward/feedback motion control system was presented to control speed, glide path angle, and turn rate. The control system uses feedforward commands obtained from an approximate solution for steady turning motion and includes feedback to compensate for approximation error and other uncertainties. The control system design includes model reference controllers for the servo-actuators, to allow actuator rate and magnitude saturation effects to be more easily analyzed and accommodated. Stability of the closed-loop system was analyzed using slowly varying systems theory in which the turn rate command was treated as a slowly varying parameter. A bound on turn acceleration was obtained as a product of the analysis. The controller's effectiveness

was demonstrated in a simulation of a multi-body model of the underwater glider *Slocum*.

The proposed control system provides a mechanism for path following. The next step was to implement a guidance strategy, together with a path planning strategy, and one which continues to exploit the natural efficiency of this class of vehicle. The structure of the approximate solution for steady turning motion is such that, to first order in turn rate, the glider's horizontal component of motion matches that of "Dubins' car," a kinematic car with bounded turn rates. Dubins' car is a classic example in the study of time-optimal control for mobile robots. For an underwater glider, one can relate time optimality to energy optimality. Specifically, for an underwater glider travelling at a constant speed and maximum flight efficiency (i.e., maximum lift-to-drag ratio), minimum time paths are minimum energy paths. Hence, energy-efficient paths can be obtained by generating sequences of steady wings-level and turning motions. These efficient paths can, in turn, be followed using the motion control system described here. A variety of guidance and path planning algorithms can be directly applied. The motion control system is applied to tracking of a Dubins path and coordination on a helical path.

An obvious next step is physical implementation of the proposed feedforward/feedback motion controller on an underwater glider. Virginia Tech and University of Washington are currently collaborating to implement the developed controller on *Seaglider*. Ongoing analysis focuses on tracking suboptimal Dubins paths which accommodate turn rate and turn acceleration limits in the presence of uniform currents.

Bibliography

[1] Geisbert, J. S., *Hydrodynamic Modeling for Autonomous Underwater Vehicles Using Computational and Semi-Empirical Methods*, Master's thesis, Virginia Polytechnic Institute & State University, Blacksburg, VA, June 2007.

[2] Stengel, R. F., *Flight Dynamics*, Princeton University Press, Princeton, NJ, 2004.

[3] Anisi, D. A., "Optimal motion control of a ground vehicle," Tech. Rep. FOI-R–0961–SE, Swedish Defence Research Agency, Stockholm, Sweden, July 2003.

[4] "AUV Technologies," *Autonomous Undersea Vehicle Applications Center Website*, August 2009, Available at `http://auvac.org/resources/`.

[5] Woithe, H. C., Tilkijieva, D., and Kremer, U., "Toward a Resuorce-Aware Programming Architecture for Smart Autonomous Underwater Vehicles," Technical Report DCS-TR-637, Rutgers University, June 2008.

[6] Leonard, N. E., Paley, D. A., Lekien, F., Sepulchre, R., Fratantoni, D. M., and Davis, R. E., "Collective Motion, Sensor Networks, and Ocean Sampling," *Proceedings of the IEEE*, Vol. 95, No. 1, January 2007, pp. 48–74.

[7] Tropea, C., Yarin, A. L., and Foss, J. F., editors, *Springer Handbook of Experimental Fluid Mechanics*, Springer, 2007.

[8] Stommel, H., "The Slocum mission," *Oceanography*, Vol. 2, 1989, pp. 22–25.

[9] Graver, J. G., *Underwater Gliders: Dynamics, Control, and Design*, Ph.D. thesis, Princeton University, 2005.

[10] Webb, D. C., Simonetti, P. J., and Jones, C. P., "SLOCUM: An Underwater Glider Propelled by Environmental Energy," *Journal of Oceanic Engineering*, Vol. 26, No. 4, 2001, pp. 447–452, Special Issue on Autonomous Ocean-Sampling Networks.

[11] Eriksen, C. C., Osse, T. J., Light, R. D., Wen, T., Lehman, T. W., Sabin, P. L., Ballard, J. W., and Chiodi, A. M., "Seaglider: A Long-Range Autonomous Underwater Vehicle for Oceanographic Research," *Journal of Oceanic Engineering*, Vol. 26, No. 4, 2001, pp. 424–436, Special Issue on Autonomous Ocean-Sampling Networks.

[12] Sherman, J., Davis, R. E., Owens, W. B., and Valdes, J., "The Autonomous Underwater Glider "Spray"," *Journal of Oceanic Engineering*, Vol. 26, No. 4, 2001, pp. 437–446, Special Issue on Autonomous Ocean-Sampling Networks.

[13] Davis, R. E., Eriksen, C. C., and Jones, C. P., "Autonomous Buoyancy-Driven Underwater Gliders," *Technology and Applications of Autonomous Underwater Vehicles*, edited by G. Griffiths, Vol. 2, chap. 3, Taylor and Francis, 2002.

[14] Jenkins, S. A., Humphreys, D. E., Sherman, J., Osse, J., Jones, C., Leonard, N., Graver, J., Bachmayer, R., Clem, T., Carroll, P., Davis, P., Berry, J., Worley, P., and Wasyl, J., "Underwater Glider System Study," Tech. Rep. 53, Scripps Institution of Oceanography, May 2003.

[15] Jones, C., Webb, D., Glenn, S., Schofield, O., Kerfoot, J., Kohut, J., Roarty, H., Aragon, D., Haldeman, C., Haskin, T., and Kahl, A., "Slocum Glider Extending the Endurance," The 16th International Symposium on Unmanned Untethered Submersible Technology (UUST09), Durham, NH, August 23-26 2009.

[16] Mientka, M., "Gliders Flying onto the World's Scientific Stage More Improvements Planned," *Unmanned Systems*, Vol. 27, No. 1, January 2009, pp. 22 – 23.

[17] Hines, S., "Seaglider monitors waters from Arctic during record-breaking journey under ice," *EurekAlert*, April 28 2009, Available at `http://www.eurekalert.org/pub-releases/2009-04/uow-smw042809.php`.

[18] "iRobot Seaglider," *iRobot Corporation Website*, September 2009, Available at `http://www.irobot.com/sp.cfm?pageid=393`.

[19] Tomoda, Y., Kawaguchi, K., Ura, T., and Kobayashi, H., "Development and Sea Trials of a Shuttle Type AUV "ALBAC"," *In Proc. 8th Int. Symposium on Unmanned Untethered Submersible Tech.*, 1993.

[20] Guo, C. and Kato, N., "Mini Underwater Glider (MUG) for Education," *Workshop for Asian and Pacific Universities' Underwater Roboticians (APuuRobo 2008)*, Institute of Industrial Science, The University of Tokyo, Japan, January 2008.

[21] Graver, J. G., Liu, J., Woolsey, C. A., and Leonard, N. E., "Design and Analysis of an Underwater Glider for Controlled Gliding," *Conference on Information Sciences and Systems*, 1998, pp. 801–806.

[22] Scott, R. D., *Cooperative Tracking for Persistent Littoral Undersea Surveillance*, Master's thesis, Massachusetts Institute of Technology, June 2007.

[23] Rusling, M., "Gliders Will Aid Naval Research," *National Defense Industrial Association Business and Technology Magazine*, June 2009, Available at `http://www.nationaldefensemagazine.org/archive/2009/June/Pages/`.

[24] GmbH, E., "Lessons learned from fish fins," 2008, Available at `http://www.evologics.de/en/products/`.

[25] Godin, M. and Fulton-Bennett, K., "Monterey Bay 2006 field experiments," *Montray Bay Aquarium Research Institute*, August 2006, Available at `http://www.mbari.org/MB2006/UPS/mb2006-ups-links.htm`.

[26] Bhatta, P., *Nonlinear Stability and Control of Gliding Vehicles*, Ph.D. thesis, Princeton University, 2006.

[27] Leonard, N. E. and Graver, J. G., "Model-Based Feedback Control of Autonomous Underwater Gliders," *Journal of Oceanic Engineering*, Vol. 26, No. 4, 2001, pp. 633–645, Special Issue on Autonomous Ocean-Sampling Networks.

[28] Galea, A. M., *Optimal path planning and high level control of an autonomous gliding underwater vehicle*, Master's thesis, Massachusetts Institute of Technology, 1999.

[29] Bachmayer, R., Graver, J., and Leonard, N. E., "Glider Control: A Close Look into the Current Glider Controller Structure and Future Developments," *IEEE Oceans 2003*, Vol. 2, 2003, pp. 951–954.

[30] Woolsey, C. A., "Reduced Hamiltonian Dynamics for a Rigid Body/Mass Particle System," *Journal of Guidance, Control, and Dynamics*, Vol. 28, No. 1, January-February 2005, pp. 131–138.

[31] Mahmoudian, N., Geisbert, J., and Woolsey, C. A., "Dynamics & Control of Underwater Gliders I: Steady Motions," Tech. Rep. VaCAS-2007-01, Virginia Center for Autonomous Systems, Virginia Tech, Blacksburg, VA, June 2007, Available at `http://www.unmanned.vt.edu/discovery/reports.html`.

[32] Mahmoudian, N., Woolsey, C., and Geisbert, J., "Steady Turns and Optimal Path for Underwater Gliders," AIAA Guidance, Navigation and Control Conference and Exhibit, Hilton Head, SC, Aug 20-23 2007.

[33] Mahmoudian, N. and Woolsey, C. A., "Underwater glider motion control," *IEEE Conference on Decision and Control*, Cancun, Mexico, December 2008, pp. 552 – 557.

[34] Fossen, T. I., *Guidance and Control of Ocean Vehicles*, John Wiley and Sons, 1995.

[35] Stevens, B. L. and Lewis, F. L., *Aircraft control and simulation, Second Ed.*, John Wiley and Sons, INC., Hoboken, N.J., 2003.

[36] Etkin, B. and Reid, L., *Dynamics of Flight Stability and Control*, John Wiley and Sons,Inc., New York, 1996.

[37] Guckenheimer, J. and Holmes, P., *Nonlinear Oscillations, Dynamical Systems, and Bifurcations of Vector Fields*, Springer-Verlag, New York, NY, 1983.

[38] Hartman, P., *Ordinary Differential Equations*, John Wiley and Sons, Inc., New York, NY, 1964.

[39] Mahmoudian, N. and Woolsey, C., "Analysis of Feedforward/Feedback Control Design for Underwater Gliders Based on Slowly Varying Systems Theory," AIAA Guidance, Navigation and Control Conference and Exhibit, Chicago, IL, Aug 20-23 2009.

[40] Khalil, H. K., *Nonlinear Systems*, Prentice Hall, Upper Saddle River, NJ, 3rd ed., 2002.

[41] Rugh, W. J., *Linear System Theory*, Prentice Hall, Upper Saddle River, NJ, 2nd ed., 1996.

[42] Kostov, V. and Degtiariova-Kostova, E., "Suboptimal paths in the problem of a planar motion with bounded derivative of the curvature," Tech. Rep. 2051, Institut National de Recherche en Informatique et en Automatique (INRIA), July 1993.

[43] Scheuer, A. and Laugier, C., "Planning sub-optimal and continuous-curvature paths for car-like robots," *IEEE/RSJ International Conference on Intelligent Robots and Systems*, Victoria, B.C., Canada, October 1998, pp. 25–31.

[44] Mahmoudian, N. and Woolsey, C., "Feedforward/Feedback Tracking of a First Order Approximate Equilibrium Manifold," American Mathematical Society 2009 Spring Southeastern Meeting, Raleigh, NC, April 4-5 2009.

[45] Dubins, L. E., "On curves of minimal length with a constraint on average curvature and with prescribed initial and terminal positions and tangents," *American Journal of Mathematics*, Vol. 79, 1957.

[46] Techy, L., Woolsey, C. A., and D. G. Schmale, I., "Path planning for efficient UAV coordination in aerobiological sampling missions," *IEEE Conference on Decision and Control*, Cancun, Mexico, December 2008, pp. 2814–2819.

[47] Mahmoudian, N. and Woolsey, C., "Efficient Guidance and Control for Underwater Gliders," The 16th International Symposium on Unmanned Untethered Submersible Technology (UUST09), Durham, NH, August 23-26 2009.

[48] Reeds, J. A. and Shepp, L. A., "Optimal paths for a car that goes both forwards and backwards," *Pacific Journal of Mathematics*, Vol. 145, No. 2, 1990, pp. 367–393.

[49] Sussmann, H. J. and Tang, G., "Shortest paths for the Reeds-Shepp car: A worked out example of the use of geometric techniques in nonlinear optimal control," Tech. Rep. 91-10, Rutgers University Center for Systems and Control, New Brunswick, NJ, 1991.

[50] Boissonnat, J.-D., Cérézo, A., and Leblond, J., "Shortest paths of bounded curvature in the plane," *IEEE International Conference on Robotics and Automation*, Nice, France, May 1992, pp. 2315–2320.

[51] Souéres, P., Fourquet, J.-Y., and Laumond, J.-P., "Set of reachable positions for a car," *IEEE Transactions on Automatic Control*, Vol. 39, No. 8, August 1994, pp. 1626–1630.

[52] Bui, J.-D. B. X.-N., "Accessibility region for a car that only moves forwards along optimal paths," Tech. Rep. 2181, Institut National de Recherche en Informatique et en Automatique (INRIA), January 1994.

[53] Bui, X.-N., Boissonnat, J.-D., Souéres, P., and Laumond, J.-P., "Shortest path synthesis for Dubins Non-holomic robot," *IEEE International Conference on Robotics and Automation*, San Diego, CA, May 1994.

[54] Scheuer, A., *Planification de chemin à courbure continue pour robot mobile non-holonome*, Ph.D. thesis, Institut National Polytechnique de Grenoble, 1998.

[55] Boissonnat, J.-D., Cérézo, A., and Leblond, J., "A note on shortest paths in the plane subject to a constraint on the derivative of the curvature," Tech. Rep. 2160, Institut National de Recherche en Informatique et en Automatique (INRIA), January 1994.

[56] Kostov, V. and Degtiariova-Kostova, E., "The planar motion with bounded derivative of the curvature and its suboptimal paths," Tech. Rep. 2189, Institut National de Recherche en Informatique et en Automatique (INRIA), January 1994.

[57] McGee, T. G. and Hedrick, J. K., "Optimal path planning with a kinematic airplane model," *Journal of Guidance, Control, and Dynamics*, Vol. 30, No. 2, 2007, pp. 629–633.

[58] Rysdyk, R., "Unmanned Aerial Vehicle Path Following for Target Observation in Wind," *Journal of Guidance, Control, and dynamics*, Vol. 29, No. 5, 2006, pp. 1092–1100.

[59] Sepulchre, R., Paley, D. A., and Leonard, N. E., "Stabilization of Planar Collective Motion: All-to-All Communication," *IEEE Transactions on Automatic Control*, Vol. 52, No. 5, 2007, pp. 811–824.

[60] Encarnacao, P. and Pascoal, A., "3D Path Following for Autonomous Underwater Vehicle," 39th IEEE Conference on Decision and Control, Sydney, Australia, December 2000.

[61] Veirs, S. R., *Heat flux and hydrography at a submarine volcano: Observations and models of the Main Endeavour vent field in the northeast Pacific*, Ph.D. thesis, University of Washington, 2003.